

Wright State University

CORE Scholar

---

[Browse all Theses and Dissertations](#)

[Theses and Dissertations](#)

---

2018

## Multiscale Modeling of Hemodynamics in Human Vessel Network and Its Applications in Cerebral Aneurysms

Hongtao Yu  
*Wright State University*

Follow this and additional works at: [https://corescholar.libraries.wright.edu/etd\\_all](https://corescholar.libraries.wright.edu/etd_all)



Part of the [Engineering Commons](#)

---

### Repository Citation

Yu, Hongtao, "Multiscale Modeling of Hemodynamics in Human Vessel Network and Its Applications in Cerebral Aneurysms" (2018). *Browse all Theses and Dissertations*. 1937.  
[https://corescholar.libraries.wright.edu/etd\\_all/1937](https://corescholar.libraries.wright.edu/etd_all/1937)

This Dissertation is brought to you for free and open access by the Theses and Dissertations at CORE Scholar. It has been accepted for inclusion in Browse all Theses and Dissertations by an authorized administrator of CORE Scholar. For more information, please contact [library-corescholar@wright.edu](mailto:library-corescholar@wright.edu).

# **MULTISCALE MODELING OF HEMODYNAMICS IN HUMAN VESSEL NETWORK AND ITS APPLICATIONS IN CEREBRAL ANEURYSMS**

A dissertation submitted in partial fulfillment  
of the requirements for the degree of  
Doctor of Philosophy

by

HONGTAO YU  
B.E., Dalian Jiao Tong University, 2011  
M.S.E.G., Wright State University, 2014

2018  
Wright State University

WRIGHT STATE UNIVERSITY

GRADUATE SCHOOL

April 16, 2018

I HEREBY RECOMMEND THAT THE DISSERTATION PREPARED UNDER MY SUPERVISION BY Hongtao Yu ENTITLED Multiscale Modeling of Hemodynamics in Human Vessel Network and Its Applications in Cerebral Aneurysms BE ACCEPTED IN PARTIAL FULFILLMENT OF THE REQUIREMENTS FOR THE DEGREE OF Doctor of Philosophy.

---

George P.G. Huang, Ph.D.  
Dissertation Director

---

Zifeng Yang, Ph.D.  
Dissertation Co-Director

---

Bryan R. Ludwig, M.D.  
Dissertation Co-Director

---

Frank W. Ciarallo, Ph.D.  
Director, Ph.D. in Engineering Program

---

Barry Milligan, Ph.D.  
Interim Dean, Graduate School

Committee on  
Final Examination

---

George P.G. Huang, Ph.D.

---

Zifeng Yang, Ph.D.

---

Bryan R. Ludwig, M.D.

---

Joseph J.S. Shang, Ph.D.

---

Philippe Sucosky, Ph.D.

## ABSTRACT

Yu, Hongtao Ph.D., Engineering Ph.D. Program, Department of Mechanical and Materials Engineering, Wright State University, 2018. *Multiscale Modeling of Hemodynamics in Human Vessel Network and Its Applications in Cerebral Aneurysms*.

Three-dimensional (3D) simulation of patient-specific morphological models has been widely used to provide the hemodynamic information of individual patients, such as wall shear stress (WSS), oscillatory shear index (OSI), and flow patterns, etc. Since patient-specific morphological segment was only restricted locally, boundary conditions (BCs) are required to implement the CFD simulation. Direct measurements of the flow and pressure waveforms were often required as input BCs for 3D CFD simulations of patient-specific models. However, as the morphology develops, the feedback from this topological deformation may lead to BCs being altered, and hence without this feedback, the flow characteristics of the morphology are only computed locally.

A one-dimensional (1D) numerical model containing the entire human vessel network has been proposed to compute the global hemodynamics. In the meantime, experimental studies of blood flow in the patient-specific modeling of the circle of Willies (CoW) was conducted. The flow and pressure waveforms were quantified to validate the accuracy of the pure 1D model. This 1D model will be coupled with a 3D morphological model to account for the effects of the altered BCs. The proposed 1D-3D multi-scale modeling approach investigates how the global hemodynamic changes can be induced by the local morphological effects, and in consequence, may further result in altering of BCs to

interfere with the solution of the 3D simulation. Validation of the proposed multi-scale model has also been made by comparing the solution of the flow rate and pressure waveforms with the experimental data and 3D numerical simulations reported in the literature. Moreover, the multi-scale model is extended to study a patient-specific cerebral aneurysm and a stenosis model. The proposed multi-scale model can be used as an alternative to current approaches to study intracranial vascular diseases such as an aneurysm, stenosis, and combined cases.

Keywords: 1D model, 3D CFD simulation, multi-scale model, boundary conditions, vascular aging, hemodynamics, cerebral aneurysm

## TABLE OF CONTENTS

	Page
1 INTRODUCTION .....	1
1.1 Background .....	1
1.1.1 Cardiovascular system .....	1
1.1.2 Cerebral aneurysm .....	3
1.2 Motivations and objectives.....	6
2 LITERATURE REVIEW .....	8
2.1 1D numerical calculation of blood flow.....	8
2.2 3D CFD simulations of cerebral aneurysms .....	13
2.3 0D-1D-3D multi-scale simulation.....	17
3 METHODOLOGY .....	21
3.1 0D-1D model.....	21
3.1.1 Governing equations .....	22
3.1.2 Discretization .....	23
3.1.3 Junctions in human vessel networks .....	25
3.1.4 0D models .....	27
3.2 <i>In vitro</i> experiments on the CoW .....	30
3.2.1 Experimental setup.....	30
3.3 Simulation of the vascular aging.....	36
3.4 3D simulation of cerebral aneurysms .....	38
3.4.1 The reconstruction of aneurysm models .....	38
3.5 Hemodynamic parameters.....	39
3.6 1D-3D multi-scale modeling.....	40
4 THE VARIATIONS OF THE COW .....	43
4.1 Overview .....	43
4.2 Validation of the 1D model.....	45
4.3 Flow characteristics of a complete CoW.....	51

4.4	Flow characteristics in variational circle of Willis.....	52
4.5	Simulation results vs. experimental results .....	56
4.6	Discussion .....	62
4.6.1	The variations of the CoW .....	62
4.6.2	The experimental study .....	64
4.7	Summary .....	65
5	THE INFLUENCE OF THE VASCULAR AGING .....	67
5.1	Overview .....	67
5.2	Cardiovascular system.....	69
5.3	Validation .....	74
5.4	Configurations of CoW .....	76
5.5	Discussion .....	79
5.6	Summary .....	83
6	3D SIMULATIONS OF ANEURYSMS.....	84
6.1	Overview .....	84
6.2	Aneurysm topology .....	84
6.3	Computational fluid dynamics .....	86
6.3.1	Analysis conditions .....	86
6.3.2	Mesh independent study .....	88
6.4	Time-averaged flow patterns.....	90
6.5	Pressure and WSS distributions .....	94
6.6	Discussion .....	97
6.7	Summary .....	99
7	MULTI-SCALE SIMULATIONS FOR CEREBRAL BLOOD FLOW WITH ANEURYSMS AND/OR STENOSES .....	101
7.1	Overview .....	101
7.2	Validation studies of the multi-scale model .....	102
7.3	Application of the multi-scale model for patient-specific segments.....	106
7.3.1	Setup of the patient-specific models .....	106

7.3.2	Computational results .....	108
7.4	Discussion .....	114
7.5	Summary .....	116
8	CONCLUSIONS.....	116
8.1	Summary of the dissertation.....	116
8.2	Future applications of the model.....	119
9	REFERENCES .....	121



## LIST OF FIGURES

Figure	Page
Figure 1.1 The cardiovascular system and the anatomy of the heart. ( <i>Anatomy of the Heart</i> , 2016).....	1
Figure 1.2 Various cerebral aneurysms located on the CoW.....	4
Figure 1.3 Variations structure of the CoW. The middle one represents the complete CoW. A-H represent the variations in the anterior and posterior parts. ....	5
Figure 3.1 Arterial and venous network consists of eighty-five arteries and 158 veins; (a) represents the arterial circulation system; (b) represents the venous circulation system .....	22
Figure 3.2 1D model vessel tree connection. (a) is branching point and (b) is the merging point. ....	26
Figure 3.3 (a), a simple artery-to-vein lumped model. Left side is the feeding artery, and the right side is the collecting vein. (b), a complex lumped model. Parameters for resistances, inductors, and capacitors are given in (Huang et al., 2015 and Müller et al., 2014) .....	28
Figure 3.4 Reconstructed CoW model from 3D angiography. ....	31
Figure 3.5 Schematic drawing of the experimental setup.....	34
Figure 3.6 Calibration curves for the Transonic TS410 flow meter (top) and the Millar Instruments SPR-524 pressure transducer .....	35
Figure 3.7 The main screen of the LabVIEW (Top) and the program to convert the voltage reading to pascal.....	36
Figure 3.8 a. Initial 3-D model; b. Vessel geometry after deformable modeling and removing arterial branches.....	39
Figure 3.9, the multi-scale method flowchart of a test case containing three arteries and coupling with a 3D artery model. ....	42
Figure 4.1 Comparison of waveforms from thirty-seven-artery-network model by Alastruey et al., (2011) with the waveforms of THINKS model. The top is the pressure	

and flow rate waveforms in the aortic arch II; the middle is the pressure and flow rate waveforms in the left subclavian I; the bottom is the pressure and flow rate waveforms in the thoracic aorta II. ....	47
Figure 4.2 Comparison of Fifty-six-network model with 1D model. The top is the pressure and flow rate waveforms in the abdominal aorta V; the middle is the pressure and flow rate waveforms in the aortic arch I; the bottom is the pressure and flow rate waveforms in the thoracic aorta III. ....	48
Figure 4.3 Simulated waveforms compared with the raw and normalized in vivo experimental data by Gwilliam et al., (2009): in common carotid artery proximal to bifurcation and internal carotid artery distal to the bifurcation. “+” represents the experimental data with error bar representing the confidence interval of the flow rate (vertical bar) and temporal response (horizontal bar). Black and red lines represent simulation data. ....	49
Figure 4.4 Absolute and dimensionless waveform comparison with in vivo experimental data: in internal carotid artery proximal to siphon, in internal carotid artery proximal to CoW, and in the midsection of the basilar artery (Tanaka et al., 2006). ....	51
Figure 4.5 Flow rate distribution of a subject with a complete CoW. (a) Flow rate in ml min <sup>-1</sup> . The flow directions are given by the arrow signs; (b) Percentage of total flow rate, percentage number in black is for afferent vessels, blue is for afferent vessels with experimental data (Tanaka et al., 2006), and red is for efferent vessels. ....	52
Figure 4.6 Flow rate distribution in CoW caused by the anomalies. The flow rates are in terms of their percentages to the total flow rates. Number in black is for afferent vessels from calculation, blue is for afferent vessels from experimental data (Tanaka et al., 2006), and red is for efferent vessels; (a) missing A1 artery, (b) missing P1 artery, (c) missing one PcoA, (d) missing AcoA, (e) missing both PcoAs, (f) missing P1-PcoA. ....	54
Figure 4.7 Comparison of the mean cross-sectional velocities at the midsection of AcoA for the complete, missing L-A1 and missing R-A1 types. The positive sign is defined from right to left. ....	55

Figure 4.8 The pressure and flow rates Comparisons of the experimental with the numerical results at the main artery, common carotid artery, and subclavian artery. Black dash lines represent the standard deviation of the experimental measurement. Red lines represent the numerical results on the right side of the artery. ....	57
Figure 4.9 The pressure and flow rates Comparisons of the experimental with the numerical results at R/L internal carotid arteries I vertebral arteries I. ....	58
Figure 4.10 The pressure and flow rates Comparisons of the experimental with the numerical results at R/L anterior cerebral arteries, middle cerebral arteries, and posterior cerebral arteries. Black dash lines represent the standard deviation of the experimental measurement. Red dash lines represent the numerical results on the right side of the artery .....	60
Figure 4.11 The pressure and flow rates Comparisons of the experimental with the numerical results at R/L anterior cerebral arteries, middle cerebral arteries, and posterior cerebral arteries. ....	61
Figure 4.12 The pressure and flow rates Comparisons of the experimental with the numerical results at R/L posterior communicating arteries and anterior communicating artery. ....	62
Figure 5.1 Simulated hemodynamics for the heart for both the NVA and EVA male 25 years, which consists of four cardiac chambers. RA, right atrium; RV, right ventricle; LA, left atrium; LV, left ventricle. (a) and (b) show the blood pressure in the heart chambers, pulmonary artery, and ascending aorta; (c) and (d) show the volume in the heart chambers. ....	70
Figure 5.2 Comparisons between the simulated data and the measured data of central systolic pressure for both the NVA and EVA.....	72
Figure 5.3 Comparison between the simulated and the measured data for both the NVA and the EVA; (a) the central pulse pressure, and (b) the central augmentation index.....	73
Figure 5.4 Mean blood flow in the selected veins: computational results versus literature data. ....	74

Figure 5.5 Arterial pressure propagation along the arterial tree during one cardiac cycle. ....	74
Figure 5.6 Comparison of the total flow rate entering the CoW between the simulated NVA, EVA, and the measured data. ....	75
Figure 5.7 Comparison of the flow rate waveform between the simulated NVA, EVA, and measured waveform in four arterial sites as the large black dot indicates in the arterial tree. A is the flow rate in the middle cerebral artery; B is the flow rate in the vertebral artery; C is the flow rate in the internal carotid artery; D is the flow rate in the common carotid artery. ....	76
Figure 5.8 Comparisons of the pressure and flow rate waveform in a complete CoW. Top two waveforms represent the pressure and flow rate in the anterior communication artery; bottom two waveforms represent the pressure and flow rate in the posterior communicating artery. ....	78
Figure 5.9 Comparisons of the pressure and flow rate waveform in an incomplete CoW. Top two waveforms represent the pressure and flow rate in the anterior communication artery with missing RA1; bottom two waveforms represent the pressure and flow rate in the posterior communicating artery with missing RP1. ....	78
Figure 6.1 Anatomic model (a) and two morphology models: (b) evenly enlarged model; (c) bi-lobed model. ....	85
Figure 6.2 Inlet boundary condition for the simulation, a. anatomic modeling; b. comparison of the pressure waveform for ICA terminus and PcoA; c. volume flow rate for ICA inlet; d. blood pressure waveform. ....	87
Figure 6.3 Monitor point position and the pressure and velocity profile from the second period to the fifth period. ....	88
Figure 6.4 Computational meshes. (a) is coarse mesh; (b) is middle mesh; (c) is fine mesh. ....	88
Figure 6.5 Time-averaged pressure (top) and WSS (bottom) distributions over the aneurysm surface: (a) and (d): the coarse mesh; (b) and (e): the middle mesh; and WSS distribution: (c) and (f): the fine mesh. ....	89

Figure 6.6 Time-averaged shear rate distributions over the aneurysm surface. ....	90
Figure 6.7 Time-averaged streamlines: (a), the anatomic case; (b), the enlarged case; (c), the bi-lobed case. ....	91
Figure 6.8 Time-averaged out-of-plane velocity contour with 2-D vectors on the surface of the inlet of the aneurysm: (a), the surface of the inlet of the aneurysm; (b), the anatomic case; (c), the enlarged case; (d), the bi-lobed case. Note that the range of the length of the velocity vector is from 0 to 0.38.....	92
Figure 6.9 Time-averaged out-of-plane velocity contour with in-plane velocity vectors on several cross-sections in the aneurysm with streamlines for the anatomic case.....	93
Figure 6.10 Time-averaged out-of-plane velocity contour with in-plane velocity vectors on several cross sections in the aneurysm with streamlines for the evenly enlarged case. ....	93
Figure 6.11 Time-averaged out-of-plane velocity contour with in-plane velocity vectors on several cross sections in the aneurysm with streamlines for the bi-lobed case. ....	94
Figure 6.12 Time-averaged pressure distributions: (a), the perspective view of the aneurysm; (b), the anatomic case; (c), the enlarged case; (d), the bi-lobed case.....	96
Figure 6.13 Time-averaged WSS distributions: (a), the anatomic case; (b), the enlarged case; (c), the bi-lobed case. ....	96
Figure 6.14 The RMS of Pressure distributions: (a). The anatomic case; (b). The enlarged case; (c). The bi-lobed case.....	97
Figure 6.15 The variance of WSS distributions: (a). The anatomic case; (b). The enlarged case; (c). The bi-lobed case.....	97
Figure 7.1 The geometries of the three test cases. The case I is stenotic artery; Case II and II are bifurcation models with different area ratios. ....	103
Figure 7.2 the mean pressure drop comparison of the multi-scale model with the 3D model and previous CFD simulation and experimental data by Banerjee et al., (2008). ....	104
Figure 7.3 Pressure and flow rate waveform comparisons among the 1D, multiscale, and 3D models. Location A & B, the pressure difference between locations A and B; Location B and C, the flow rate waveforms comparison.....	105

Figure 7.4 Pressure and flow rate waveform comparisons among the 1D, multiscale, and 3D models. Location A & B, the pressure difference between locations A and B; Location B and C, the flow rate waveforms comparison.....	106
Figure 7.5 The description of applications of the multi-scale model, where a 3D aneurysm segment and a CCA bifurcation model are coupled with a 1D model of the entire cardiovascular system. LICA: left internal carotid artery; LPcoA: left posterior communicating artery; LICA_T: left internal carotid artery terminal; LCCA: left common carotid artery; LECA: left external carotid artery.....	107
Figure 7.6 The pressure and flow rate waveforms comparisons of the multi-scale model with the baseline model at the ICA upstream and ICA_T and PcoA downstream as red dots represent. ....	110
Figure 7.7 Pressure, WSS, OSI distributions over the surface and the velocity path-lines for the LICA aneurysm model. ....	111
Figure 7.8 The pressure and flow rate waveforms comparisons of the multi-scale model with the baseline model at the LCCA upstream and LICA and LECA downstream as red dots represent. ....	112
Figure 7.9 WSS, OSI distributions over the surface and the velocity path-lines for the LCCA bifurcation model. ....	113

## LIST OF TABLES

Table	Page
Table 3.1 Parameters of the Tygon and silicone tubes presented in Figure 3.5. ....	32
Table 3.1 continued from previous page.....	33
Table 3.2 Peripheral resistance. ....	36
Table 3.3 Parameter changes in the aortic pulse wave velocity (Co), ascending aorta radius (R) and left ventricle peak systolic elastance during aging.....	38
Table 4.1 The CoW anomalies and their impacts on the total flow rate and the blood supply to different regions of the brain. The case is referred to Figure 22.....	54
Table 4.2 Flow rate distribution in CoW for a subject with missing right A1. Flow rate in ml min <sup>-1</sup> . This Table is referred to the case of missing R-A1 in Figure 21 (a). The flow directions are shown as arrows. ....	54
Table 4.3. Comparisons of the mean flow rate and pressure at various locations.....	59
Table 5.1 Comparison between measurements and simulations. ....	71
Table 5.2 The rate of pressure rise from diastolic to systolic in AcoA and PcoA with complete and incomplete CoW, corresponding to left RA1 and RP1, for the NVA and EVA subjects with 25 and 85 years. ....	82
Table 5.3 The systolic flow rate in AcoA and PcoA with complete and incomplete CoW, corresponding to missing RA1 and RP1, for the NVA and EVA subjects at 25 and 85 years old. ....	83
Table 6.1 The comparison of simulation times, pressure difference, and WSS difference among different meshes. ....	89
Table 7.1: Comparison of mean flow rates in the CoW between the multi-scale model and the baseline model for the LCCA bifurcation model. The labels of vessels refer to the position on the CoW network on the right.....	113

Table 7.2: Comparison of mean flow rates in the CoW between the multi-scale model and the baseline model for the LCCA bifurcation model. The labels of vessels refer to the position on the CoW network on the right.....	113
---	-----



## ABBREVIATIONS

0D	Zero-Dimensional
1D	One-Dimensional
3D	Three-Dimensional
AcoA	Anterior Communicating Artery
Aix	Augmentation Index
BCs	Boundary Conditions
CCA	Common Carotid Artery
CCD	Charge-Coupled Device
CFD	Computational Fluid Dynamics
CFL	Courant-Friedrichs-Lewy
CoW	Circle of Willis
CT	Computed Tomography
DCG	Discontinuous Galerkin
DSA	Digital Subtraction Angiographic
EVA	Early Vascular Aging
IVC	Inferior Vena Cava
MRA	Magnetic Resonance Angiogram
MRI	Magnetic Resonance Imaging
NVA	Normal Vascular Aging
ODE	Ordinary Differential Equation
OSI	Oscillatory Shear Index
PC-MRI	Phase-Contrast Magnetic Resonance Imaging
PcoA	Posterior Communicating Artery
PDE	Partial Differential Equation

PIV	Particle Image Velocimetry
PWV	Pulse Wave Velocity
R/L ACA (A1)	Right/Left Anterior Artery
R/L ICA	Right/Left Internal Carotid Artery
R/L MCA	Right/Left Middle Cerebral Artery
R/L PCA (P1)	Right/Left Posterior Artery
RMSWSS	Root Mean Square Wall Shear Stress
RCR	Resistance-Compliance-Resistance
RL	Resistance-Inductance
SA	Subclavian Artery
SVC	Superior Vena Cava
TCD	Trans-Cranial Doppler ultrasonography
THINKS	Total Human Intravascular Network Simulation
TVD	Total Variation Diminishing
UIA	Un-ruptured Intracranial Aneurysm
VA	Vertebral Artery
WSS	Wall Shear Stress

## **Acknowledgments**

I would like to deeply thank my supervisors Dr. George Huang and Dr. Zifeng Yang for their patience, guidance, and encouragement throughout my Ph.D. study. I would like to thank Dr. Bryan Ludwig for sharing his medical experiences and knowledge of cerebrovascular diseases. I would also like to thank Dr. Joseph Shang and Dr. Philippe Sucusky for their valuable comments on the final dissertation. Finally, to my family and my dear friends who supported me during my studies.

# 1 INTRODUCTION

## 1.1 Background

### 1.1.1 Cardiovascular system

In the human body, blood transports oxygen, carbon dioxide, and hormones to and from all tissues of the body. Blood flows through the cardiovascular network consisting of the heart, pulmonary circulation, blood vessels, and microcirculation beds. The blood circulation can be separated into two sections: the pulmonary and the systemic circulations. Blood is oxygenated in the pulmonary circulation, and the heart pumps the oxygenated blood into the systemic to circulate through arteries, veins, capillaries, and back to the heart, as shown in Figure 1.1 (b). The primary function of the vessels is to deliver nutritive substance and oxygenated blood to tissues of the body. The deoxygenated blood is carried by the pulmonary trunk from the heart to the lungs to gain oxygen. After supplying oxygen to tissues, deoxygenated blood from tissues and muscles are taken back to the heart through venules and veins.

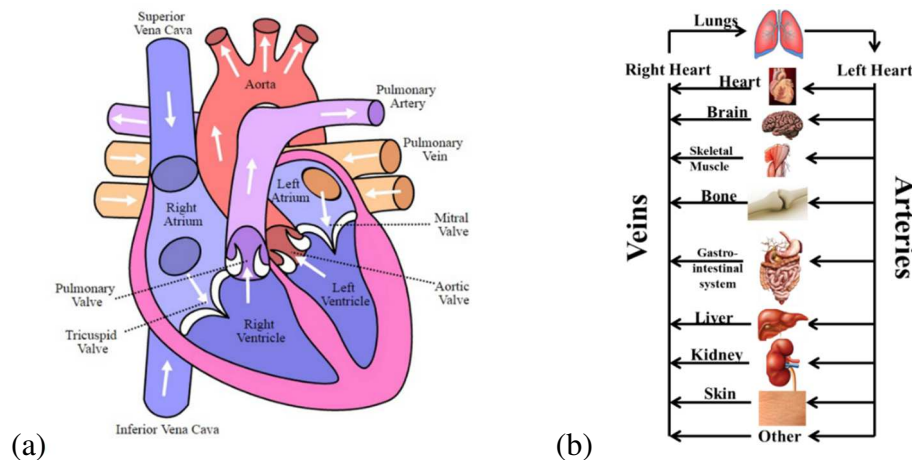


Figure 1.1 The cardiovascular system and the anatomy of the heart. (*Anatomy of the Heart*, 2016)

The heart is a muscular organ, which pumps blood through the blood vessels of the circulatory system (Taber et al., 2009). The heart consists of four chambers, left/right atria and ventricles, as shown in Figure 1.1. The right atrium collects blood flowing from the systemic veins, including superior vena cava, inferior vena cava, and coronary artery, and then pump it into the right ventricle. Blood in right ventricle is delivered to the lungs through the pulmonary vessels for oxygenation. From the lungs, it flows back to the left atrium through the pulmonary veins and into the left ventricle and pumps out to the ascending aorta root going through all the tissues and muscles of the body via the arterial network. The cardiac muscles are made of dense connective tissues, which give structure to the heart, forming the atrioventricular septum which separates the atria from the ventricles, and the fibrous rings which serve as bases for the four heart valves (Pocock, 2006). The valves ensure blood flows in the correct direction through the heart and also prevent backflow.

The root systemic artery is called aorta which connects the left ventricle and receives blood directly from the left ventricle of the heart. The aorta is the largest artery ( $D \sim 3$  cm) in the human body, and the branches from the aorta become successively smaller in diameter, down to the arterioles ( $D \sim 0.2$  cm). The first branches of the aorta are the coronary arteries, which supply blood to the heart muscles. Other branches supply blood to organs and muscles performing crucial functions, such as the renal system and the digestive system. The blood is stripped of oxygen in the capillaries inside these organs, and the deoxygenated blood is taken back by the venules through the venous system. The veins grow larger as they merge and the largest veins, Superior and Inferior Vena Cava, deliver blood back to the heart.

The blood pressure varies in different locations of the body. The arterial network is directly connected to the high-pressure left side of the heart, so the pulse pressure is determined by the compliance of the aorta and the contraction of the left ventricle. Then, the pulse pressure becomes larger in the downstream because of the less compliant arteries. Systemic arteries can be subdivided into two types, muscular and elastic, according to the related compositions and muscle tissue in their tunica media and their size and the makeup of the internal and external elastic lamina. The larger arteries contain elastic tissue and smooth muscle that provides dynamic tension within the vessels to act against the transmural pressure.

#### 1.1.2 Cerebral aneurysm

A cerebral aneurysm is a weakened spot on a blood vessel in the brain and it balloons out and fills with blood. An aneurysm may rupture, leaking blood to surrounding tissues resulting in hemorrhage or stroke. The dominance of cerebral aneurysms is estimated to be 2-5 % in the general population, and the rupture of an aneurysm results in subarachnoid hemorrhage which is the leading cause of stroke mortality and morbidity (Zacharia et al., 2010). A cerebral aneurysm can be generated congenitally, or as a result of genetic diseases. It also can occur from trauma or injury to the head, high blood pressure, infection, tumors, atherosclerosis, and other diseases of the vascular system. There are three types of cerebral aneurysms: a saccular aneurysm balloons out on one side of the artery, a fusiform aneurysm is formed by the widening along all sides of the vessel wall, and the last type is called pseudo-aneurysm which is formed inside the layers of a blood vessel wall. Figure 1.2 shows cerebral aneurysms located in the CoW.

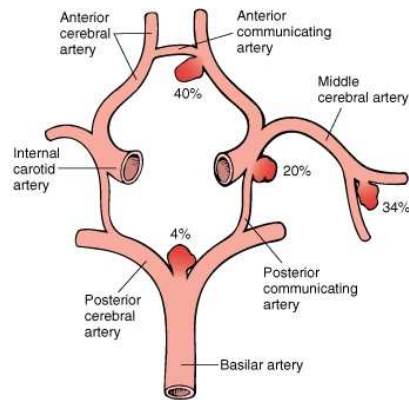


Figure 1.2 Various cerebral aneurysms located on the CoW.

Previous studies based on hemodynamic hypotheses have correlated aneurysm pathophysiology with a hemodynamic insult (blood flow impingement, pressure, and WSS) (Meng et al., 2014). Conflicting findings regarding “high-versus-low” WSS were reported during the past decade. Moving toward the goal of a unifying, it is proposed that both high and low wall shear stress can drive IA growth and rupture through different pathways. An inflammatory-cell-mediated pathway is associated with low WSS and high oscillatory shear index, while a mural-cell-mediated pathway is associated with high WSS with a positive gradient (Meng et al., 2014). Other genetic and environmental risk factors, including hypertension, cigarette smoking, and genetic predisposition may make the cerebral arteries more vulnerable to the hemodynamic insult, and complicate underlying molecular pathways pertinent to the IA initiation. IA initiation induces increased matrix degradation, which can be indicated by loss of internal elastic lamina and upregulation of matrix metalloproteinases. It has been recently demonstrated that both nitric oxide production from endothelial nitric oxide synthase and superoxide could elicit smooth muscle cells phenotype change and MMP production and thus lead to IA initiation in response to hemodynamic insult (Meng et al., 2014). Therefore, it is clear that hemodynamic anomalies play a critical role in the initiation of aneurysms.

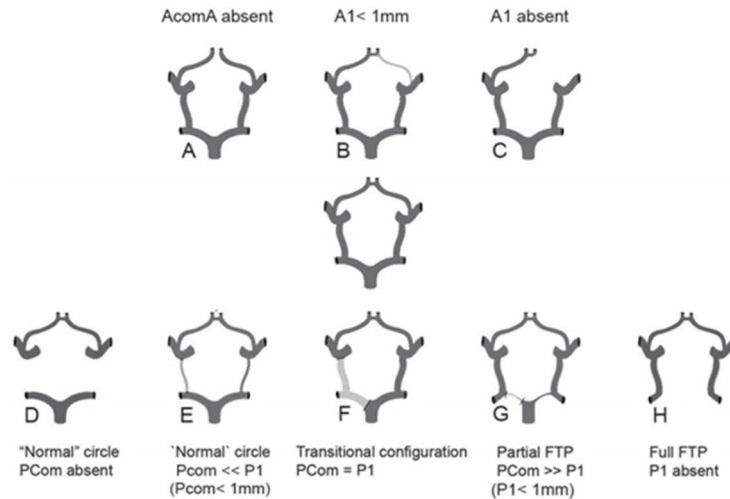


Figure 1.3 Variations structure of the CoW. The middle one represents the complete CoW. A-H represent the variations in the anterior and posterior parts.

A small cerebral aneurysm with a diameter less than seven millimeters will not show symptoms; while a more significant, steadily growing aneurysm could damage surrounding tissues and nerves, resulting in pain, numbness, weakness, and vision changes. On the other hand, a ruptured aneurysm causes hemorrhages, possibly resulting in sudden and extremely severe headache or loss of consciousness. Statistically, the most common sites that an aneurysm occurs are in the CoW and the bifurcations of the vessels. In addition, the CoW is a circulatory anastomosis that supplies blood to the brain and surrounding tissues (Uston, 2005). The arrangement of the brain's arteries into the CoW creates redundancies or collaterals in the cerebral circulation. If a section of the circle becomes blocked or narrowed, blood flow from other blood vessels can preserve the cerebral perfusion enough to avoid the symptoms of ischemia. Variations of the CoW are presented in Figure 1.3 (De Boorder et al., 2006).



## 1.2 Motivations and objectives

Numerous statistical studies indicate that the hemodynamic characteristics take significant effect on the initiation, development, and rupture of a cerebral aneurysm. However, obtaining comprehensive hemodynamic parameters directly from patients remains a challenge because of the technical difficulties and the small and tortuous arteries in the brain. Hence, three-dimensional (3D) simulation of patient-specific morphological models has been widely used to provide the hemodynamics information of individual patients. Since geometries were only restricted locally, BCs are required to carry out the CFD computations. The boundary conditions were obtained from a direct measurement of the flow rate from medical images, such as Doppler ultrasound technique. Experimental uncertainties of the measured waveforms may affect the accuracy of time-dependent patient-specific boundary conditions. Moreover, the BCs may be altered by changes of local vascular deformation caused by the disease and therefore unless the computational domain is sufficiently large, the feedback from the pressure loss of the 3D segment may not be properly interpreted.

The present work aims to develop a coupling approach to investigate how the local vessel deformation caused by the associated vascular disease induces flow alterations within the vessel network. To achieve this goal, a previously published closed loop 1D numerical model containing the entire human vessel network is employed to compute the flow rate and blood pressure waveforms in the flow network. In the meantime, the 1D model considers the vascular aging effects to investigate how the vascular aging effects on hemodynamic characteristics in the cardio- and cerebrovascular systems, especially the flow conditions in the CoW. A 3D patient-specific aneurysm model is reconstructed

based on personal DSA image slices, and two additional morphologies are created based on the original anatomy, such as an enlarged and a bilobed model. The 3D CFD simulations are conducted by applying the flow conditions extracted from the 1D numerical model corresponding to the arteries in the 3D geometry, aiming to explore the effects of the shape and size on the hemodynamic parameters (e.g., pressure, WSS, OSI, and flow patterns). Having the 1D and 3D computational models accomplished, the 1D-3D multi-scale model is developed by directly exchanging the flow rate and pressure gradients information between the 1D and 3D models. This coupling approach is used to investigate the global hemodynamic changes induced by the local morphological effects. Overall, the main contribution of the current dissertation includes the investigation of the vascular aging on the hemodynamics of blood flow and the development of the multi-scale model, which can be used as an alternative to current approaches to study intracranial vascular diseases such as an aneurysm, stenosis, and combined cases.

## 2 LITERATURE REVIEW

### 2.1 1D numerical calculation of blood flow

Recently, CFD simulation approach of the blood flow has been widely employed to predict the hemodynamics of patient-specific segments. The flow motion of blood is governed by 1D Navier-Stokes continuity and momentum equations. Most previous studies adopted linear or nonlinear constitutive equations to compute the pressure and cross-sectional area relationship (Alastruey et al., 2011; Alastruey et al., 2008; Alastruey et al., 2012; Alastruey et al., 2007; Blanco et al., 2013; Blanco et al., 2015; Huang et al., 2015; Liang et al., 2015; Liang et al., 2011, Liang et al., 2009; Liang et al., 2009; Liang et al., 2005; Müller et al., 2014; Yu et al., 2016; Mynard et al., 2008; Mynard et al., 2015; Sherwin et al., 2003; Reymond et al., 2011; Montecinos et al., 2014; perdikaris et al., 2015). The 1D governing equations for the pulse wave propagation is examined by the two Riemann variables to decouple the area and the volumetric flow rate. To simulate the hemodynamics of blood flow, two simulation approaches were developed from previous reports to treat the boundary conditions: open-loop and closed-loop. The former is to apply the pulsatile flow rate obtained from the measurement data or theoretical derivations as the inlet boundary condition and coupled with lumped parameter models (0D) at the terminals of the vessel network, using the electrical analog approach with resistance, capacitor, and impedance to represent the flow resistance, blood vessel compliance and flow inertia. On the contrary, the flow condition of the latter is calculated from lumped parameter models of the heart and pulmonary circulation. Similarly, 0D models were used at the outlets, but they were connected to the right atrium of the heart

model to be considered as a closed-loop simulation. Herein, the capillary circulation system is computed as 0D models.

Blanco et al., (2015) reconstructed an Anatomically Detailed Arterial Network (ADAN) model which contains 1,497 named arteries and 544 smaller vessels. The hemodynamics of this blood vessel network has been investigated. In this 1D model, the blood pressure was treated by accounting for the effects of elastin, collagen, and smooth muscle, and assigning different parameters of these factors to the vessels based on their radius. The sensitivity of the arterial stiffening regarding perturbations of parameters at different vascular regions has been conducted (Blanco et al., 2015). A local perturbation method was used to carry out the sensitivity study assessing the effects of the model parameters on the differential impact. Additionally, the wave propagation of blood flow in fifty-five larger arteries was calculated by Wang et al., (2004) in the closed-loop 1D model. The inflow waves were computed by the heart, and the terminals of the arteries were connected by resistance elements to provide reasonable pressure wave reflections. The pressure waveform can be separated into forward and backward wave components. The former wave is generated by the heart contraction, while the latter wave is induced by the vessel bifurcations and terminal resistance (Wang et al., 2004). The phenomenon of increased pressure wave with the distance away from the heart has been captured. Also, the occlusion of different arteries was modeled to investigate the changes in the flow rate and blood pressure waveforms (Wang et al., 2004).

Muller et al., (2014) developed a closed-loop 1D numerical model to simulate the entire human vessel network including arterial and venous circulation systems. The calculation of the 1D model starts from the heart and pulmonary circulation which is modeled as

lumped parameter models. The pulsatile blood flow moves through the arterial, capillary, and venous circulation systems and then flowing back to the heart. Hence, the flow rate and blood pressure waveforms in each artery and vein can be obtained (Muller and Toro, 2014). In the meantime, Huang et al., (2015) developed a closed-loop 1D numerical model of the similar vessel network to reproduce the flow rate and blood pressure waveforms using a TVD numerical scheme. Validation studies were presented by comparing the computed results with manipulated solutions. Moreover, a detailed adult vessel network has been modeled by Mynard et al., (2015), which contains the heart and pulmonary, coronary, microcirculation, and arterial-venous systems, resulting in a total of 396 vessels and 188 junctions. The investigations focused on the forward and backward wave intensities in different segments and the interactions between the heart and vascular waves.

The influence of aging on the hemodynamic characteristics of blood flow has been studied by Liang et al., using a closed-loop 0D-1D model. The heart and capillary circulations were simulated by 0D models, while the arterial and venous systems were computed in 1D. The flow rate and blood pressure wave propagation were compared with patients in each decade. During aging, the heart and blood vessel walls become stiffer, resulting in an increase in the preload of the left ventricle to cause heart and vascular diseases (Liang et al., 2009; Yu et al., 2016). The applications of this 1D model on the aortic valvular and arterial stenoses were examined by applying stenosis numerical equations in the heart valves and different artery segments (Liang et al., 2009). The results demonstrated that the 1D model is able to capture the changes in the flow rate and pressure waveforms when stenosis occurred in arteries (Liang et al., 2009).

To validate the accuracy of the 1D model, The flow rate and pressure waveforms have been compared between a 1D numerical model and a well-defined experimental 1:1 replica of the 37 main human arteries model by Matthys et al.. (2007) and Alastruey et al., (2011). The experiment adopted a silicone network of the arteries model assembled by connectors and a pulsatile pump to provide the pulsatile inflow. The comparisons of the flow rate and pressure waveforms showed that the 1D model is able to capture the main features of the pulse wave propagation of the experimental data.

Regarding the hemodynamics of the blood flow in the CoW, the system of the auto-regulation of blood flow has been studied by Alastruey et al., (2008) using a 1D numerical model coupled with lumped parameter models at the terminals. The auto-regulation of blood flow is caused by the brain metabolism due to the blood nutrition changes through the bloodstream and the relaxation of the surrounding tissues. Thus, the terminal resistance is changing during the process and able to redirect the flow distributions in the CoW. One scenario of the lack of supplement of blood due to the absence of an artery in the CoW demonstrated that the anterior communicating artery plays important roles in compensating for the particular variation of the CoW. Additionally, the flow rate and blood pressure waveforms in the variations of the CoW were investigated by Alastruey et al., (2007) the 1D numerical model. The physiological data was adopted from the previously published report. The results concentrated on the flow and pressure waveform comparison of the complete CoW with incomplete variations of the CoW configurations, including the absence of artery AcoA, R/LPcoA, R/LACA, R/LPCA, and both R/LPCA and R/LPcoA. The simulated results indicated the importance of AcoA to maintain the perfusion in the brain if the ICA or ACA is occluded.

In the other scenario, when the VA is occluded, PcoAs would play essential roles in remaining the flow distributions in the CoW. The similar hyperperfusion phenomenon of the CoW when absent or occlusion of arteries was also investigated by Liang et al., (2011) by using a 1D closed-loop numerical model. It is known that the stenosis or missing arteries occurred in the CoW would activate the auto-regulation function of the CoW to maintain the flow distributions in different areas in the brain.

Regarding the 0D model used in the 1D calculation, different electrical analog models defined at terminations of arteries contribute various effects on the global hemodynamics. A current study has summarized the functions of various lumped models by Alastruey et al., (2008). It is indicated that the inflow resistance could avoid non-physiological reflections, meaning more energy can be absorbed by a resistor at the terminal. Also, the mean pressure and flow rate in arteries computed from 1D model highly relies on the terminal resistances but not as much on the compliance (Alastruey et al., 2008). To fully understand the behavior of the global hemodynamics of the blood flow, a closed-loop 0D model has been developed by Liang et al., (2005) with a detailed explanation of the heart-pulmonary and vascular circulation systems. The 0D model was calculated using an electrical analog approach to represent the blood flow resistance, vessel wall compliance, and the impedance of blood flow. The 0D model has assigned different volume-elastance parameters to the heart, arterial, and venous walls (Liang et al., 2005).

A benchmark study of the 1D model has been conducted by Boileau et al., (2015) by comparing the simulated results solved with various numerical schemes, a 3D numerical model, and previous experimental data. (Xiao et al., 2014; Matthys et al., 2007; Alastruey et al., 2011; Blanco et al., 2014; Blanco et al., 2015). The tested 1D model was solved by

different numerical schemes, such as discontinuous Galerkin, locally conservative Galerkin, Galerkin least-squares finite element method, finite volume method, finite difference MacCormack method and a simplified scheme that spatially integrates the mass and momentum equations along the vessel axis using the trapezium rule method (Formaggia et al., 2003; Sherwin et al., 2003; Bessems et al., 2007; Steele et al., 2003; Toro et al., 2013; Muller et al., 2013; Azer et al., 2007). It is demonstrated that the arterial pulse wave propagation can be modeled using these numerical schemes and the 1D model is able to provide a quick insight of the hemodynamics of blood flow to aid in vascular disease treatment strategies.

## 2.2 3D CFD simulations of cerebral aneurysms

To evaluate the risks of a cerebral aneurysm, the hemodynamic characteristics of a cerebral aneurysm model have been considered to associate with the rupture of an aneurysm. However, directly measuring of such hemodynamic parameters, such as pressure, wall shear stress, and flow patterns remains a challenge due to the current technique. So, the 3D CFD simulation tool has been widely used to predict the flow parameters of a patient-specific aneurysm model. Hemodynamic parameters are mainly induced because of the friction between blood flow and vessel wall. The pulsatile blood pressure could cause tensile stresses on the wall. When the distribution of tensile stresses is unbalanced, it could activate medial cell-mediated collagen synthesis and cross-linking and collagen degradation, which contributes the rupture of an aneurysm (Humphrey et al., 2008). On the other hand, the rupture of an aneurysm can be attributed to wall stresses, which further trigger local wall weakening of an intracranial aneurysm due to a local pathological morphology. To investigate the effects of the wall shear stress on the rupture



of an aneurysm in CFD simulation, time-averaged WSS is widely considered as the main index and plotted as a surface distribution. Occasionally, however, instantaneous WSS at peak systole or diastole in the cardiac cycle is used instead of investigating time-averaged WSS (Xiang et al., 2014).

The 3D patient-specific aneurysm models are reconstructed based on the MRA or DSA imaging data scanned directly from patients. Since the resolution of the imaging data is quite sensitive to the measurement operations and the patient's physical conditions, the created geometry would include a tremendous amount of redundant elements, requiring cleaning through surface smoothing, filling holes, eliminating redundant elements and reconnecting branches (Yang et al., 2015). To accurately simulate the blood flow, the effect of the Newtonian and non-Newtonian fluid for the blood flow simulation on the hemodynamic results has been summarized by Xiang et al. (2011). The WSS distribution of three patient-specific ICA aneurysm models was predicted with the Newtonian viscosity model and two Non-Newtonian models (Casson and Herschel-Bulkley). The difference of the predicted WSS between the fluid models is approximately less than 5% in quasi-spherical and bifurcation aneurysm models primarily found around the dome region of an aneurysm. However, for the oblong, complex, ICA aneurysm shape, a 55-60% difference in the dome region can be observed from non-Newtonian models as compared to the Newtonian model in time-averaged WSS distribution. Furthermore, identical flow patterns inside all aneurysm models were observed with different flow assumptions. It is demonstrated that the Newtonian model is acceptable for aneurysm models which don't have low shear regions. Aneurysms with low shear flow regions, the non-Newtonian model, should be considered, particularly in aneurysms with the complex, oblong shape.

Sometimes, non-Newtonian models may underperform. When simulated blood has high shear rates to behave a constant viscosity, the non-Newtonian model could cause unrealistically lower viscosity values, resulting in low viscosity value occurring in parent vessels (Xiang et al., 2011).

In a study of twenty middle cerebral aneurysms (three ruptured and seventeen unruptured) implemented by Shojima et al. (2004), the spatial-averaged WSS over the aneurysm region has been compared between ruptured and unruptured aneurysms. The results indicated that larger WSS occurred in the unruptured aneurysms, which is about two times greater than that of ruptured ones. Moreover, the low magnitude of the WSS has been found in both rupture and unruptured aneurysm models, which are not able to mechanically induce the rupture of an aneurysm. It turns out that the low WSS would trigger biological signals on endothelial cells to modify the cellular functions (Gibbons et al., 1994).

Indeed, Xiang et al., (2011) identified the effects of morphological and hemodynamic characteristics on the rupture of cerebral aneurysms by investigating 119 intracranial aneurysms (38 ruptured, 81 unruptured). Studies have been categorized into three groups: morphological factors, hemodynamics, and morphological and hemodynamic combined. It is indicated that ruptured aneurysms tend to have complex flow patterns with more than one vortex inside the aneurysm sac compared to un-ruptured aneurysms resulting in increasing inflammatory cell infiltration in the aneurysm wall. The complex flow pattern could trigger a large OSI which measures the directional change of WSS during the cardiac cycle. From the results, the low magnitude of WSS has been observed in ruptured aneurysm models compared to the unruptured aneurysms, which agrees with the findings

by Shojima et al. (2004). More specifically, Boussel et al., (2008) and Dhar et al., (2008) indicated that the low WSS and high OSI are commonly involved in aneurysms of complex or stretched shapes, such as large size ratio, undulation index, and aspect ratio. These factors are also associated with the growth and rupture of an aneurysm.

Additionally, Cebal et al., (2011) proposed the relationship between hemodynamic characteristics and the aneurysm pathogenesis, progression, and rupture. In this report, a total of 210 cerebral aneurysm models were predicted with different flow conditions, and quantitative hemodynamic parameters and statistical analysis were defined and conducted (Cebal et al., 2011). The statistical results show that large inflow concentration, large maximum WSS, large shear concentration, and low viscous dissipation ratios could be observed in ruptured aneurysms compared to unruptured ones. Enlarged aneurysms appear to be governed by the interaction between hemodynamic loads and mechanobiology response of the cellular elements of the wall, resulting in a weakening of the wall (Chatziprodromou et al., 2007).

Griffith et al., (1994) reported that the low-flow theory points to localized stagnation of blood flow against the wall in the dome as causing a dysfunction of the endothelium, as well as accumulation and adhesion of platelets and leukocytes along the intimal surface, which encourages intimal damage, inflammation, and subsequent wall degradation. The aneurysm wall progressively thins and may result in a tearing of the tissue.

The formation of a cerebral aneurysm is found to be associated with the configuration of the circle of Willes. Krasny et al., (2014) assessed the prevalence of aneurysms in patients with morphological variations of the CoW. It has been demonstrated that variations in the circle of Willis take significant effect on the development and

occurrence of cerebral aneurysms. The investigated data revealed a clear correlation between variations of the anterior circle and cerebral aneurysms (aplasia 10%; hypoplasia 52.91%). From the hemodynamic theory, the data showed that an AcoA aneurysm tends to occur with grade-I ACA hypoplasia, and large aneurysms would be formed with grade II hypoplasia. Moreover, SilvaNeto et al., 2012 revealed low incidence of fetal type PcoA in patients with AcoA aneurysms. The fetal type PcoA is associated with high flow rates in the carotid system, and low flow rates in the basilar artery.

In conclusion, the possible reasons for rupture of a cerebral aneurysm have been statistically studied, and the risk factors of cerebral aneurysms have been summarized by Cebal et al., (2013). Some factors take essential effects on biological processes in vessel walls. In the study of aneurysms, the wall tension and hemodynamic characteristics can be defined based on the blood vessel wall properties and flow conditions. The size and shape of an aneurysm affect the flow patterns inside an aneurysm, as well as the artery angle of the parent artery. Thus, the wall remodeling and thrombus generation and subsequent inflammation could be related to the hemodynamic characteristics. On the other hand, the aneurysm location is also associated with determining the hemodynamics, which also causes the changing of wall structure (Cebal et al., 2013).

### 2.3 0D-1D-3D multi-scale simulation

Three-dimensional modeling is a powerful tool for studying hemodynamics of blood flow. However, building a comprehensive 3D model representing the entire cardiovascular system is challenging. Thus, the multi-scale model was used to consider the global systemic changes due to a local pathological morphology, such as a cerebral aneurysm and stenosis. It combines the 1D and 3D models by passing the flow and pressure

information between each side and has gained more consideration to evaluate the risk factors and provide valuable treatment options for local vascular diseases (Pontrelli, 2004; Nobile, 2009; Papadakis, 2009; Cristiano et al., 2013).

Formaggia et al., (1999) claimed that a local pathological morphology, such as stenosis, may have global effects on the flow distributions resulting from the large pressure loss induced by the changes in diameter of the vessels. To analyze blood flow simulation in compliant vessels, Formaggia et al., (2001) developed a multi-scale model coupling between a 3D fluid-structure model and a 1D reduced model. The interaction between the 1D and 3D models is to pass the area, mean pressure, flux, and boundary characteristic functions between two models. Two simple geometries were tested, and the results indicated that this proposed multi-scale model allows for simplification of the computational complexity, and the outgoing pressure waves can be suitably absorbed (Formaggia et al., 2003; Formaggia et al., 2009).

However, some researchers used different methods to treat with interfaces between different dimensionalities. A unified variational approach for coupling 1D and 3D models was proposed by Blanco et al., (2007). The treatment of the 1D and 3D coupling method can be considered as discontinuous fields arise because of the difference in the kinematics assumed for different domains. A case of a wave traveling along multidimensional arteries model was used to test the proposed method. This 1D-3D model was applied to solve a blood vessel network coupled with 3D segments of the femoral artery, common carotid artery, and cerebral aneurysm models, respectively. The hemodynamic characteristics of blood flow investigated by presenting the pressure and flow waveforms in specific arteries and wall shear stress and streamlines of the 3D

models (Blanco et al., 2009). Furthermore, an integrative closed-loop 0D-1D model was established by Blanco et al., (2010) to investigate the aortic valve regurgitation disease and the influence of the hemodynamic variables. After developing the 0D-1D model, a patient-specific aneurysm model was inserted into the 0D-1D model to come up with the 0D-1D-3D model. The effects of the local aneurysm model on the global factors, such as heart rate, peripheral resistance, and blood pressure, were briefly discussed (Blanco et al., 2010).

On the other hand, Passerini et al., (2009) developed a multi-scale model by coupling the compliant 1D model and a rigid 3D segment. The interfaces between the 1D and 3D models were used 0D models working as a medium to exchange the flow and pressure information from each side. The comparisons were made among the 1D model, a multi-scale model with null 0D, and multi-scale model with activated 0D. It is demonstrated that the activated 0D model is able to reduce the flow rate oscillation because the compliance component in the 0D model can help the pressure wave propagation between the 1D and 3D models (Passerini et al., 2009). Instead of solving the 3D model through programming, Liang et al., (2015) established a software-based multi-scale model employed cardiac-cycle-dependent coupling method to implement the multi-scale model, where the computational method ignored the deformation of vessel walls due to high computational cost. The main procedures for solving the interface were to apply the respected flow rates to the 3D simulation as BCs. After the 3D computation converging, the 3D model transferred back the pressure at inlet and outlets to the 1D model to recalculate a new flow rate. The iteration stops when the difference of the mean pressure between the 1D and 3D models reaches the convergence tolerance (Liang et al., 2015).

Recently, a full 3D model considered to compute the blood vessel network (Vignon-Clementel et al., 2006; Xiao et al., 2013; Xiao et al., 2014). Vignon-Clementel et al., (2006) discussed the effects of the lumped parameter models as the outflow conditions on the flow distributions, velocity, and pressure fields for a 3D model calculation by presenting the hemodynamics with three test cases, a straight artery, a stenotic abdominal aorta, and a patient-specific abdominal aorta model. Furthermore, Xiao et al., (2013) presented a full-body 3D arterial network computation. A full 3D model was reconstructed from two different patients with tomographic angiography image data. The flow rate in the ascending aorta and lumped parameter models were used as the inlet and outlet BCs, respectively. The 3D computation is able to obtain hemodynamic characteristics including the deformation of vessel walls due to the altered blood pressure, the vessel wall dynamics, and complex flow patterns. The validation studies of the 3D model computation were presented by using a bunch of artery models, such as a single artery, single bifurcation, and an aorta model by comparing the 3D results with those obtained from the 1D model (Xiao et al., 2014).

### 3 METHODOLOGY

In this chapter, the methodologies involved in the entire dissertation will be presented. Section 3.1 introduces the 1D numerical model, including the numerical schemes, blood vessel network, and lumped parameter models. In Section 3.2, the experimental setup of blood flow in a complete CoW will be described. The 1D model is extended to investigate the vascular aging effects, and the simulation approach will be presented in Section 3.3. Section 3.4 describes the reconstruction of patient-specific segments and the detailed setup of the 3D CFD simulation. The concentrated hemodynamic parameters in this dissertation will be introduced in Section 3.5. Last but not the least, Section 3.6 proposes the multi-scale model by linking the 1D and 3D models, and the methodologies will be elaborated.

#### 3.1 0D-1D model

Huang et al., (2015) and Müller et al., (2014) introduced a 1D numerical modeling of blood flow to simulation the hemodynamics in the circulation system of a human body. The 1D model contains both the arterial and venous circulation systems consisting of eighty-five major arteries, 158 major veins, seventy-seven venous and forty-three arterial junctions, as presented in Figure 3.1. Microcirculation in capillaries and venules, the motion of the heart, and pulmonary circulations were modeled as lumped parameter models (0D).



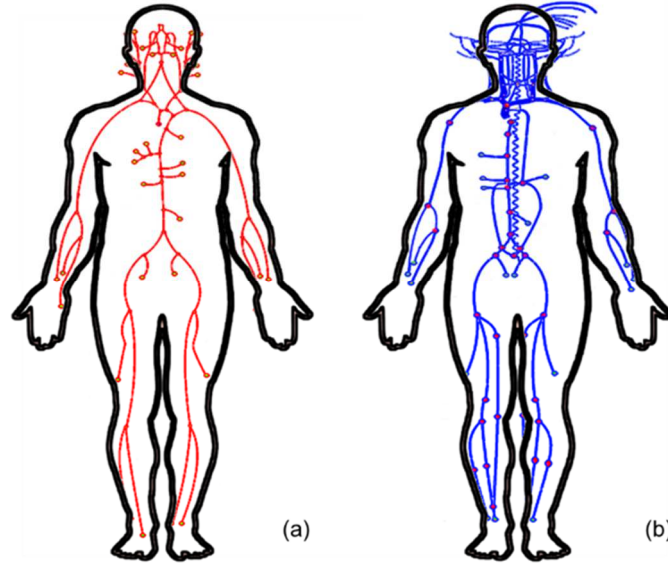


Figure 3.1 Arterial and venous network consists of eighty-five arteries and 158 veins; (a) represents the arterial circulation system; (b) represents the venous circulation system

### 3.1.1 Governing equations

The governing equation of 1D blood flow derived from conservation of mass and momentum of incompressible and Newtonian fluid is given by (Huang et al., 2015; Müller et al., 2014):

$$\frac{\partial A}{\partial t} + \frac{\partial q}{\partial x} = 0, \quad (1a)$$

$$\frac{\partial q}{\partial t} + \frac{\partial}{\partial x} \left( \alpha \frac{q^2}{A} \right) = -\frac{A}{\rho} \frac{\partial p}{\partial x} - f / \rho, \quad (1b)$$

where  $t$  is time;  $x$  is the axial coordinate along the artery and vein;  $A$ ,  $q$ , and  $p$  represent the cross-sectional area, the volume flux, and the average internal pressure, respectively;  $\rho$  is the density of the blood and was assumed to be  $1050 \text{ kg/m}^3$ ;  $\alpha$  is kinetic energy coefficient, a value of 1 is used by assuming a blunt velocity profile in cross section.  $f$  is the friction force per unit length of the vessel, which is dependent on the chosen velocity profile, herein taken to be  $f = -8\mu\pi U$  (Alastruey et al., 2012).

The internal pressure to the cross-sectional area of the vessel in equation (1b) can be expressed as:

$$P(x, t) = P_e(x, t) + \Psi(x, t), \quad (2)$$

where  $P_e(x, t)$  is the external pressure exerted by tissues surrounding vessels;  $\Psi(x, t)$  is the transmural pressure which is the pressure difference between internal and external and is given by:

$$\Psi(x, t) = K(x)\phi(A(x, t), A_o(x, t)) + P_o, \quad (3)$$

where  $K(x) = \frac{E(x)h_o(x)}{(1-\nu^2)R_o(x)}$ , where  $E(x)$  represents the Young modulus;  $h_o(x)$  represents the blood vessel wall thickness;  $\nu$  represents the Poisson's ratio.  $P_o$  is the reference pressure at which  $A = A_o$ . The function  $\phi(A(x, t), A_o(x, t))$  is assumed to be of the form:

$$\phi(A(x, t), A_o(x, t)) = \left(\frac{A(x, t)}{A_o(x, t)}\right)^m - \left(\frac{A(x, t)}{A_o(x, t)}\right)^n, \quad (4)$$

The parameters of  $m$  and  $n$  computed from experimental measurements, for arteries,  $(m, n) = (0.5, 0)$ , and for veins,  $(m, n) = (10, -1.5)$  (Huang et al., 2015 and Müller et al., 2014).

Therefore, substitute equations (2, 3, 4) into equation (1), the momentum equation can be rewritten into:

$$\frac{\partial q}{\partial t} + \frac{\partial}{\partial x} \left( \alpha \frac{q^2}{A} \right) + \frac{A}{\rho} K \frac{\partial \phi}{\partial x} \frac{\partial A}{\partial x} = -\frac{A}{\rho} \left( \frac{\partial P_e}{\partial x} + K \frac{\partial \phi}{\partial A_o} \frac{\partial A_o}{\partial x} + \phi \frac{\partial K}{\partial x} \right) f / \rho, \quad (5)$$

### 3.1.2 Discretization

In this work, the TVD scheme is adopted as the basis of the approach (Yee, 1987). Herein, the physical part of the governing equation is expanded based on the central differencing scheme, whereas a TVD section is developed in discontinuity interfaces to provide a stable solution for the numerical part.

Equation (1) and (2) can be rearranged in terms of matrix form as:

$$\frac{\partial Q}{\partial t} + \frac{\partial F}{\partial x} + H \frac{\partial P}{\partial x} = S, \quad (6)$$

where

$$Q = \begin{bmatrix} A \\ q \end{bmatrix}, F = \begin{bmatrix} q \\ q^2 / A \end{bmatrix}, H = \begin{bmatrix} 0 & 0 \\ 0 & A / \rho \end{bmatrix}, P = \begin{bmatrix} 0 \\ p \end{bmatrix}, \text{ and } S = \begin{bmatrix} 0 \\ -f / \rho \end{bmatrix}, \quad (7)$$

After discretizing equation (6), the equation can be expressed as

$$\frac{\partial Q}{\partial t} = -\frac{1}{\Delta x} (F_{i+1/2} - F_{i-1/2}) - H_i \frac{1}{\Delta x} (P_{i+1/2} - P_{i-1/2}) + S_i + \frac{1}{\Delta x} (D_{i+1/2} - D_{i-1/2}), \quad (8)$$

where the values at the interfaces,  $i+1/2$ , can be obtained by the geometrical averaging of the values at former and latter interfaces,  $i+1$  and  $i-1$ . And, a numerical flux is derived from Equation (5), and for the first order scheme, it can be written as

$$D_{i+1/2} = \frac{1}{2} R_{i+1/2}^{-1} |\Lambda_{i+1/2}| R_{i+1/2} \begin{bmatrix} \delta_{i+1/2} A \\ \delta_{i+1/2} q \\ \delta_{i+1/2} K \\ \delta_{i+1/2} A_o \\ \delta_{i+1/2} p_e \end{bmatrix}, \quad (9)$$

where  $\delta_{i+1/2}$  is the differencing operator between  $i+1$  and  $i$  points:

$$R = \begin{bmatrix} -\frac{c+u}{A} & \frac{1}{A} & \frac{\phi}{\rho(u-c)} & \frac{K(\partial\phi/\partial A_o)}{\rho(u-c)} & \frac{1}{\rho(u-c)} \\ \frac{c-u}{A} & \frac{1}{A} & \frac{\phi}{\rho(u+c)} & \frac{K(\partial\phi/\partial A_o)}{\rho(u+c)} & \frac{1}{\rho(u+c)} \end{bmatrix},$$

$$\Lambda = \begin{bmatrix} |u-c| & 0 \\ 0 & |u+c| \end{bmatrix}, \quad (10)$$

$$R^{-1} = \begin{bmatrix} -\frac{A}{2c} & \frac{A}{2c} \\ \frac{A(c-u)}{2c} & \frac{A(c+u)}{2c} \end{bmatrix},$$

and

$$c = \sqrt{\frac{A}{\rho} K \frac{\partial \phi}{\partial A}} = \sqrt{\frac{K(x)}{\rho} \left[ m \left( \frac{A(x,t)}{A_0(x,t)} \right)^m - n \left( \frac{A(x,t)}{A_0(x,t)} \right)^n \right]}, \quad (11)$$

To solve Equation (8), two Riemann variables,  $W_1$  and  $W_2$ , are defined to decouple the unknowns,  $A$  and  $q$ , and the equation can be written as:

$$\begin{aligned} \delta W_1 &= \delta u - \frac{c}{A} \delta A + \frac{\phi}{\rho(u-c)} \delta K + \frac{K(\partial \phi / \partial A_o)}{\rho(u-c)} \delta A_o + \frac{1}{\rho(u-c)} \delta p_e, \\ \delta W_2 &= \delta u + \frac{c}{A} \delta A + \frac{\phi}{\rho(u+c)} \delta K + \frac{K(\partial \phi / \partial A_o)}{\rho(u+c)} \delta A_o + \frac{1}{\rho(u+c)} \delta p_e, \end{aligned} \quad (12)$$

where the first two terms on the right-hand side are derived from the matrix form Equation (6); and the last three terms are the numerical parts.

The approach adopted to solve Equation (8) is the third-order TVD Runge-Kutta method for time integration:

$$\begin{aligned} Q^1 &= Q^n + \Delta t RHS(Q^n, t), \\ Q^2 &= \frac{3}{4} Q^n + \frac{1}{4} Q^1 + \frac{1}{4} \Delta t RHS(Q^1, t + \Delta t), \\ Q^{n+1} &= \frac{1}{3} Q^n + \frac{2}{3} Q^2 + \frac{2}{3} \Delta t RHS(Q^2, t + \frac{1}{2} \Delta t), \end{aligned} \quad (13)$$

where superscript ‘n’ represents the values at the previous time step; and ‘RHS’ represents the right-hand side terms of Equation (12).

### 3.1.3 Junctions in human vessel networks

The treatment of vessel junctions is the most significant part of the vessel network calculation, as shown in Figure 3.2. In the 1D model, the branching and merging points can be treated using the Riemann variables, conservation of mass, and the Bernoulli equations proposed in (Huang et al., 2015).

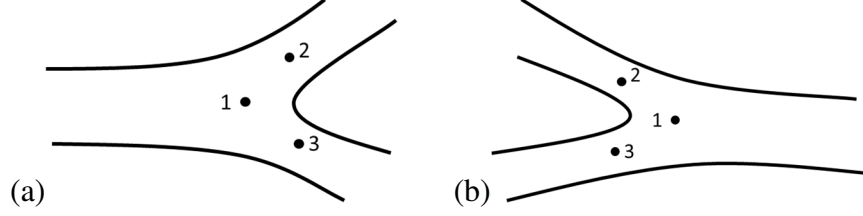


Figure 3.2 1D model vessel tree connection. (a) is branching point and (b) is the merging point. In the vessel junctions, a total of  $N$  number of vessels connecting, so that the boundary condition requirement for each vessel has two unknowns which are  $A_k^n$  and  $Q_k^n$  at time  $t^n$ , where the subscript  $k$  represent the  $k^{th}$  vessel and the superscript  $n$  denotes the unknown boundary values. Therefore, the total number of  $2N$  unknowns has to be solved. For example, the junction shown in Figure 3.2, the flow comes from parent vessel 1 and supplies blood to daughter branches 2 and 3, respectively. This simple bifurcation requires six unknowns:  $A$  and  $Q$  in each vessel, resulting in the requirement of six equations to calculate these unknowns. So the following assumptions have to be made: 1) the Riemann variables contributes each of vessel an equation by imposing that the characteristic variables in each vessel should remain constant, and equations can be written:

$$u_k^n + \mathfrak{I}_k \int_{A_{o,k}}^n \frac{c(A)}{A} dA = u_k^{n-1} + \mathfrak{I}_k \int_{A_{o,k}}^{n-1} \frac{c(A)}{A} dA \quad (14)$$

Where the superscript  $n-1$  is the point adjacent to the boundary point and the values of which can be obtained from the solution of the governing equation, (8); the value of  $\mathfrak{I}_k$  is either 1 or -1 based on which end of vessel:

$$\mathfrak{I}_k = \begin{cases} 1 & \text{if the distal end of the vessel} \\ -1 & \text{if the proximal end of the vessel} \end{cases} \quad (15)$$

Although the analytic solution of the integration shown in equation (14) is available for artery, for the sake of generality, the integration of equation (14) was used a 10-point

Gaussian quadrature. The other three equations can be obtained from the conservation of mass and the Bernoulli equation:

$$\sum_{k=1}^N \mathfrak{I}_k A_k^n u_k^n = 0 \quad (16)$$

$$P(A_1^n) + 0.5\rho(u_1^n)^2 = P(A_k^n) + 0.5\rho(u_k^n)^2 \text{ for } k = 2, \dots, N \quad (17)$$

In conclusion, the six equations given by (14-17) define a nonlinear system of algebraic equations which determine the unknowns at the bifurcation.

#### 3.1.4 0D models

In a human body, large arteries are directly connected to veins through one-by-one connections, whereas small arteries are merged to connect to coupling veins. Thus the distal/proximal ends of the arterial and venous system are connected via a 0D network composed of twenty one-artery-to-one-vein connections (mainly occurred in arms and legs) and seven complex circuit diagrams (mainly occurred in the brain and chest) (Müller et al., 2014). The governing equations of the network are obtained by imposing mass or momentum conservation in which resistors, inductors, and capacitors were employed to account for the viscous resistance to blood flow, blood inertia, and compliance of vascular wall, respectively, as sample connections shown in Figure 3.3, where the subscript *al* represented the electric components for arterials, *cp* represents the electric components for capillaries, and *vn* represents the electric components for venules. The governing equations of the network are obtained by imposing mass or momentum conservation on each node.

$$Q_i = \frac{P_i - P_{i+1}}{R_{i+1}}, \quad (18)$$

$$\frac{dP_i}{dt} = \frac{1}{C_i} (Q_{i-1} - Q_i) + \frac{dP_e}{dt}, \quad (19)$$

$$\frac{dQ_i}{dt} = \frac{1}{L_i}(P_i - Q_i R_i - P_{i+1}), \quad (20)$$

where,  $P_i$  and  $P_{i+1}$  represent the pressures upstream and downstream of the  $Q_i$  node, respectively. And  $Q_{i-1}$  and  $Q_i$  represent respectively the inflow and outflow rates of the  $P_i$  node. Thus, the RCRL lumped model was adopted from the previous work, and we refer readers to the detailed descriptions in the report by (Müller et al., 2014).

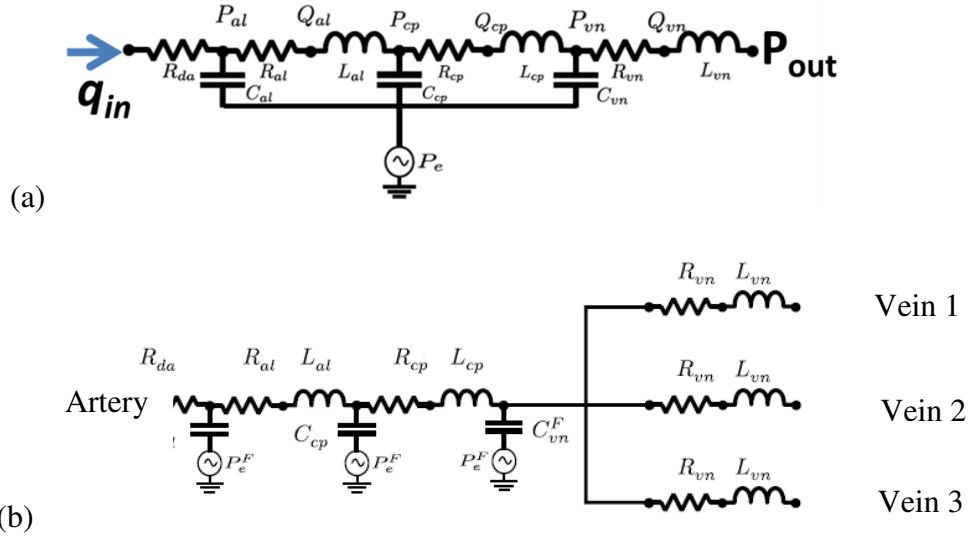


Figure 3.3 (a), a simple artery-to-vein lumped model. Left side is the feeding artery, and the right side is the collecting vein. (b), a complex lumped model. Parameters for resistances, inductors, and capacitors are given in (Huang et al., 2015 and Müller et al., 2014)

The heart chambers, corresponding valves, and pulmonary circulation were developed using 0D model. For the detailed connections of the 0D models, one can be referred to references (Huang et al., 2015 and Müller et al., 2014). The contraction and relaxation actions of the cardiac chambers were represented respectively by a time-varying elastance. Blood pressure ( $P_{ch}$ ) in a cardiac chamber is expressed by Huang et al., (2015) and Müller et al., (2014):

$$P_{ch}(t) = P_e + (E_A e(t) + E_B)(V_{ch} - V_{ch,0}) + S \frac{dV_{ch}}{dt} \quad (21)$$

where  $E_A$  and  $E_B$  are the active and passive elastance, respectively.  $V_{ch}$  and  $V_{ch,0}$  represent the chamber volume and dead chamber volume, respectively.  $e(t)$  is a normalized time-varying function, which for the atria and ventricle are described by:

$$e_a(t) = \begin{cases} 0.5\{1 + \cos[\pi(t + T - t_{ar})/T_{arp}]\}, & 0 \leq t \leq t_{ar} + T_{arp} - T \\ 0, & t_{ar} + T_{arp} - T < t \leq t_{ac} \\ 0.5\{1 - \cos[\pi(t - t_{ac})/T_{acp}]\}, & t_{ac} < t \leq t_{ac} + T_{acp} \\ 0.5\{1 + \cos[\pi(t - t_{ar})/T_{arp}]\}, & t_{ac} + T_{acp} < t \leq T \end{cases} \quad (22)$$

$$e_v(t) = \begin{cases} 0.5\{1 - \cos[\pi t/T_{vcp}]\}, & 0 \leq t \leq T_{vcp} \\ 0.5\{1 + \cos[\pi(t - T_{vcp})/T_{vrp}]\}, & T_{vcp} < t \leq T_{vcp} + T_{vrp} \\ 0, & T_{vcp} + T_{vrp} < t \leq T \end{cases} \quad (23)$$

where  $T$  represents the period of a cardiac cycle;  $T_{vcp}$ ,  $T_{acp}$ ,  $T_{vrp}$ , and  $T_{arp}$  represent the durations of ventricular/atrial, and contraction/relaxation, respectively; and  $t_{ac}$  and  $t_{ar}$  are the times within the cardiac cycle at the beginning of atrial contraction and relaxation, respectively.

The key to the solution of the complete human blood circulation model is to couple 0D models to the 1D vessel network. As the 0D models consist of the solution of a system of ordinary differential equations, the same third-order Runge–Kutta method, Equation (13), is applied to solve the system of ODEs. Once both the 1D solution and the 0D model solution are brought to the same time level, the coupling of the 0D model and the 1D vessel is updated. This coupling is performed at each step of the Runge–Kutta operations. It should be noted that the 0D-1D model will be called as 1D model in the rest of this dissertation.



### 3.2 *In vitro* experiments on the CoW

The experimental study aims to validate the 1D numerical model by comparing the numerical simulation results with the *in vitro* experimental data. A closed loop cerebrovascular circulation model was established, including a physical patient-specific model of the CoW. Transient pressure and flow rate waveforms were measured at eight selected locations within the network. The results will be mainly focusing on the comparisons of the flow rate and pressure waveforms at various locations between the 1D model and the experiment.

#### 3.2.1 Experimental setup

A vascular model of a complete CoW has been created from the 3D rotational angiography images as shown in Figure 3.4. 3D rotational angiography image databases of the CoW are available through a long-term collaboration with Miami Valley Hospital of Premier Health in Dayton, Ohio. The physical silicone model of the CoW with isotropic thickness was printed using a prototype machine at Medisim Corporation as presented in Figure 3.5. Size modifications were made at the inlets and outlets of the CoW model in order for connecting with standard Tygon tubes. As the flow network shown in Figure 3.5, a closed loop cerebrovascular circulation network was established with a pulsatile pump (Harvard Apparatus Pulsatile Blood Pump), an overflow reservoir, a silicone model of the complete CoW, and bifurcation connectors. The silicone model of CoW was created starting from left/right ICA and VA to the ending with six exits, which are left/right PCA, MCA, and ACA. Tygon tubes were used to connect the CoW model to the artificial heart and overflow reservoir served as transition sections to complete the network. Overall, the current cerebral artery network consists of fifty-nine branches.

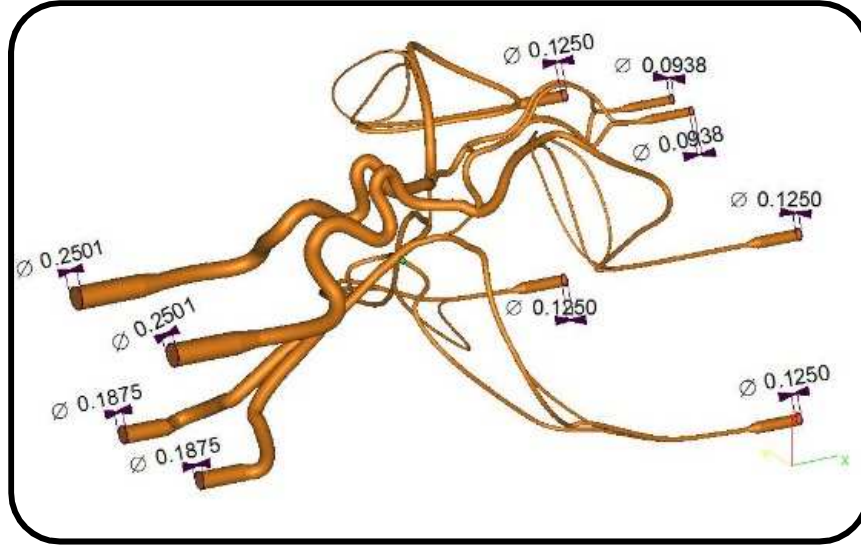


Figure 3.4 Reconstructed CoW model from 3D angiography.

The Harvard pump was set to output a periodic pulsatile flow wave with the mean flow rate of approximate 16 ml/s, which is falling into the range of the total flow rate entering into the CoW of human (Hendrikse et al. 2005). Flow control valves were installed at the terminals of the tubes to control the flow rates and back pressures at terminals. The working fluid was made by mixing water with glycerol at the ratio of 75/25 with the density of  $1050 \text{ kg/m}^3$  and viscosity of  $0.0026 \text{ Pa}\cdot\text{s}$  to mimic the properties of blood. The pulsatile pump was set with the following settings to generate the inflow conditions: 60 beats per minute with a systolic to diastolic ratio of 35/65. The resistor was directly connected to an overflow reservoir to generate a constant distal pressure.

The flow rate waveforms were measured using the ultrasonic flow meter (TS410 Tubing Flow module, transonic systems Inc. Ithaca, NY, USA) with a flow sensor (ME 6 PXN) of 0.9525 cm inner diameter. The pressure was measured simultaneously using the micro-tip catheter pressure transducers (SPR-524, Millar Instruments, Houston, TX, USA). The transient flow rate and pressure measurements were collected at eight selected locations, including the main artery, LCCA, LSA, LICA-I, LVA-I, LACA-VI, LMCA-VII, and

LPCA-VI, of the flow network due to the symmetric configuration of the model. It should be noted that the measurements of flow rate and pressure waveforms couldn't be achieved inside the silicone CoW model because the pressure catheter and flow sensor couldn't be inserted through the arteries in the CoW due to the small and tortuous tubes.

Table 3.1 Parameters of the Tygon and silicone tubes presented in Figure 3.5.

No.	Vessel name	Length (cm) $\pm 3\%$	$r_{in}$ (cm) $\pm 5\%$	$r_{out}$ (cm) $\pm 5\%$	$h$ (cm) $\pm 2\%$
1	Main a.	20.000	0.318	0.318	0.165
2	Common carotid a.	26.000	0.318	0.318	0.165
3	Subclavian a.	27.000	0.318	0.318	0.165
4	L. int. carotid a. I	25.000	0.318	0.225	0.165
5	R. int. carotid a. I	25.000	0.318	0.225	0.165
6	L. Vertebral a. I	27.000	0.318	0.318	0.165
7	R. Vertebral a. I	26.000	0.318	0.318	0.165
8	Basilar a.	3.500	0.162	0.137	0.150
9	R. int. carotid a. II	11.500	0.225	0.155	0.150
10	L. int. carotid a. II	11.500	0.225	0.155	0.150
11	R. Vertebral a. II	4.600	0.217	0.217	0.150
12	L. Vertebral a. II	4.600	0.217	0.217	0.150
13	R. ant. cerebral a. I	1.500	0.070	0.070	0.150
14	L. ant. cerebral a. I	1.500	0.070	0.070	0.150
15	R. ant. cerebral a. II	1.600	0.065	0.065	0.150
16	L. ant. cerebral a. II	1.600	0.065	0.065	0.150
17	R. ant. cerebral a. III	2.750	0.060	0.060	0.150
18	L. ant. cerebral a. III	2.750	0.060	0.060	0.150
19	R. ant. cerebral a. IV	3.000	0.060	0.060	0.150
20	L. ant. cerebral a. IV	3.000	0.060	0.060	0.150
21	R. ant. cerebral a. V	2.500	0.065	0.115	0.150
22	L. ant. cerebral a. V	2.500	0.065	0.115	0.150
23	R. post. communicating a.	0.960	0.050	0.050	0.150
24	L. post. communicating a.	0.960	0.050	0.050	0.150
25	R. post. cerebral a. I	0.980	0.075	0.075	0.150
26	L. post. cerebral a. I	0.980	0.075	0.075	0.150
27	R. post. cerebral a. II	4.400	0.070	0.070	0.150
28	L. post. cerebral a. II	4.400	0.070	0.070	0.150
29	R. post. cerebral a. III	6.200	0.070	0.070	0.150
30	L. post. cerebral a. III	6.200	0.070	0.070	0.150

Table 3.1 continued from previous page.

No.	Vessel name	Length (cm) $\pm 3\%$	$r_{in}$ (cm) $\pm 5\%$	$r_{out}$ (cm) $\pm 5\%$	$h$ (cm) $\pm 2\%$
31	R. post. cerebral a. IV	6.000	0.070	0.070	0.150
32	L. post. cerebral a. IV	6.000	0.065	0.070	0.150
33	R. post. cerebral a. V	2.200	0.085	0.150	0.150
34	L. post. cerebral a. V	2.200	0.085	0.150	0.150
35	R. middle cerebral a. I	3.000	0.145	0.145	0.150
36	L. middle cerebral a. I	3.000	0.145	0.145	0.150
37	R. middle cerebral a. II	8.200	0.050	0.050	0.150
38	L. middle cerebral a. II	8.200	0.050	0.050	0.150
39	R. middle cerebral a. III	4.300	0.040	0.040	0.150
40	L. middle cerebral a. III	4.300	0.040	0.040	0.150
41	R. middle cerebral a. IV	3.200	0.040	0.040	0.150
42	L. middle cerebral a. IV	3.200	0.040	0.040	0.150
43	R. middle cerebral a. V	4.400	0.045	0.045	0.150
44	L. middle cerebral a. V	4.400	0.045	0.045	0.150
45	R. middle cerebral a. VI	4.300	0.065	0.150	0.150
46	L. middle cerebral a. VI	4.300	0.065	0.150	0.150
47	Ant. communicating a.	0.100	0.050	0.050	0.150
48	R. post. cerebral a. VI	67.000	0.318	0.318	0.165
49	L. post. cerebral a. VI	66.000	0.318	0.318	0.165
50	R. ant. cerebral a. VI	28.000	0.318	0.318	0.165
51	L. ant. cerebral a. VI	24.000	0.318	0.318	0.165
52	R. middle cerebral a. VII	75.000	0.318	0.318	0.165
53	L. middle cerebral a. VII	67.000	0.318	0.318	0.165
54	Ant. Cerebral a. VII	8.000	0.318	0.318	0.165
55	Middle cerebral a. VIII	8.000	0.318	0.318	0.165
56	Post. cerebral a. VII	8.000	0.318	0.318	0.165
57	Ant. Cerebral a. VIII	78.500	0.215	0.215	0.130
58	Middle cerebral a. IX	83.000	0.215	0.215	0.130
59	Post. cerebral a. VIII	61.000	0.215	0.215	0.130

The flow meter and pressure transducer were calibrated through volumetric flow measurements and hydraulic pressure measurements, as shown in Figure 3.6 (a) and (b). During the experiment, the pressure data and flow rate data were sampled at 1000 Hz and collected through the software LabVIEW with a written program to convert the voltage reading to flow rate (ml/s) and pressure (Pascal), respectively, as presented in Figure 3.7.

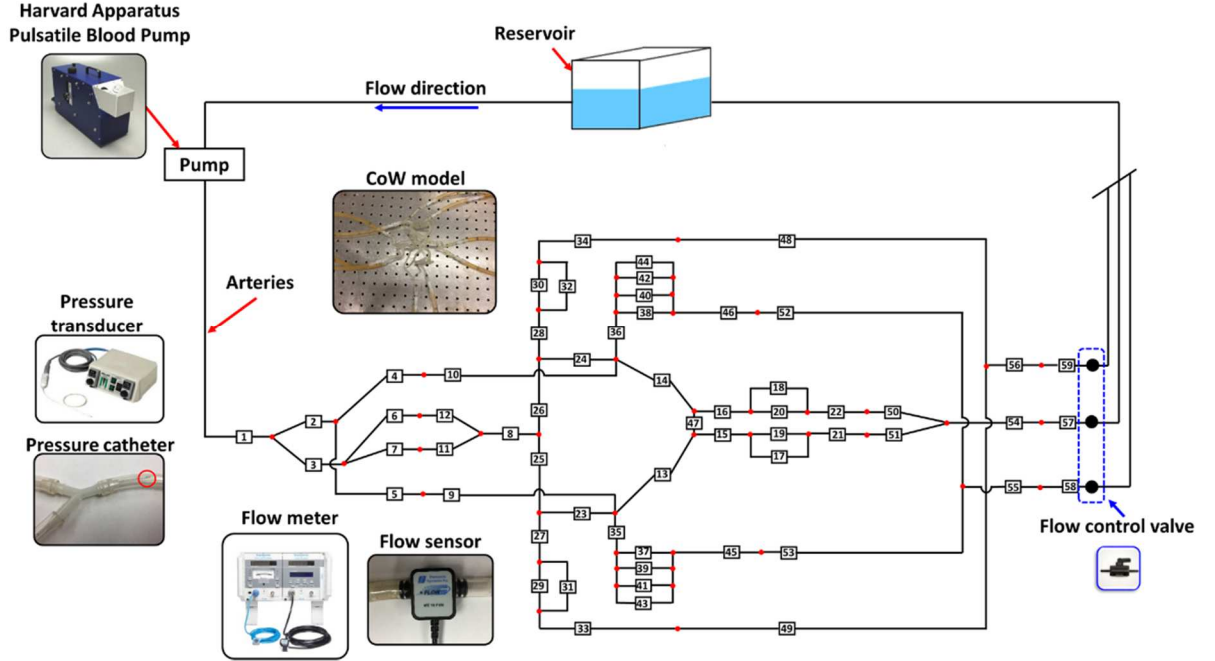


Figure 3.5 Schematic drawing of the experimental setup.

In the 1D model, the terminal analogy resistance was computed by using lumped parameter models (0D), which adopts a single  $R$  electrical analog model. The governing equation of the 0D model can be written as:  $Q_{1D} = (P_{1D} - P_{out})/R_T$ , where  $Q_{1D}$  and  $P_{1D}$  are the flow rate and pressure at the outlets of the 1D model, herein,  $P_{out}$  is the constant hydraulic pressure generated by the reservoir with a of zero pa as the reference pressure by calibrating the pressure transducer.  $R_T$  is the total peripheral resistance at the end of the 1D model, and the values are presented in Table 3.2. The terminal resistances were examined from the mean pressure and flow rate measured at the inlets and exits of the flow control valves.

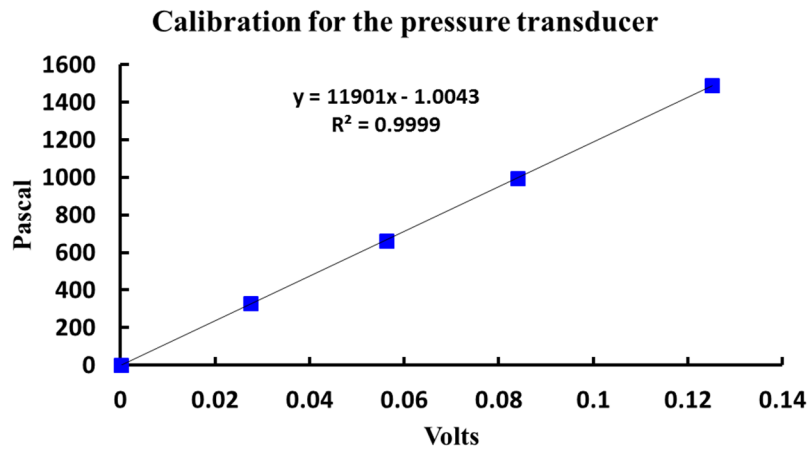
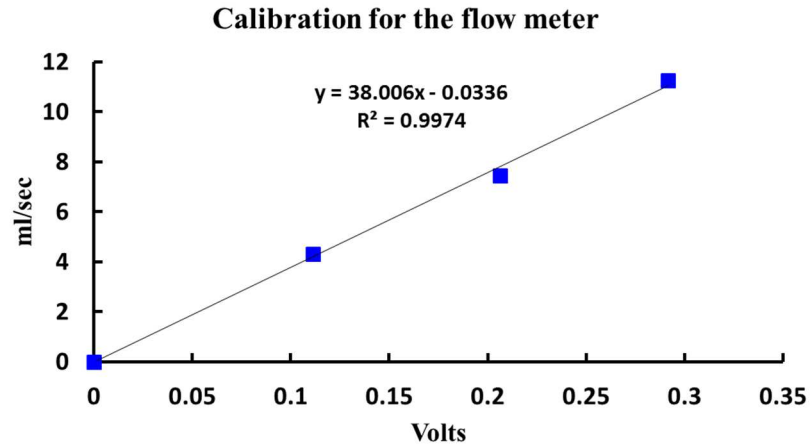
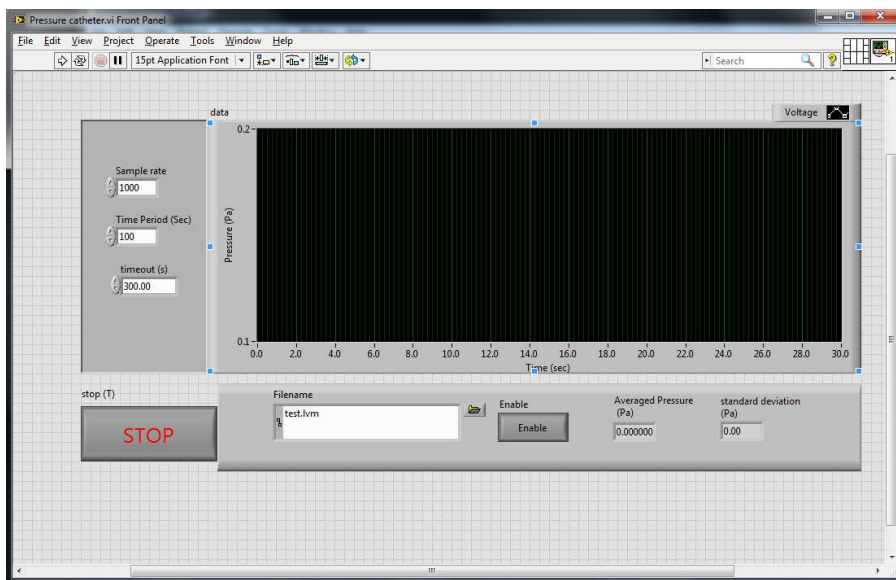


Figure 3.6 Calibration curves for the Transonic TS410 flow meter (top) and the Millar Instruments SPR-524 pressure transducer



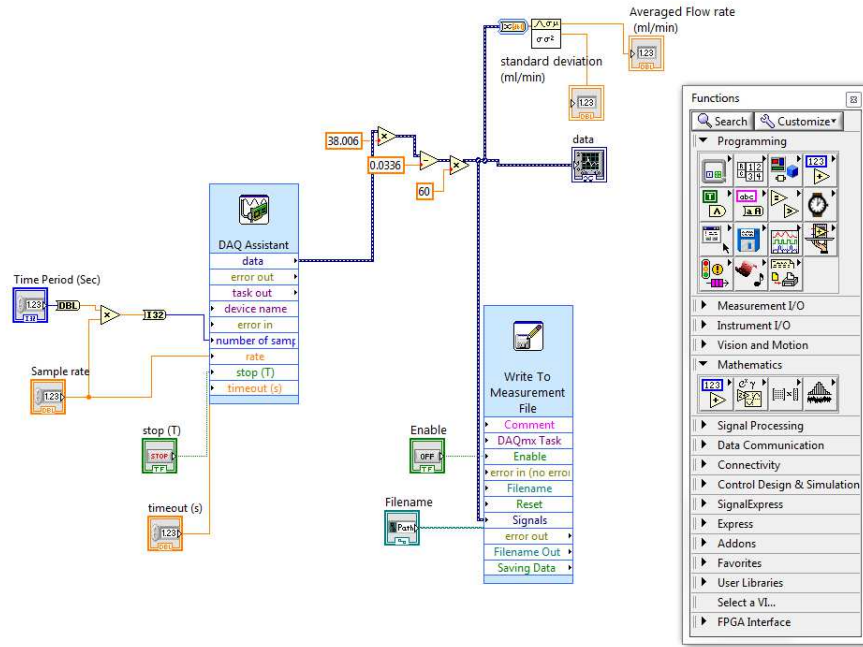


Figure 3.7 The main screen of the LabVIEW (Top) and the program to convert the voltage reading to pascal.

Table 3.2 Peripheral resistance.

Arteries	Terminal resistance ( $10^7 Pa s m^{-3}$ )
Ant. cerebral a. VIII	5.06
Middle cerebral a. IX	5.00
Post. cerebral a. VIII	4.91

The simulation parameters used in the 1D model was directly measured from the experimental models, such as the length, radius, and thickness of vessels, as shown in Table 3.1. Inflow conditions were specified with the flow rate waveform measured from the exits of the pulsatile pump. The Young's modulus of the Tygon and the silicone tubing are 6.7 and 0.357 MPa, respectively, obtained from the model's manufacturers.

### 3.3 Simulation of the vascular aging

The 1D model has been improved to account for the vascular aging effects, and the parameters used to describe the aging, such as the PWV, radius of arteries, and

mechanical properties were adopted from previous statistical works. For the NVA system, the PWV of the elastic arteries and the peripheral arteries in the arterial system matched the data reported by Huang et al., (2015), Liang et al., (2009), and McEniery et al., (2005). Furthermore, the increasing ratio of the radius of the peripheral elastic arteries to the cerebral arteries was adjusted to agree with the data reported by McEniery et al., (2005) and Bullitt et al., (2010). For veins, due to the lower pulse wave velocity and flow rate in the venous system, changes of the properties of the venous vessels are not apparent. Thus, the SVC and IVC were applied in 3% and 2.5% linear increment on the radius and PWV (Nippa, et al., 1971). Since arteries are stiffer in the EVA system than those in the NVA system (Nilsson, 2015), mechanical parameters in the EVA system were adjusted so that the PWVs matched the results reported in previous studies (Cunha et al., 2015 and Redfield et al., 2014). Additionally, the changes of total resistance with age were adopted from Liang et al., (2009) for both systems. In addition, parameters of the active and passive elastance of the Left Ventricle (LV) were adopted from literature (Liang et al., 2009 and Redfield et al., 2005). Table 3.1 displays the PWV, aortic radius, and the elastance of left ventricle changes in ascending aorta (Yu et al., 2016). The investigation of the effects of the vascular aging on the hemodynamics in cardio- and cerebrovascular systems will be presented in Chapter 5.



Table 3.3 Parameter changes in the aortic pulse wave velocity (Co), ascending aorta radius (R) and left ventricle peak systolic elastance during aging.

	25 yr	35 yr	45 yr	55 yr	65 yr	75 yr	85 yr
NVA Aortic Co ( $\text{m s}^{-1}$ )	5.11	5.50	6.06	6.81	7.73	8.43	9.20
NVA Aortic R (cm)	1.47	1.59	1.71	1.83	1.95	2.07	2.19
EVA Aortic Co ( $\text{m s}^{-1}$ )	6.13	7.15	8.18	9.20	10.22	11.24	12.26
EVA Aortic R (cm)	1.69	1.81	1.93	2.05	2.17	2.30	2.41
LV Elastance ( $\text{mmHg ml}^{-1}$ )	2.20	2.37	2.53	2.70	2.86	3.02	3.19

### 3.4 3D simulation of cerebral aneurysms

#### 3.4.1 The reconstruction of aneurysm models

3D DSA imaging data (Siemens Artis Zee) was obtained from an un-ruptured ICA aneurysm scanned in a 64-year-old, Caucasian, female patient with no smoking history or family history of RIAs. All 3D imaging data were acquired using the Siemens 3D spin software. Images were collected by careful catheterization of the cervical ICA using a 5F Terumo angle taper catheter and then visipaque 300 contrast agent was injected using the powered injector set at 3 ml/min contrast for 18 ml, total over a 6 second spin with a variable rate rise dependent on the patient's cardiac output and previous DSA contrast runs. This axial sliced data was then collected in the DICOM format and identified by the operating physician. In this work, 500 segmented files with the thickness of 0.4 mm were used to reconstruct the 3D patient-specific morphology. The transformation from DICOM format to STL file was performed using a freeware software, 3D-Slicer. The STL file is considered a generic format for both CFD and CAD software.

Figure 3.8 (a) shows the unmodified 3D vascular reconstruction. As can be seen, not only does the data contain ample image noise, but there exist many trivial branches associated with various blood vessels. In order to reduce the computational efforts, the core region

of the aneurysm was concentrated. The modification involves smoothing out the image noise appearing on the vessel surfaces and connections, filling holes, repairing broken connections, and eliminating unwanted small branches (unless they were approaching the ostium or connecting to the aneurysmal sac directly). These modifications were performed in a commercial CFD software Cradle SC/Tetra V12. The final configuration of the morphology is shown in Figure 3.8 (b). The ICA aneurysm was classified by two, independent, neuro-interventionalist as a side-wall, saccular, unruptured aneurysm exhibiting with one lobe. The diameter of the ICA inlet was 5.03 mm, the vertical height from the ostium to the aneurysm dome is 3.32 mm and the diameter of the aneurysm ostium is 3.72 mm which was comparable to CT angiography measurements. The equivalent diameter of the aneurysm sac is 4.42 mm computed based on the volume of the aneurysmal sac measured as 45.19 mm<sup>3</sup>.

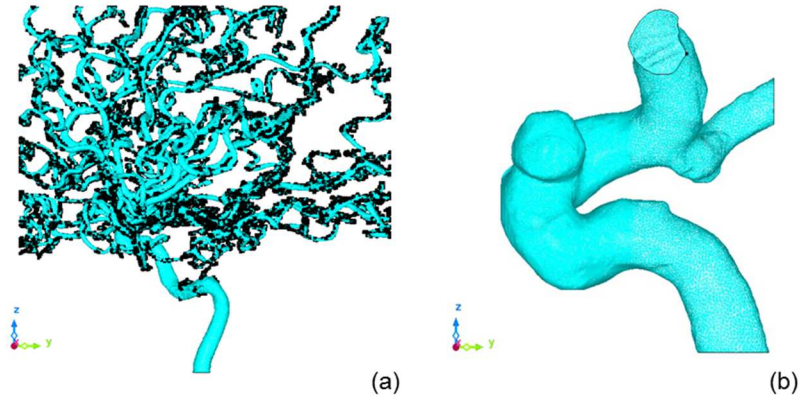


Figure 3.8 a. Initial 3-D model; b. Vessel geometry after deformable modeling and removing arterial branches

### 3.5 Hemodynamic parameters

In this dissertation, qualitative and quantitative comparisons in the present work focus on the pressure, WSS, OSI, RMSWSS, and 3D streamlines. The WSS represents the

tangential frictional stress between the blood flow and endothelium wall of blood vessel.

For unsteady flow time-averaged WSS was computed by the following equation:

$$WSS = \frac{1}{T} \int_0^T |\overrightarrow{WSS}| dt \quad (24)$$

where  $|WSS_i|$  is the instantaneous WSS (N/m<sup>2</sup>) magnitude and T denoted the pulse period.

The OSI evaluates the differences between time-averaged WSS magnitude and the magnitude of time-averaged WSS vector. So, the WSS vector deflection from blood flow predominant direction can be defined.

$$OSI = 0.5 \left( 1 - \left| \int_0^T \overrightarrow{WSS} dt \right| / \int_0^T |\overrightarrow{WSS}| dt \right), \quad (25)$$

where  $1/T \left| \int_0^T \overrightarrow{WSS} dt \right|$  denotes the magnitude of time-averaged WSS vector,  $1/T \int_0^T |\overrightarrow{WSS}| dt$  denotes the time-averaged WSS magnitude, and  $T$  denotes the duration of the cycle. Blood flow turnover time was defined as the volume of the aneurysm sac divided by the inflow rate. It is associated with blood clotting and thrombotic occlusion of the aneurysm (Xiang et al., 2015).

The variances of pressure and WSS provide information for the strength of the oscillation and are defined as  $\sqrt{p'^2}$  and  $\sqrt{\tau_w'^2}$ , where prime denotes the difference between instantaneous and mean values and bar indicate an average over the one-time cycle.

### 3.6 1D-3D multi-scale modeling

The CFD solver package Cradle SC/Tetra was used to compute the flow physics of 3D segments. The blood flow was solved as an incompressible and Newtonian flow with a density of  $\rho = 1050 \text{ kg/m}^3$  and a dynamic viscosity of  $\mu = 3.5 \times 10^{-3} \text{ Pa} \cdot \text{s}$ . The evaluation of the Newtonian and Non-Newtonian fluid is tested at Section 6.3 in Chapter 6. The shear rate distribution over and the aneurysm surface indicated that the assumption

of Newtonian fluid is acceptable for the current aneurysm model because only a small region is under a low shear rate less than 100/s. Conservation of mass and momentum equations constitute governing equations to solve the flow velocity and pressure distribution. Rigid wall boundary condition was assumed for the 3D model calculation for the sake of saving computational efforts, and the non-slip wall condition was applied. It should be noted that the inlet of the artery was extended by twenty times diameter to ensure the generation of Womersley velocity profiles flowing through the aneurysm as reported by Pereira et al., (2013). In all the multi-scale simulations, the maximum Reynolds number is 435 as appeared in the straight stenotic pipe case, a detailed description of the simulation is given in Chapter 7. All simulations assume the flow as laminar flow throughout the calculation, even though transition flow could occur due to the stenosis and aneurysm. The assumption of laminar flow is adopted for the sake of simplicity although the proposed method can also be applied in cases where transition and/or turbulence exist.

The multi-scale model was developed by linking the 1D and 3D models to complete the entire blood circulation system. The spatial pressure gradient and flow rate waveforms between the 1D and 3D models are exchanged as described in Figure 3.9. The treatment of the interfaces for the current method is conducted in a cardiac-cycle-based fashion: the pressure gradients from the 3D model during the cycle was stored and then mapped onto the corresponding locations in the 1D model within one cardiac cycle; and similarly, the mass flow rate obtained from the 1D model was stored and mapped onto the 3D model as inlet boundary condition in a cycle to cycle manner (Liang et al., 2015).

For example, for a 3D segment with  $N$  multiple exits, the  $N-1$  boundary conditions of the flow rate waveforms of the 3D simulation were extracted from the corresponding arteries in the 1D simulation and the zero static pressure is specified at the  $N^{th}$  vessel. This will ensure the consistency of the mass flow rates between the 1D and 3D simulations. When the 3D simulation is accomplished, the spatial-averaged pressure gradients  $dP_N^{3D}/ds$  for the local 3D morphology of each vessel can be computed, where  $N$  represents the segment of the vessel network and  $s$  is the streamwise distance. The pressure gradients were then mapped onto the corresponding locations of the 1D model as the new pressure resistance to account for the 3D morphological effects. The iterations between 1D and 3D models was conducted in a cycle-to-cycle manner until the solutions converge. A convergence tolerance was defined to allow the maximum relative error of the  $P_N^{3D}$  to be less than 0.01,  $\varepsilon_{P_{N,3D}}^{MAX} = \max_i |(P_{i,3D} - P_{i,1D})/P_{i,3D}|$  (Boileau et al., 2015). The validation and application studies will be presented in Chapter 7.

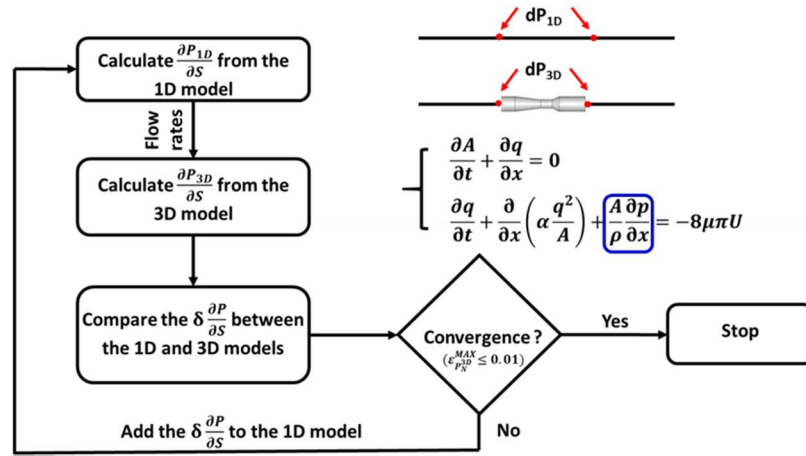


Figure 3.9, the multi-scale method flowchart of a test case containing three arteries and coupling with a 3D artery model.

## 4 THE VARIATIONS OF THE COW

### 4.1 Overview

Previous studies reported that approximately 60% of the population does not have a complete Circle of Willis (CoW) (Lasheras, 2007). A number of investigations proposed to link the variations of CoW to the formation and risk of rupture of cerebral aneurysms (Berg et al., 2014; Cebal and Raschi, 2013; de Rooij et al., 2009; Kayembe et al., 1984; Krasny et al., 2014; Lazzaro et al., 2012; Songsaeng et al., 2010). Although there is evidence that cerebral aneurysms are associated with CoW anomalies, the risk factors associated with rupture are not determined, and most studies were inconclusive. Many investigations focused strictly on the statistical correlation between the anatomic variations and locations of aneurysms. However, there was not a study that investigated the impact of the blood flow redistribution caused by the variations in CoW. We hypothesize that variations of the CoW may result in distinct flow patterns and thus their impact on various regions in the CoW might be considerable. Recent evidence has shown that the flow pattern in the CoW may be affected dramatically as a result of the collateral function to shunt the blood flow and that these effects may be highly asymmetric (Krasny et al., 2014; Lee et al., 2004; Liang et al., 2011). Blood flow can also be distributed asymmetrically in the CoW of patients who have anatomical variants. For example, a missing right anterior cerebral artery (A1) segment may cause the flow rate in the left side of CoW to increase while the flow rate in the right side is reduced by the same amount. The AcoA is then subjected to a more massive load in shunting the imbalanced blood flow from the left A1 to the right A2. The resultant increase in pressure and WSS

from redistribution of the blood flow induces risk for various vascular malformations (Ujiie et al., 1996; Kasuya et al., 1999).

Current in vivo experiments using TCD ultrasonography, PC-MRI and video densitometry from X-ray images can provide useful measurements of flow rates in vessels. However, it should be noted that there are a number of limitations in experiments, such as limited spatial and temporal resolution, disturbance effect from injection of contrast, etc. In vitro experiments of the three CoW variations with abnormal junctions were also conducted (Fahy et al., 2014; Fahy et al., 2014), but unfortunately, these experiments failed to account for flow rate changes of inflow conditions owing to the CoW variations.

The investigation of the hemodynamic characteristics of CoW has also been conducted by using the 3D CFD simulation. Patient-specific CoW models were successfully reconstructed based on MRA or CT images in previous reports (Reorowicz et al., 2014; Moore et al., 2006; Long et al., 2008). It is well known that the simulated results are significantly sensitive to the boundary conditions for 3D simulations, resulting in over- or under-estimating the hemodynamic behaviors. Reorowicz et al. (2014) reconstructed CoW models started from the ascending aorta to the terminals of the CoW. To minimize the flow and pressure uncertainties, Reorowicz et al. (2014) specified an inflow velocity profile as the inflow boundary condition in the aorta instead of applying in the feeding arteries of the CoW and coupled with a compliant artery extruded from the aorta. On the other hand, Moore et al. (2006) have taken the terminal resistance and the autoregulation effect of the CoW into consideration in the 3D simulation by defining a porous block at terminations and a relationship between the blood flow rate and arterial pressure. Both

simulated results could match the ultrasonography measurements and experimental data. The flow alterations could be captured due to a local pathological pressure drop by the latter method.

In this chapter, the THINKS model is provided to investigate the changes in flow patterns caused by the variational CoW. The intent is to use THINKS to recognize the alteration of flow patterns caused by the variation in the CoW with the ultimate goal of identifying the role of corresponding variations of WSS involved in the development of cerebral aneurysms.

## 4.2 Validation of the 1D model

The assessment of the accuracy of the 1D numerical model will be discussed in this section. The first test case adopted to validate the 1D model was chosen the in vitro experiment of the human arterial system performed in previous reports by (Alastruey et al., 2011; Matthys et al., 2007). The model contained thirty-seven rubber tubes containing major human arteries, with a pump used to mimic the heart to produce pulsatile flow condition. The inflow waveform and the terminal resistance of the vessel network are documented in the experiments. In their study, a value of 22 was used in the source term  $f$  in the viscous force of Equation (1b) in order to fit the experimental data, and the viscosity was taken as  $0.0025 \text{ Pa} \cdot \text{s}$ . Full details on the topography of the network, description of mechanical properties, the geometry of the vessels, terminal resistances, and the measurements of flow rates in different locations, are reported in the original paper (Matthys et al., 2007).

Figures 4.1 shows the flow rate and blood pressure waveforms computed by the 1D model and the numerical results reported in the previous work (Alastruey et al., 2011).



The current mesh for the vessel network is established by using  $\Delta x = 1$  mm and a CFL value of 0.9. The pressure and flow rates waveforms are presented at the midpoint of three selected arteries. As can be seen in Figure 4.1, the 1D model exhibits an excellent agreement with the reported numerical data. It demonstrates that the proposed 1D model can be employed to handle the one-to-one network connection with variable properties.

The second validation case considered to evaluate the 1D model was a reduced version of the anatomically detailed arterial network model developed by Blanco et al., (2015). The model consists of 56 major arteries, as presented in the report (Boileau et al., 2015). The inflow boundary condition  $Q_{in}(t)$  is obtained from one of the inflow signals reported by Murgo et al., 1980. Figure 4.2 presents the comparisons of the pressure and flow rate waveforms of the 1D model with the numerical results from the work by Blanco et al., (2015). A good agreement can be observed in the flow and pressure waveforms comparisons between the DCG numerical method and 1D model in the abdominal aorta, aortic arch, and thoracic aorta, respectively.

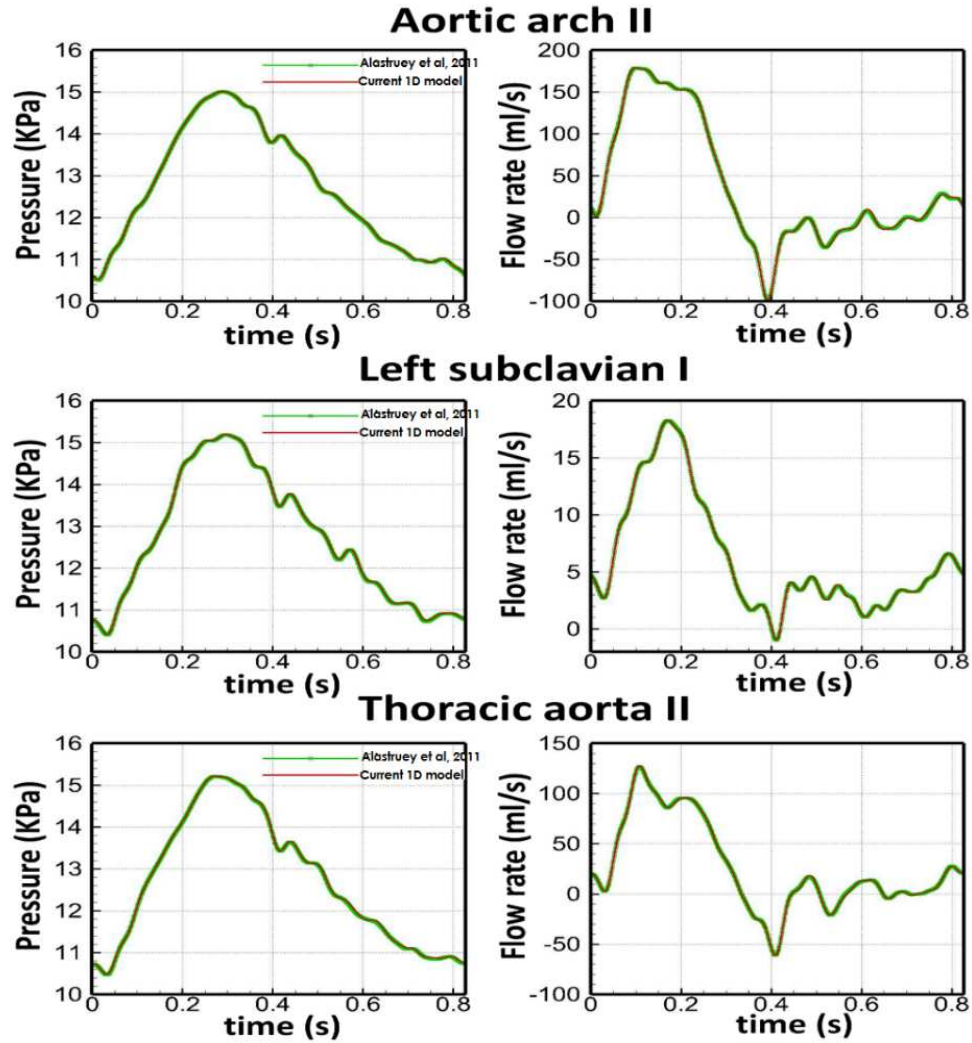


Figure 4.1 Comparison of waveforms from thirty-seven-artery-network model by Alastruey et al., (2011) with the waveforms of THINKS model. The top is the pressure and flow rate waveforms in the aortic arch II; the middle is the pressure and flow rate waveforms in the left subclavian I; the bottom is the pressure and flow rate waveforms in the thoracic aorta II.

The validation of simulation of the entire human vessel network was made by comparing the simulated results with previous *in vivo* measurement data (Gwilliam et al., 2009). As shown in Figure 4.3 (a) and (b), the flow rate prediction in CCA at a position which is 3 cm proximal to the bifurcation; (c) and (d) present results in ICA which is 3 cm distal to the bifurcation. The *in vivo* experimental data were obtained from twenty-two subjects (recruitment age: 20 to 40 years with no history of vascular disease) (Gwilliam et al.,

2009). The number of data sets obtained for (a) and (b) is  $N = 21$  (11 on the right, 10 on the left). The number of data sets obtained for (c) and (d) is  $N = 40$  (20 on the right, 20 on the left).

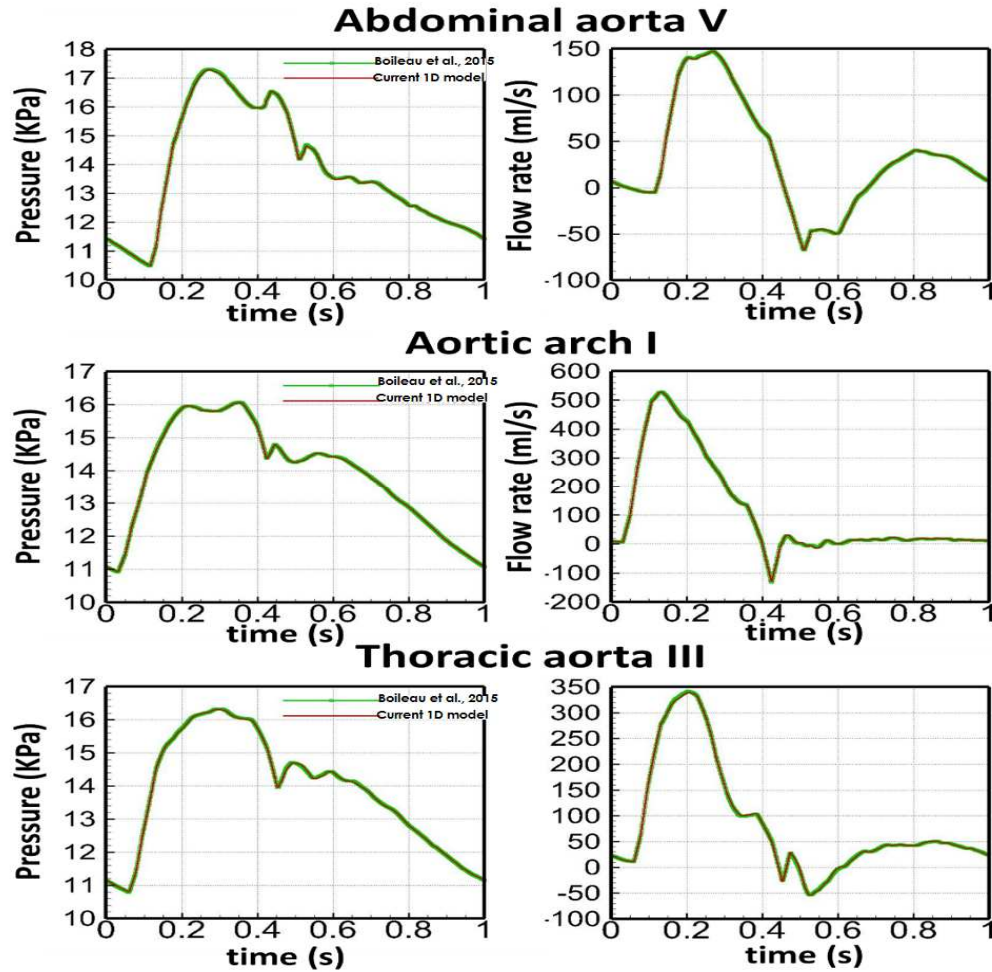


Figure 4.2 Comparison of Fifty-six-network model with 1D model. The top is the pressure and flow rate waveforms in the abdominal aorta V; the middle is the pressure and flow rate waveforms in the aortic arch I; the bottom is the pressure and flow rate waveforms in the thoracic aorta III.

As the waveform varied significantly from person to person, and from cycle to cycle, local minima and peaks and time between these were identified. Then the in vivo experimental data was aligned to the respective time of mid-acceleration in the time domain, and normalized by the cycle-averaged volumetric flow rate (Nilsson, 2015).

Therefore, the root mean square of the timing and amplitude was calculated and represented as the horizontal error bar and vertical error bar, respectively, as shown in Figure 4.3. The average S.D. of the raw flow rate waveforms is 23% of the mean value. This S.D. is reduced to 9% when the data is aligned temporally and normalized by the cycle-averaged volumetric flow rate (Gwilliam et al., 2009). The comparison implies that the aligned and normalized waveform is similar across all subjects. Overall, the prediction could capture the waveform within bounds of both the raw and normalized experimental data.

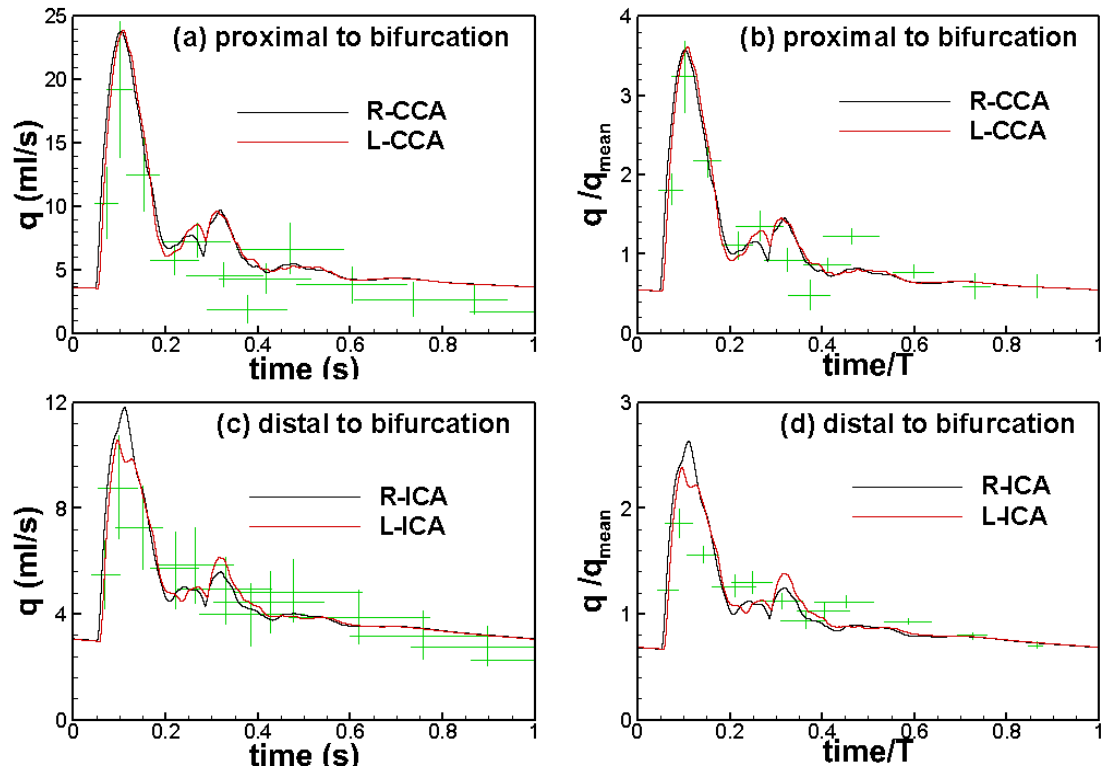


Figure 4.3 Simulated waveforms compared with the raw and normalized in vivo experimental data by Gwilliam et al., (2009): in common carotid artery proximal to bifurcation and internal carotid artery distal to the bifurcation. “+” represents the experimental data with error bar representing the confidence interval of the flow rate (vertical bar) and temporal response (horizontal bar). Black and red lines represent simulation data.

Figure 4.4 shows comparisons of flow rate waveforms in three different locations: ICA proximal to the carotid siphon (N = 24 with 12 each side), ICA proximal to CoW (N = 36

with 18 on each side) and in the mid-section of the basilar artery (BA) ( $N = 15$ ). It was observed that the in vivo experiments were very scattering due to the variation in individual waveforms. In the current modeling, only published averaged modeling parameters (i.e., length, diameter, the stiffness of the vessel wall, heart parameters, etc.) were used to simulate the cardiovascular circulation. The comparison is reasonably good except for the peak value of waveforms in the normalized comparison. In the normalized comparison, the current models tend to overpredict the flow rate near the peak by about 10%~30%. On the one hand, the analogy of blood flow to the electrical circuits simplifies the nonlinear characteristics of pressure and volume in a real artery, resulting in uncertainties in the flow and pressure waveforms. Individual variations are inherently smoothed out by using the population-averaged parameters. Therefore, some modeling parameters might not be accurate enough to represent the individuals involved in the in vivo experiment. The proposed method can be simply adjusted to match with the patient-specific waveforms by comparing the simulated results with the cuff measured pressure waveforms from different locations of a patient. On the other hand, it should be noted that the experimental measurements of peak values contain more uncertainties mainly owing to the poor temporal resolution and variation of waveforms involved in the experiments. Therefore the averaged experimental results tend to smooth out the peak and thus underestimate the flow rate near the peak. The structure of the CoW has a number of variations, such as missing A1, missing P1, and missing AcoA.

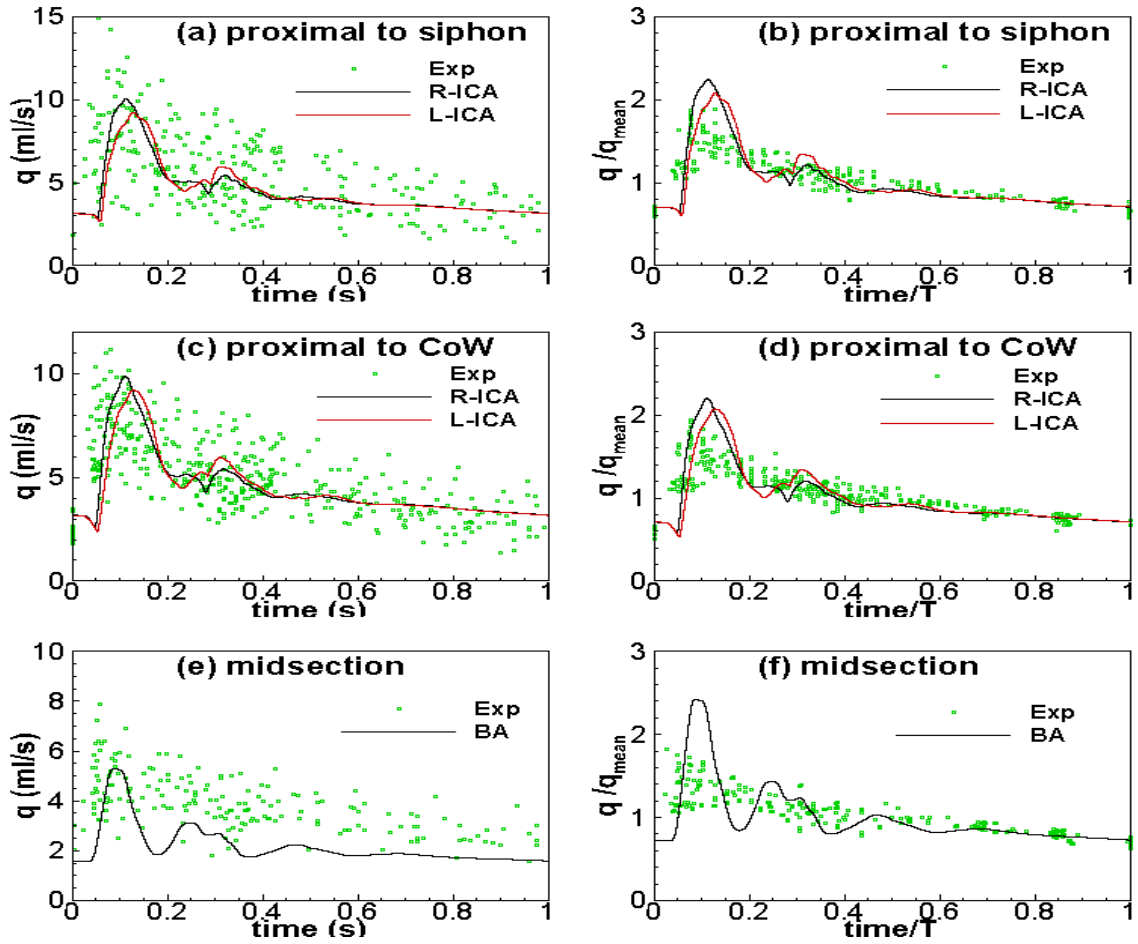


Figure 4.4 Absolute and dimensionless waveform comparison with in vivo experimental data: in internal carotid artery proximal to siphon, in internal carotid artery proximal to CoW, and in the midsection of the basilar artery (Tanaka et al., 2006).

### 4.3 Flow characteristics of a complete CoW

Figure 4.5 (a) shows the blood flow distribution for a complete CoW. The blood is supplied to the CoW through two ICAs and the BA. The predicted flow rate in each of ICAs is approximately  $270 \text{ ml min}^{-1}$  which falls in the value ranges of  $245 \pm 65 \text{ ml min}^{-1}$  and  $305 \pm 74 \text{ ml min}^{-1}$  (Tanaka et al., 2006; Hendrikse et al., 2005). The predicted BA flow rate is  $131 \text{ ml min}^{-1}$  and again falls in the range of  $118 \pm 37 \text{ ml min}^{-1}$  and  $165 \pm 43 \text{ ml min}^{-1}$  (Tanaka et al., 2006; Hendrikse et al., 2005). Although there is a slight difference regarding average flow rates, the ratios of flow rate for ICA and BA are

essentially the same with the value of 80:20 (Tanaka et al., 2006; Hendrikse et al., 2005), as described in Figure 4.5 (b). The predicted total flow rate into and out of the CoW is  $666 \text{ ml min}^{-1}$ , and the flow rate division among P2's, MCA's and A2's is 0.96: 2.01: 1.00, as shown in Figure 4.5 (b). The flow rate ratios of the ICAs and BA are in agreement with in vivo data. The flow distribution is almost symmetrical for a human with a complete CoW, whereas there is a small net flow rate of  $1.15 \text{ ml min}^{-1}$  from right to left in the AcoA. This implies that the cerebrovasculature on the right side has a slightly higher pressure than the left-hand side.

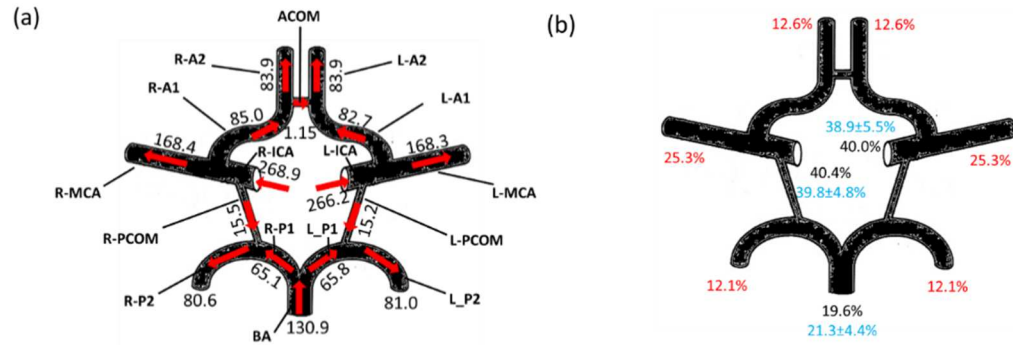


Figure 4.5 Flow rate distribution of a subject with a complete CoW. (a) Flow rate in  $\text{ml min}^{-1}$ . The flow directions are given by the arrow signs; (b) Percentage of total flow rate, percentage number in black is for afferent vessels, blue is for afferent vessels with experimental data (Tanaka et al., 2006), and red is for efferent vessels.

#### 4.4 Flow characteristics in variational circle of Willis

The CoW has been reported to exhibit many types of anatomical variations. The current study focuses on the comparison of the “complete” CoW with seven types of variations referred to Figure 4.5 (a): (a) missing A1 artery, (b) missing P1 artery, (c) missing one PcoA artery, (d) missing AcoA artery, (e) missing both PcoA arteries, and (f) missing P1-PcoA arteries, as shown in Figure 4.6. Table 4.1 shows the comparison of flow rate from different CoW anomalies with the complete CoW. The Table also illustrates blood supply ratios to different areas of the brain via P2's, MCA's and A2's.

Figure 4.6 provides a map of flow ratios in all afferent and efferent vessels of the CoW for variations (a) through (f). Although the flow rates of the efferent arteries are almost unchanged, the flow rates of the afferent arteries can vary substantially due to variations of CoW. For example, for the missing-A1 case (Figure 4.6 (a), Table 4.2), the flow rate in the R-ICA (refer to Figure 4.5 (a)) is significantly reduced by about 11% of the total amount compared to the complete CoW shown in Figure 4.5 (b), whereas the flow rate in the L-ICA is increased by about the same percent, which is in a good agreement with the experimental data (Hendrikse et al., 2005). The blood supply seems to be compensated entirely by ICAs, whereas the flow rate in the BA is maintained the same for the missing-A1 type. Thus, the total flow rate to the CoW for the missing-A1 case is almost unaffected. In contrast, the flow rate in BA is reduced by 7% for the missing P1 type (Figure 4.6 (b)), whereas the flow rate in the R-ICA is increased by about the same percentage. Therefore, the total afferent flow rate for the missing-P1 is also not affected. It can also be observed from other cases (Figure 4.6 (c) through (f)) the afferent flow rate maintains an approximately constant value due to the collateral effect. If percentage values are rounded, the respective ratios of contribution to the bilateral ICA and BA would be 40:40:20, 30:50:20 and 50:40:10 for the complete, missing-A1 and missing-P1 types, respectively. The results shown in Figure 4.6 are in excellent agreement with in vivo experiments (Tanaka et al., 2006; Hendrikse et al., 2005).



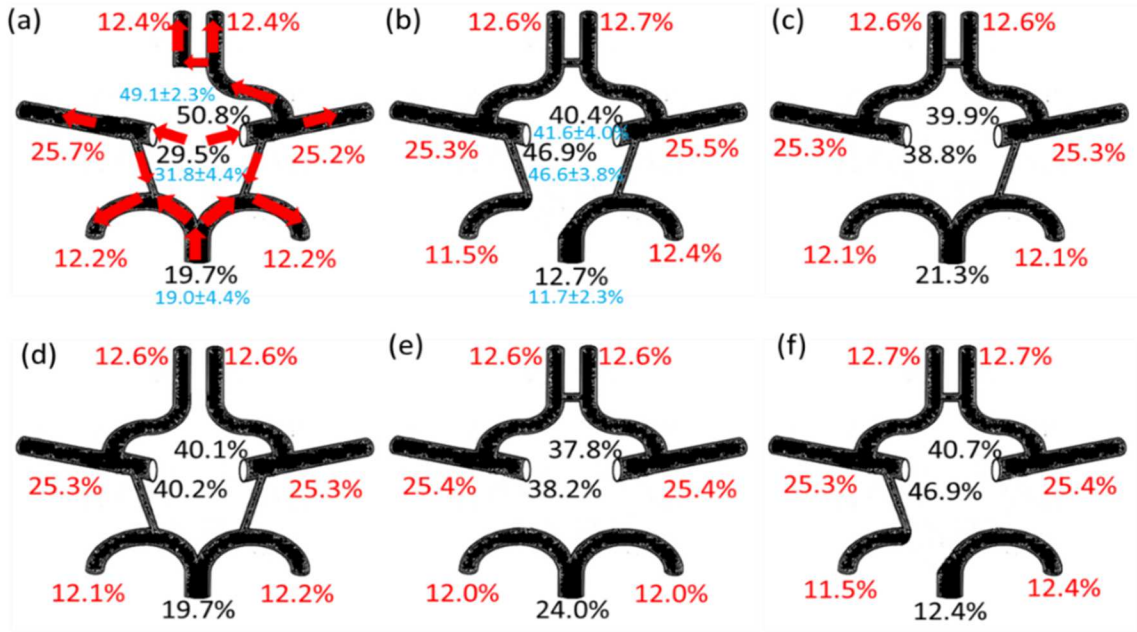


Figure 4.6 Flow rate distribution in CoW caused by the anomalies. The flow rates are in terms of their percentages to the total flow rates. Number in black is for afferent vessels from calculation, blue is for afferent vessels from experimental data (Tanaka et al., 2006), and red is for efferent vessels; (a) missing A1 artery, (b) missing P1 artery, (c) missing one PcoA, (d) missing AcoA, (e) missing both PcoAs, (f) missing P1-PcoA

Table 4.1 The CoW anomalies and their impacts on the total flow rate and the blood supply to different regions of the brain. The case is referred to Figure 22.

<i>Missing</i>	none	A1	P1	one PcoA	AcoA	both PcoA	P1 & PcoA	all coA
case	(a)	(b)	(c)	(d)	(e)	(f)	(g)	(h)
<b>Q (ml min<sup>-1</sup>)</b>	666	663	662	666	666	665	662	665
<b>P2:</b>	0.96:	0.98:	0.94:	0.96:	0.96:	0.95:	0.95:	0.95:
<b>MCA:</b>	2.01:	2.05:	2.01:	2.01:	2.01:	2.01:	2.01:	2.01:
<b>A2</b>	1.00	1.00	1.00	1.00	1.00	1.00	1.00	1.00

Table 4.2 Flow rate distribution in CoW for a subject with missing right A1. Flow rate in ml min<sup>-1</sup>. This Table is referred to the case of missing R-A1 in Figure 21 (a). The flow directions are shown as arrows.

Arteries	R/L ICA	R/L MCA	R/L P1	R/L P2	R/L A1	R/L A2	R/L PcoA	AcoA	BA
<b>Q (ml min<sup>-1</sup>)</b>	268.9/ 266.2	168.4/ 168.3	65.1/ 65.8	80.6/ 81.0	85.0/ 82.7	83.9/ 83.9	15.5/ 15.2	1.15	130.9

Furthermore, the temporal mean velocity in the midsection of AcoA during one cardiac cycle was calculated for WSS analysis. The biological normal wall shear stress for a straight artery ranges from 1.5 to 2.5 Pa, while a WSS >3.0 Pa is referred as a high WSS

(Dolan et al., 2013). The high WSS sensed by the endothelial cell in the arterial wall can trigger the mural-cell-mediated destructive remodeling, and thereby facilitate the initiation and growth of an aneurysm.

Figure 4.7 shows the comparison of instantaneous mean cross-sectional velocities between the complete CoW and the missing-A1 types. Assuming the flow in AcoA is a fully developed laminar Newtonian flow, the shear stress at the pipe wall can be estimated based on the mean velocity (Wilcox, 2000). As the shear stress is proportional to the mean velocity, the wall of AcoA in the missing-A1 types (either side) is subject to an excessively large shear force (almost three times larger) as compared to the complete case. It indicates that the WSS in AcoA could increase by about three times which is likely to induce local wall degeneration. This hypothesis is supported by a recently published clinical study which reported that variations in the A1 segment are correlated with a higher prevalence of AcoA aneurysms (Krasny et al., 2014).

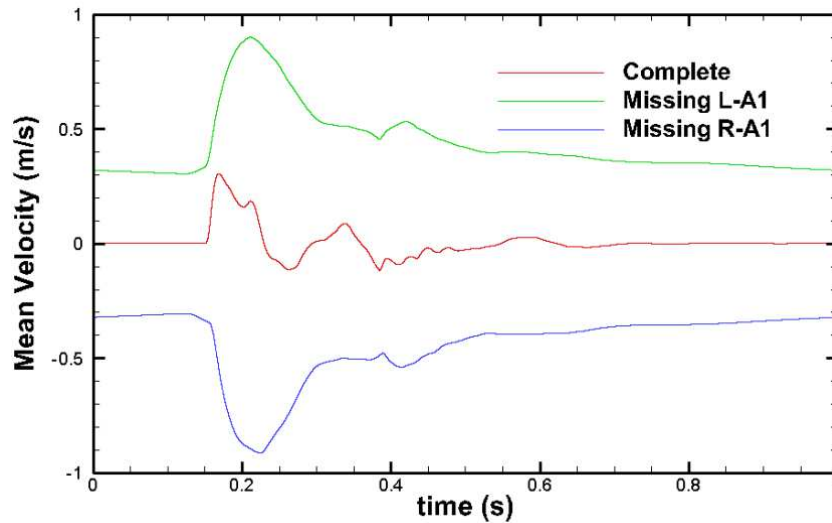


Figure 4.7 Comparison of the mean cross-sectional velocities at the midsection of AcoA for the complete, missing L-A1 and missing R-A1 types. The positive sign is defined from right to left.

#### 4.5 Simulation results vs. experimental results

The computational accuracy of the 1D model was evaluated by comparing the flow and pressure waveforms at eight selected locations of the flow network. Figure 4.8 and 4.9 depict the pressure and flow rate waveforms comparisons of the experiment with the 1D model at the center point of the upstream arteries of the CoW, including the main artery, CCA, SA, ICA, and VA-I. The comparison results indicate that the pressure occurred within the systolic time interval (between 0.25 – 0.6s) can be accurately reproduced by the 1D model. However, the 1D model underestimates the pressure about 15.38% at pre-systolic region and overestimates the pressure about 21.72% at diastolic regions. On the other hand, the comparisons of the flow rate waveforms show a good agreement between the 1D simulation and *in vitro* measurement. As can be seen from the flow rate comparisons in subclavian and vertebral arteries, wave oscillations were observed in the 1D model. This phenomenon could result from the radius contraction between the VA-I and VA-II, causing a minor wave reflection to induce the slight oscillations. Overall, the main features of the pressure and flow rate waveforms can be captured by the 1D numerical model.

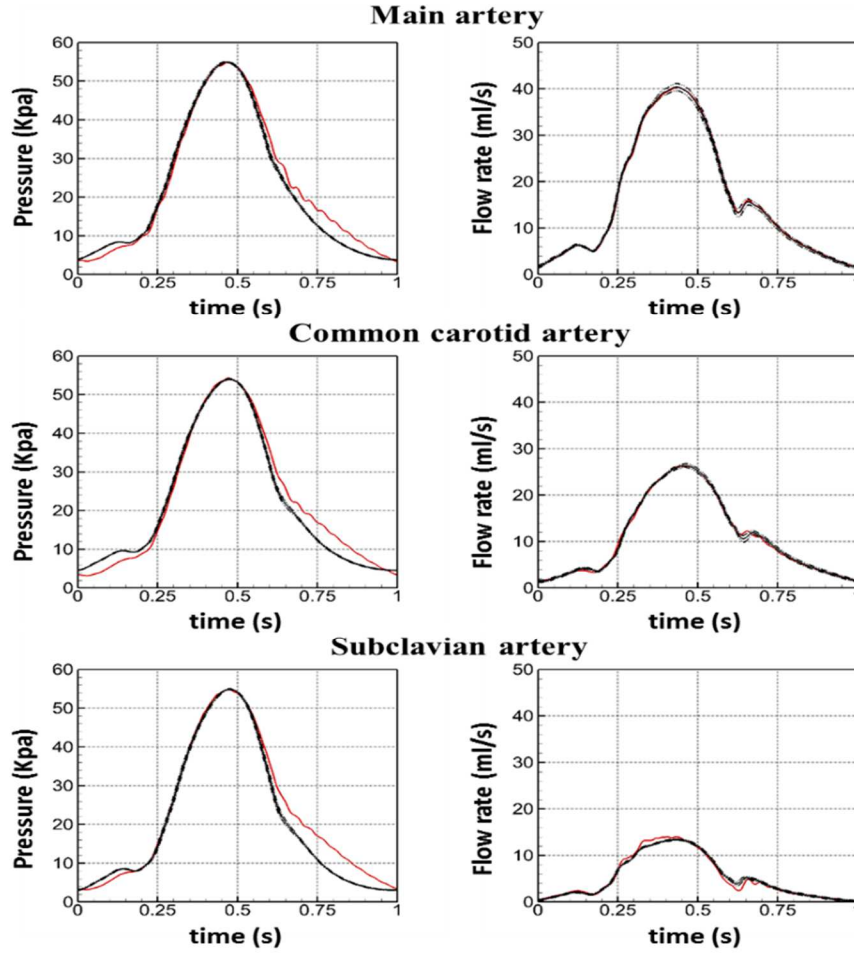


Figure 4.8 The pressure and flow rates Comparisons of the experimental with the numerical results at the main artery, common carotid artery, and subclavian artery. Black dash lines represent the standard deviation of the experimental measurement. Red lines represent the numerical results on the right side of the artery.

Figure 4.10 presents the pressure and flow rate comparisons of the experiment with the 1D model in three downstream arteries of the CoW model, including ACA, MCA, and PCA. It is demonstrated that the simulated results from the 1D model is capable of capturing the main characteristics obtained from the in vitro measurement data in the systolic regions (between 0.25 - 0.69s). Similarly, the 1D model under-predicts the pressure at the pre-systolic (before 0.25s) and over-predicts the pressure at the diastolic (after 0.69 s) regions.

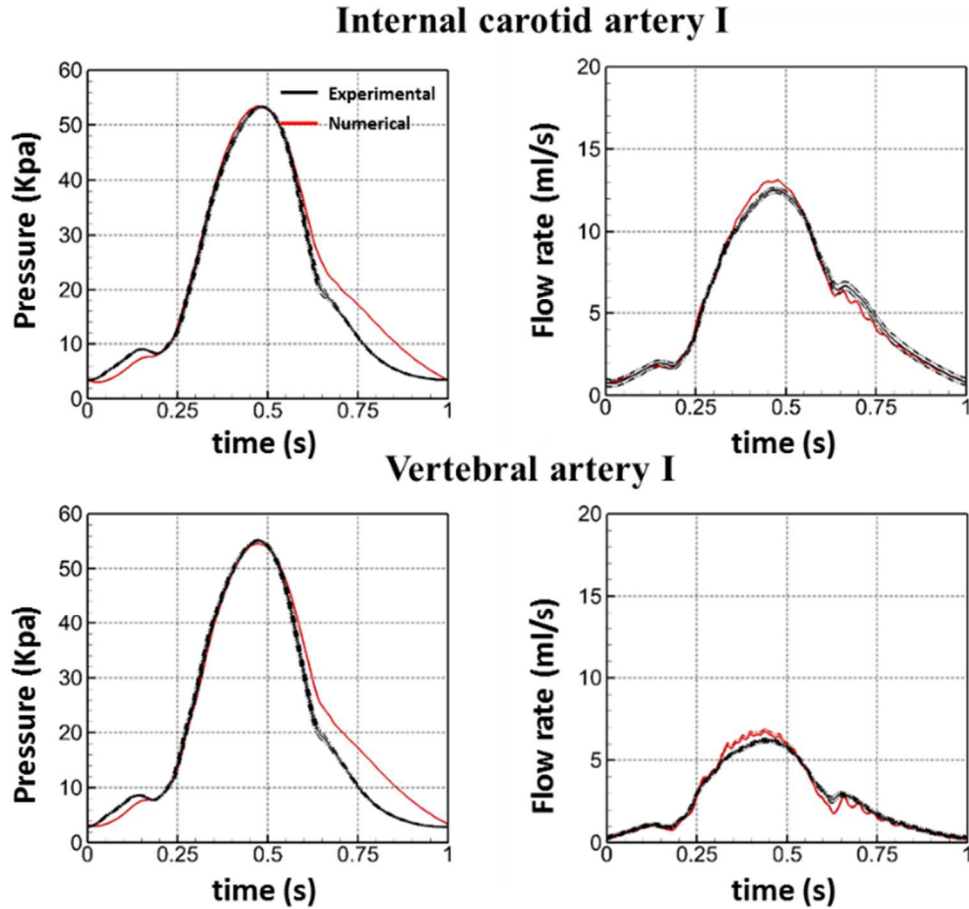


Figure 4.9 The pressure and flow rates Comparisons of the experimental with the numerical results at R/L internal carotid arteries I vertebral arteries I.

Mismatches in the flow rate comparisons can be observed at the peak and the dicrotic notch regions, as shown in Figure 4.10. The measurement results of the flow waveforms show that the dicrotic notch was attenuated leading to a relatively smoothed curve, as shown in Figure 4.10. The feature of the dicrotic notch was observed in the simulated flow waveforms, resulting in an underestimation in the time period between 0.63 – 0.8s as compared to the measurement data. This flow discrepancy results in an overestimation of the flow rate at the peak region, as presented in Figure 4.10. The mean values of the pressure and flow rates of the simulated and in vitro measurement results were compared in Table 4.3. A good agreement can be obtained from the flow rate comparisons, where

the overall errors between simulated and measurement results are smaller than 2%. However, significant discrepancy of pressure comparisons can be observed in the upstream arteries of the silicone CoW model, where the maximum error is 35.30% obtained from the ICA-I. The overall errors of pressure in downstream arteries of the silicone CoW model are less than 10%. The main difference of the pressure comparisons between the 1D model and experiment is attributed to the mismatches occurred at the pre-systolic and the diastolic period.

Table 4.3. Comparisons of the mean flow rate and pressure at various locations.

	Flow rate (ml/s)			Pressure (Kpa)		
	Measurement	Simulation	Difference	Measurement	Simulation	Difference
<b>Main artery</b>	<b>16.18</b>	<b>16.19</b>	<b>0.06%</b>	<b>17.92</b>	<b>22.76</b>	<b>27.00%</b>
<b>CCA</b>	<b>11.00</b>	<b>10.93</b>	<b>0.64%</b>	<b>16.65</b>	<b>22.35</b>	<b>34.23%</b>
<b>SA</b>	<b>5.22</b>	<b>5.26</b>	<b>0.77%</b>	<b>17.25</b>	<b>22.55</b>	<b>30.72%</b>
<b>ICA I</b>	<b>5.47</b>	<b>5.46</b>	<b>0.18%</b>	<b>16.26</b>	<b>22.00</b>	<b>35.30%</b>
<b>VA I</b>	<b>2.60</b>	<b>2.60</b>	<b>0.00%</b>	<b>17.05</b>	<b>22.38</b>	<b>31.26%</b>
<b>ACA VI</b>	<b>2.86</b>	<b>2.86</b>	<b>0.00%</b>	<b>4.09</b>	<b>4.37</b>	<b>6.85%</b>
<b>MCA VII</b>	<b>2.36</b>	<b>2.38</b>	<b>0.85%</b>	<b>3.91</b>	<b>3.92</b>	<b>1.02%</b>
<b>PCA VI</b>	<b>2.87</b>	<b>2.88</b>	<b>0.35%</b>	<b>3.24</b>	<b>3.56</b>	<b>9.88%</b>

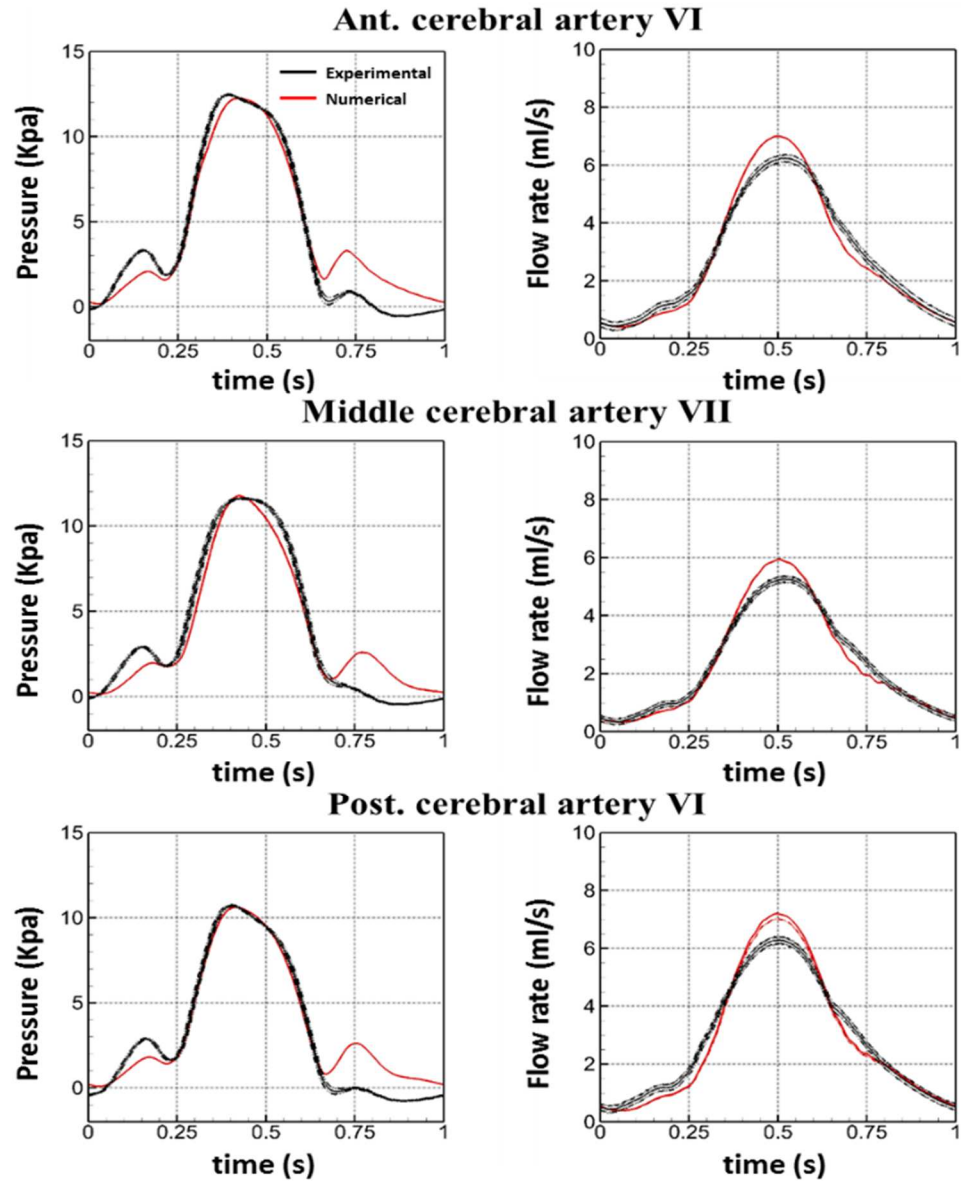


Figure 4.10 The pressure and flow rates Comparisons of the experimental with the numerical results at R/L anterior cerebral arteries, middle cerebral arteries, and posterior cerebral arteries. Black dash lines represent the standard deviation of the experimental measurement. Red dash lines represent the numerical results on the right side of the artery

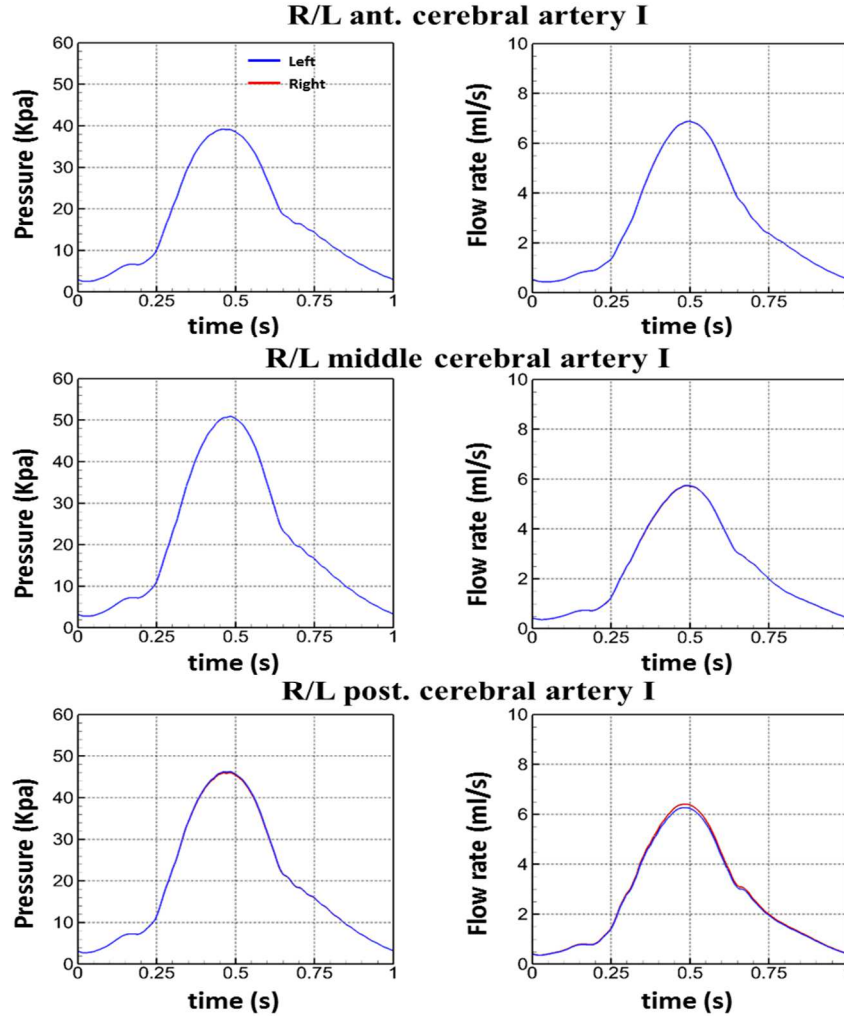


Figure 4.11 The pressure and flow rates Comparisons of the experimental with the numerical results at R/L anterior cerebral arteries, middle cerebral arteries, and posterior cerebral arteries. Figure 4.11 and 4.12 present the simulated flow rate and pressure waveforms of the arteries in the CoW, where these arteries cannot be measured due to the dimensions of the silicone model. The results of the pressure waveforms indicate that the pressure distributions on both right and left sides are almost identical, except a small difference appeared in the PCA resulting in a slight change (less than 1%) in flow rate distributions on both sides of the PCAs. It is worth noting that the tiny flow rate distribution was observed in the AcoA, as shown in Figure 4.12, resulting from the symmetric configurations of the assembled flow network. Theoretically, there should be a slight



flow rate ( $\sim 1\text{-}2\text{ ml/s}$ ) moving through the AcoA from the right to left side in a complete CoW configuration (Huang et al. 2015, Liang, et al. 2011). This behavior can be explained by that the right side of the common carotid artery, and subclavian artery are branched out from the brachiocephalic artery while the right common carotid artery and subclavian artery are both diverted directly from the arch of the aorta at a slight distance downstream of the aorta. The small pressure difference between both sides leads to the slight flow rate in the AcoA.

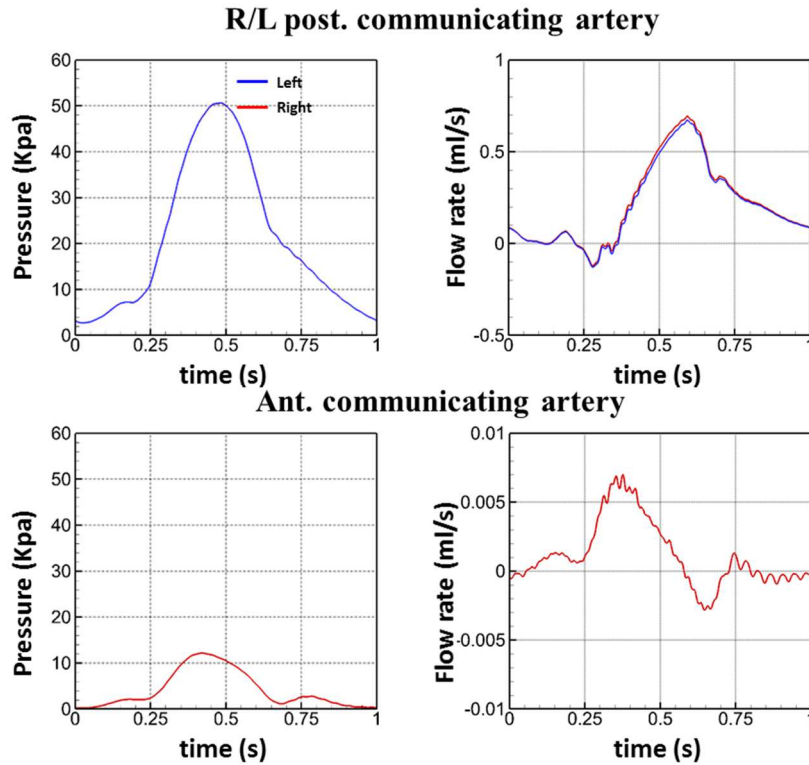


Figure 4.12 The pressure and flow rates Comparisons of the experimental with the numerical results at R/L posterior communicating arteries and anterior communicating artery.

## 4.6 Discussion

### 4.6.1 The variations of the CoW

The circle connection in CoW has been hypothesized to have the ability to perfuse deprived areas when a patient is missing one of the main arteries and/or communicating

arteries or undergoes occlusion of arteries. The self-regulation was believed to be caused by dilation and constriction of arterioles in response to different environmental stimuli (i.e., increased or decreased CO<sub>2</sub> or other biological stresses) (Alastruey et al., 2007). Nevertheless, the current study, for the first time, provides computational evidence that the self-regulation of CoW is a built-in mechanism associated with its particular circle structure.

Although CoW variations mentioned above do not seem to cause an immediate threat because the blood supply to different areas of the human brain is virtually unaffected, over time these variations may have a long-term effect and result in alterations of the geometry of individual vessels, and vascular stressors, such as initiation and/or rupture of intracranial aneurysms. It has been reported that the diameter of the functional collateral arteries of the CoW was significantly larger than that of the non-functional collateral arteries including the PcoA and P1 (Ahmed et al., 2015). The negative correlation was found between the diameter of the PCA and its accessory P1 (Ahmed et al., 2015), and between the diameter of A1 and P1 (Tanaka et al., 2006), respectively. These correlations implied that the diameter of the collateral arteries could be enlarged due to the missing or non-functional arteries of the CoW. On the other hand, based on present simulations the redistribution of blood flow through the CoW may cause specific vessels to carry excessive hemodynamic loads, high flow rates, and wall shear stresses, and hence lead to a high probability of an aneurysm in that region. For example, the missing-A1 variation causes the flow rate in the ipsilateral ICA to increase from 266 ml min<sup>-1</sup> to 337 ml min<sup>-1</sup> whereas the flow rate in the contralateral ICA is reduced by the same amount, as shown in the comparison of Figure 4.5 (a) and Table 4.1. The AcoA is then responsible for

correcting/shunting the imbalanced blood flow from the ipsilateral A1 to the contralateral A2. In the case of the missing-R-A1 type, the flow rate in the AcoA is substantially changed from  $1.15 \text{ ml min}^{-1}$  to a reverse flow of  $82.1 \text{ ml min}^{-1}$ .

#### 4.6.2 The experimental study

The experimental study of blood flow in a silicone model of a complete CoW was conducted to assess the accuracy of the 1D numerical model. Differences can be observed mainly from the pre-systolic and diastolic regions for pressure comparisons and the peak region for flow rate comparisons. These mismatches might result from the use of the two types of tubes assembled in the experiment, which are the Tygon and silicone tubes. The Tygon tube has a very uniform wall thickness and elasticity, whereas these two parameters of the silicone model cannot be promised to be uniformly manufactured for the entire model, especially at the junctions. However, the assumption of a constant elasticity and wall thickness for the silicone tubes were initialized in the 1D model probably resulting in some errors between the simulated and experimental results. Alastruey et al., (2011) demonstrated that the 1D visco-elasticity model is able to reduce the errors between the simulation and experimental results particularly on damping peripheral oscillations by taking the vessel wall viscosity into consideration. Thus, the further experimental study is required by using one type of the cerebrovascular tree model with more uniformed thickness and elasticity for the whole flow network and considering the visco-elaticity model into account in the 1D model.

Flow control valves were adopted to connect to the overflow reservoir served as the outflow conditions, providing a constant resistance and aiming to quantify its parameters simply. This single resistance could reduce the non-physiological wave reflection from

terminals to upstream in the 1D blood flow simulation (Alastruey et al. 2008). Matthys et al. (2007) evaluated the effects of different 0D models on the upstream pressure and flow rate waveforms, including RL and RCR. The results indicate that the adding of inductance can increase the oscillations in waveforms. However, the RCR model is able to reduce the oscillations and achieve a smooth curve due to Windkessel effect (Matthys et al. 2007). The effect of the variations of the terminal 0D models used in the 1D model and setup in the experiment will be investigated in the future study to improve the wave reflection from the distal ends.

#### 4.7 Summary

In this chapter, a number of CoW variations were studied, and results were compared with that of the complete CoW. The total blood flow rate to the CoW is minimally affected by its variations. The rate is either congenital or subjected to missing one of the main arteries and/or communicating arteries. The special structure of the CoW has the ability to shunt blood flow to different areas of the brain. The present study demonstrates that this shunting behavior requires no external stimulus and it is purely an emergent effect of CoW. Although the flow rates in the efferent arteries (distal to CoW) remain unaffected by the variations in the CoW, the flow rates in afferent vessels may be subject to substantial changes. Last but not the least, the redistribution of flow rates resulting from CoW variations may cause particular vessels to undergo excessive hemodynamic loads induced by the increased flow rate (Huang et al., 2018).

In the meantime, an experimental study of blood flow in a silicone arterial network was conducted to assess the accuracy of a previously published 1D numerical model. The transient flow and pressure waveforms were measured in eight selected locations

distributed at both upstream and downstream arteries of the CoW. The comparison results of the pressure waveforms indicate that the 1D model is able to capture the main features occurred at the systolic regions, whereas under- and overestimation of the pressure about 15.38% and 21.72% can be observed at the pre-systolic and diastolic regions, respectively. On the other hand, the flow rate waveforms measured from the upstream arteries can be accurately reproduced by the 1D model. However, some discrepancies of the flow rate comparisons can be found in the downstream arteries of the CoW mainly due to the assumption of the uniformed elasticity in the 1D model. Quantitatively, the mean flow rates through all measured arteries can be precisely predicted by the 1D model, and the overall difference between the numerical and experimental results is smaller than 1%.

## **5 THE INFLUENCE OF THE VASCULAR AGING**

### **5.1 Overview**

Cardio- and cerebrovascular diseases, such as atherosclerosis, ischemic stroke, and hemorrhagic stroke, are among the most common factors of death in the world for elderly patients in the world (Thom et al., 2006). Age-associated alterations in cardiovascular structure and function, together with pathophysiological disease mechanisms, determine the threshold, severity, and prognosis of cardiovascular diseases in elder patients (Lakatta et al., 2003). Normal vascular aging has been described as a gradual process involving biochemical, enzymatic, and cellular changes of the vasculature and modification of the signals that modulate those (Kotsis et al., 2011). Gerontologists and epidemiologists have investigated why aging confers enormous risk for cardiovascular disease. Cross-sectional studies have demonstrated that prominent structural alteration manifested wall thickening and dilatation in large elastic arteries during aging (Lakatta, 1993). Age-associated increases in intimal media thickening are usually accompanied by both luminal dilations and increase in the stiffness of vascular walls. Increased PWV and aortic AIx were traditionally used as markers to identify structural changes in vascular media, including increased collagen fraction, reduced elastin content, elastin fractures, and calcification. Previous studies have demonstrated that elevations in pulse pressure in middle-aged patients are a predictor of clinical disease (Antikainen et al., 2000).

Recently, a new concept of EVA, defined as the acceleration of typical vascular aging, has emerged to explain the increased risk of cardiovascular events in the middle-aged population (Cunha et al., 2015). EVA was usually identified as the case with PWV values higher than the 95th percentile for age and sex. It is claimed that patients with values of

PWV higher than the 95% confidence intervals of the mean of age are at high risk for EVA (Kotsis et al., 2011).

The mean PWV value, which is adjusted for age by using the normal population PWV values as a comparator, was used as a marker for early vascular aging in cohort studies to identify individuals presenting accelerated and premature arterial aging (Nilsson, 2008). In comparison with NVA, EVA features increased arterial stiffness, dilation of central elastic arteries, and impaired endothelial function (Cunha et al., 2015; Nilsson, 2014). It has been well documented that age-associated degenerative changes in arteries correlate closely with the development of atherosclerosis, systolic hypertension, and stroke (Lakatta et al., 2003).

In recent years, one-dimensional models were widely used to study arterial wave propagation (Alastruey et al., 2007; Huang et al., 2015; Müller et al., 2014). A review of 0D and 1D models of the cardiovascular system summarized different modeling approaches and highlighted their pros and cons (Shi et al., 2011). A closed-loop model of the cardiovascular system has been employed to quantify the coupled ventricular-arterial hemodynamic changes associated with NVA (Liang et al., 2009). However, hemodynamic characteristics of EVA as compared to NVA, especially in cerebral arteries, have not been addressed. In this chapter, the THINKS model was enhanced to simulate the hemodynamic characteristics in both EVA and NVA subjects so as to analyze the correlation of EVA with cardiovascular diseases. Herein, the emphasis was placed on comparing the simulated pressure and flow waveforms in central arteries and cerebral arteries under EVA and NVA conditions.

## 5.2 Cardiovascular system

In the calculation, the heart was assumed at 60 beats per minute. The 25-year-old subject NVA was chosen as the base test. The parameters for arterials and venous tree, lumped models, and heart model are given in the previous report by Huang et al., (2015).

Figure 5.1 shows the hemodynamic characteristics of the heart in one cardiac cycle for both the NVA and EVA subjects aged 25 years. Table 5.1 presents comparisons of simulated hemodynamic variables and in vivo measurements data for the NVA and EVA subjects aged 25 and 85 years, respectively (Cunha et al., 2015; McEniery et al., 2005; Saeed et al., 2014; Arbab-Zadeh et al 2004; Aune et al., 2009; Dexter et al., 1950; Fowler et al., 1953; Gayat et al., 2011; Han et al., 2013; Kawaguchi et al., 2003; Salton et al., 2002; Schlant et al., 1994; Yamaguchi et al., 2006). From comparisons, all indices are very close to the measured data. The afterload on the left ventricle increases due to the arterial stiffness, end diastolic volume, and end systolic volume of the left ventricle—which notably declines during aging (Cain et al., 2009).



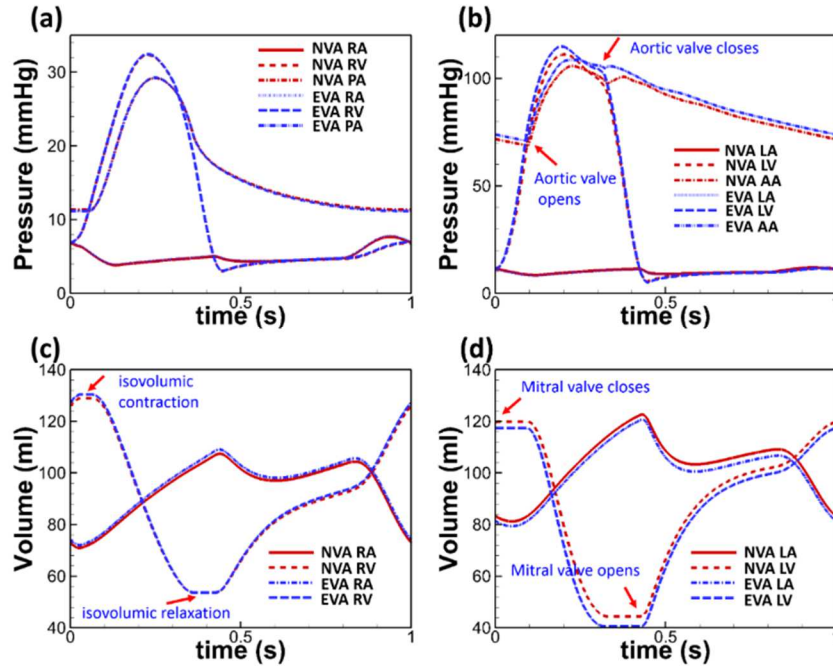


Figure 5.1 Simulated hemodynamics for the heart for both the NVA and EVA male 25 years, which consists of four cardiac chambers. RA, right atrium; RV, right ventricle; LA, left atrium; LV, left ventricle. (a) and (b) show the blood pressure in the heart chambers, pulmonary artery, and ascending aorta; (c) and (d) show the volume in the heart chambers.

Table 5.1 Comparison between measurements and simulations.

Variable	measured data	NVA 25 yr	NVA 85 yr	EVA 25 yr	EVA 85 yr
Stroke volume ( ml)	<b>74.5±23.8</b> <sup>(Kawafuchi et al., 2003)</sup> , <b>71.7±10.8</b> <sup>(Kawafuchi et al., 2003)</sup>	<b>77.81</b>	<b>77.67</b>	<b>77.00</b>	<b>78.59</b>
Ejection fraction (%)	<b>66.8±7.2</b> <sup>(Kawafuchi et al., 2003)</sup> , <b>62.9±7.2</b> <sup>(Kawafuchi et al., 2003)</sup> , <b>63.67±7.49</b> <sup>(Han et al., 2013)</sup> , <b>62(59-66)</b> <sup>(Gayat et al., 2011)</sup>	<b>63.65</b>	<b>68.06</b>	<b>65.67</b>	<b>69.46</b>
LVSP (mmHg)	<b>90-140</b> <sup>(Schlant et al., 1994)</sup>	<b>111.09</b>	<b>124.69</b>	<b>113.81</b>	<b>130.30</b>
LVEDP (mmHg)	<b>4-12</b> <sup>(Schlant et al., 1994)</sup>	<b>5.50</b>	<b>4.59</b>	<b>5.06</b>	<b>4.39</b>
RVSP (mmHg)	<b>17-31.5</b> <sup>(Fowler et al., 1953)</sup>	<b>32.32</b>	<b>32.23</b>	<b>32.37</b>	<b>32.39</b>
RVEDP (mmHg)	<b>-0.5-7</b> <sup>(Fowler et al., 1953)</sup>	<b>2.99</b>	<b>2.99</b>	<b>3.00</b>	<b>3.01</b>
LVESV (ml)	<b>36</b> <sup>(Salton et al., 2002)</sup>	<b>44.44</b>	<b>36.45</b>	<b>40.26</b>	<b>34.56</b>
LVEDV (ml)	<b>119±19</b> <sup>(saeed et al., 2014)</sup> , <b>115</b> <sup>(Salton et al., 2002)</sup>	<b>122.25</b>	<b>114.12</b>	<b>117.26</b>	<b>113.15</b>
LA (ml)	<b>35±7 (25 yr)</b> <sup>(Yamaguchi et al., 2006)</sup> , <b>38±6 (55 yr)</b> <sup>(Yamaguchi et al., 2006)</sup> , <b>30-84</b> <sup>(Arbab-Zadeh et al., 2004)</sup>	<b>41.71</b>	<b>40.89</b>	<b>42.40</b>	<b>40.93</b>
RVESV (ml)	<b>52</b> <sup>(Schlant et al., 1994)</sup>	<b>53.58</b>	<b>53.02</b>	<b>53.48</b>	<b>53.21</b>
RVEDV (ml)	<b>136</b> <sup>(Schlant et al., 1994)</sup>	<b>129.67</b>	<b>117.77</b>	<b>130.18</b>	<b>117.08</b>
RA (ml)	<b>36-100</b> <sup>(Arbab-Zadeh et al., 2004)</sup>	<b>36.54</b>	<b>37.39</b>	<b>36.73</b>	<b>37.72</b>
Systolic pressure (mmHg)	<b>NVA: 124±10 (25 yr), 125±9 (55 yr), 130±8 (85 yr)</b> <sup>(Aune et al., 2009)</sup> <b>EVA: 125±15 (30 yr)</b> <sup>(Cunha et al., 2015)</sup> , <b>148±21 (52 yr)</b> <sup>(saeed et al., 2014)</sup>	<b>123</b>	<b>138</b>	<b>125</b>	<b>144</b>
Pulmonary artery (ESP/EDP/mean)	<b>19-26</b> <sup>(Arbab-Zadeh et al., 2004)</sup> , <b>11-29</b> <sup>(Fowler et al., 1953)</sup> / <b>6-12</b> <sup>(Arbab-Zadeh et al., 2004)</sup> , <b>4-13</b> <sup>(Fowler et al., 1953)</sup> / <b>13-12</b> <sup>(Arbab-Zadeh et al., 2004)</sup> , <b>8-19</b> <sup>(Fowler et al., 1953)</sup>	<b>29.20 / 11.32 / 17.28</b>	<b>28.92 / 11.04 / 17.00</b>	<b>29.18 / 10.84 / 16.95</b>	<b>29.09 / 10.79 / 16.89</b>

LVSP, left ventricle systolic pressure; LVEDP, left ventricle end diastolic pressure; RVSP, right ventricle systolic pressure; RVEDP, right ventricle end diastolic pressure; LVESV, left ventricle end systolic volume; LVEDV, left ventricle end diastolic volume; RVESV, right ventricle end systolic volume; RVEDV, right ventricle end diastolic volume; LA, left atrium; RA, right atrium. (Cunha et al., 2015): mean value in 260 subjects with EVA less than 50 years old; (McEniery et al., 2005): mean value in 183 normal male subjects (age: 30-39 years); (Saeed et al., 2014): mean value in 38 EVA male subjects (mean age: 52 years); (Arbab-Zadeh et al 2004): normal young subjects (7 male, 7 female; mean age, 28.9±5 years); (Aune et al., 2009): normal reference range determined from measurements in 79 normal male subjects (age: 29-80 years); (Dexter et al., 1950): mean value in 8 subjects with a normal cardiovascular-pulmonary system; (Fowler et al., 1953): normal reference range determined from measurements in 18 normal subjects and a review of the data of 54 normal subjects; (Gayat et al., 2011): mean value in 10 subjects (mean age: 35.9 (31.7-49.7)); (Han et al., 2013): mean value in 852 healthy participants (aged 30-98 years, 46% men); (Kawaguchi et al., 2003): mean value in 14 young subjects (mean age:36) and 9 old subjects (mean age: 65); (Salton et al., 2002): mean value in 63 normal male subjects (mean age: 56.7 years); (Schlant et al., 1994): normal reference range obtained in population based in vivo studies; (Yamaguchi et al., 2006): mean value in 25 subjects (age ≥ 20).

Figure 5.2 compares aortic systolic pressures against the data reported in previous works (Liang et al., 2009 and McEniery et al., 2005). From the results, one can observe that the simulated results for the NVA subject are in good agreement with existing data, and the central systolic pressure in the EVA subject is 6 mmHg higher in average than that in the NVA subject. Additionally, age-associated arterial stiffening leads to the increase of central pulse pressure and AIx. Figure 5.3 (a) and (b) present the central pulse pressure and augmentation index compared against previous data (McEniery et al., 2005).

The pulse pressure of the NVA matches the measurement data, whereas the pulse pressure of the EVA subject is higher than that of the NVA subject and measurement data. Similarly, the AIx of the EVA is larger than that of the NVA in each decade. The augmentation index is the ratio of central augmentation pressure to the pulse pressure. The augmentation pressure was calculated by the subtraction of inflection pressure from the central systolic pressure, where the inflection pressure is derived from the second derivative of the pressure wave.

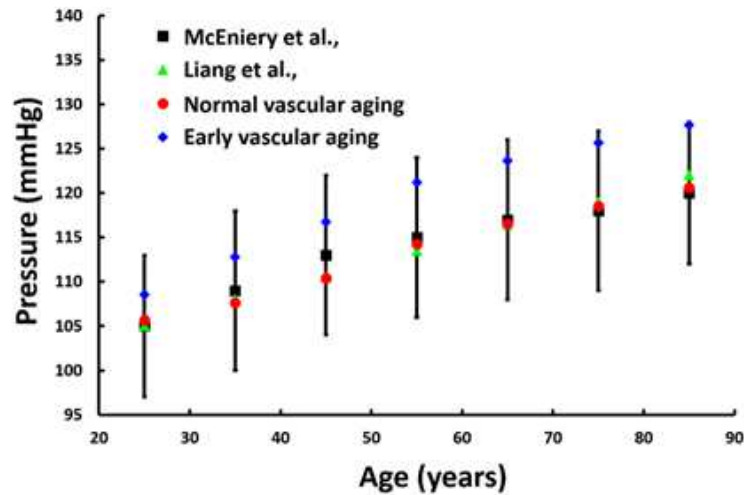


Figure 5.2 Comparisons between the simulated data and the measured data of central systolic pressure for both the NVA and EVA.

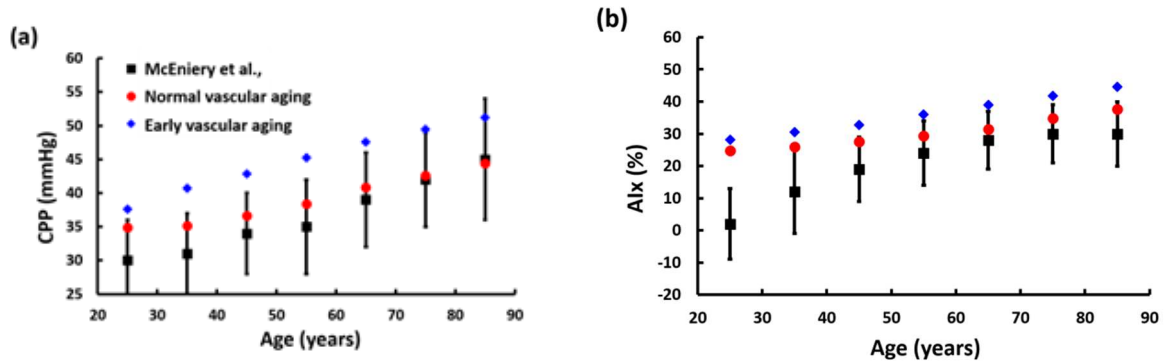


Figure 5.3 Comparison between the simulated and the measured data for both the NVA and the EVA; (a) the central pulse pressure, and (b) the central augmentation index.

Figure 5.4 shows the simulated mean flow rates in some major veins (in subjects aged 25 years) compared against measured data (Cheng et al., 2003; Fortune et al., 2003; Nabeshima et al., 1995; Stoquart-ElSankari et al., 2009). The mean flow rate of the EVA subject is slightly higher than that of NVA subject, and all simulation results fall in the range of the reported data. Figure 5.5 shows comparisons of the blood pressure propagation along the arterial tree with previous work among simulations aged 25, 55, and 65 years (Nichols et al., 1993). It is illustrated that the EVA subject shows higher systolic pressure than that of the NVA subject, and the main features of the measurement data can be captured by both simulations.

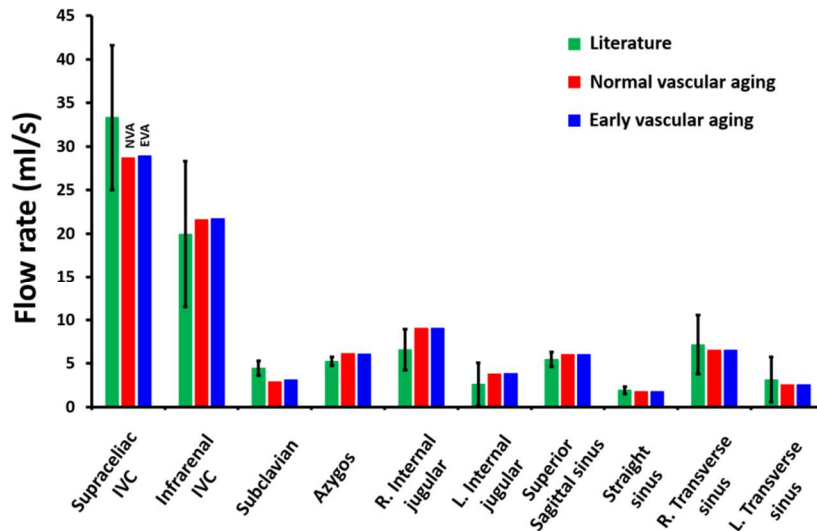


Figure 5.4 Mean blood flow in the selected veins: computational results versus literature data.

### 5.3 Validation

In order to Figure out the influence of the cerebral hypertensive pressure, the hemodynamic characteristics in the CoW were assessed. First, Figure 5.6 presents the validation of the total flow rate entering the CoW. The total flow rates for the EVA and NVA subjects are 595.97 ml/min and 583.33 ml/min respectively, which fall into the range of measurement data (Hendrikse et al., 2005).

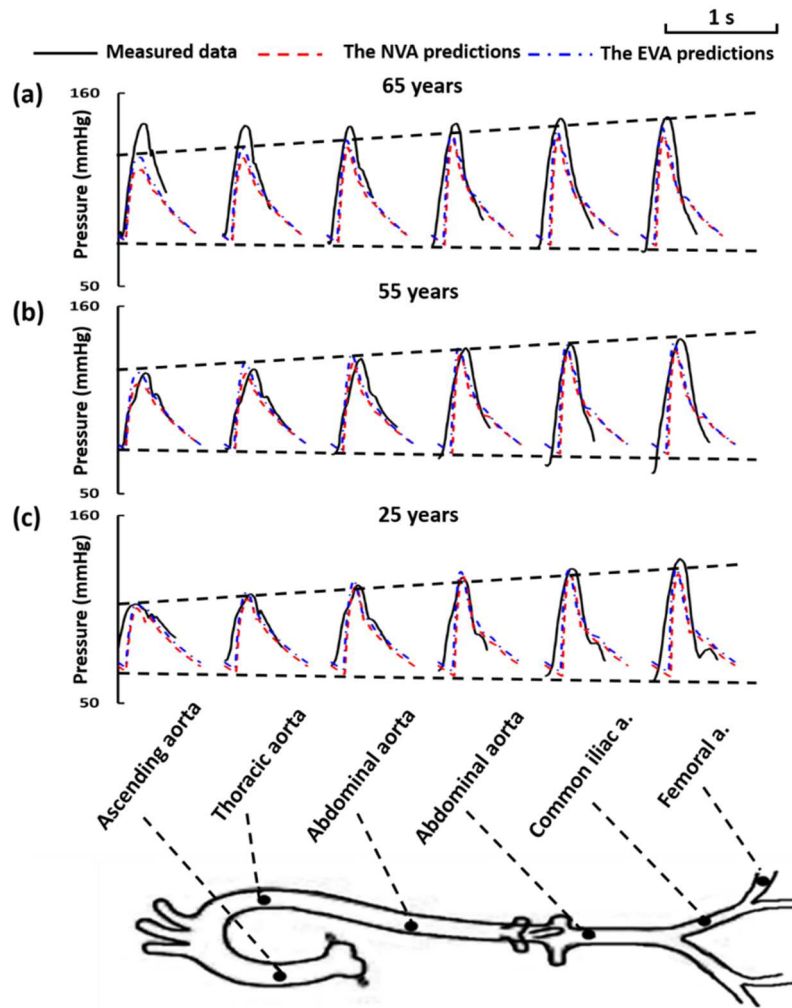


Figure 5.5 Arterial pressure propagation along the arterial tree during one cardiac cycle.

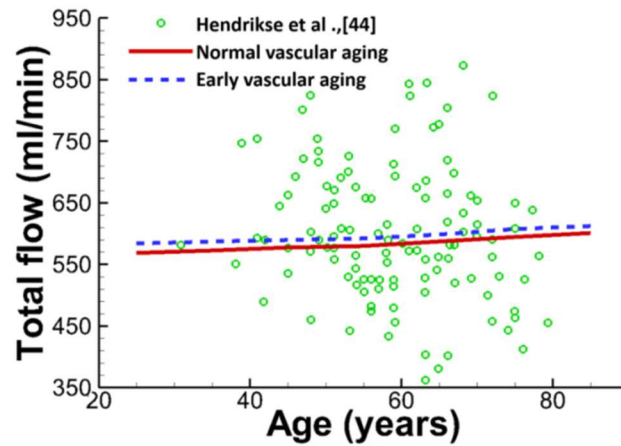


Figure 5.6 Comparison of the total flow rate entering the CoW between the simulated NVA, EVA, and the measured data.

Figure 5.7 shows the validation of the flow rate waveforms in comparison with the measured waveforms (Reymond et al., 2011). The square symbols shown in the Figure represent the averaged flow rate waveforms from measurements, and the error bar presents the 95% CI. Overall, a phase shift in the waveform for the EVA subject can be observed, and the following second peak also occurred earlier than that of the NVA subject, which can be observed clearly in Figures 5.6 (a), (b), and (d). On the other hand, in Figure 5.7 (a), the flow rate in the Middle Cerebral Artery (MCA) for the EVA and NVA subjects is 21.87% higher than the measured mean systolic flow rate in average. Similarly, in Figure 5.7 (d), the peak systolic flow rate in the Common Carotid Artery (CCA) is 14.9% higher than the measured peak systolic flow rate. On the contrary, Figures 5.7 (b) and (c) show that the flow rate waveforms in the Vertebral Artery (VA) and Internal Carotid Artery (ICA) are in agreement with the measured flow rate waveforms. Minor differences with experimental data were observed in the flow rates of the diastolic region (from 0.5 s to 1 s), and the current aging models do not seem to change the profile shapes in this region very much.

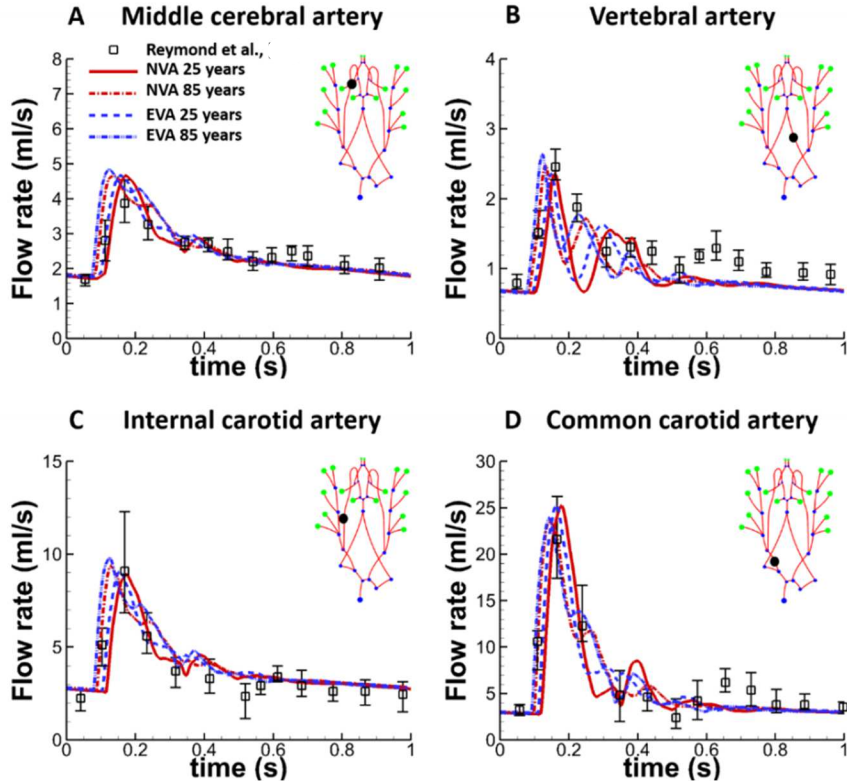


Figure 5.7 Comparison of the flow rate waveform between the simulated NVA, EVA, and measured waveform in four arterial sites as the large black dot indicates in the arterial tree. A is the flow rate in the middle cerebral artery; B is the flow rate in the vertebral artery; C is the flow rate in the internal carotid artery; D is the flow rate in the common carotid artery.

#### 5.4 Configurations of CoW

The CoW has been investigated by presenting the alterations of pressure and flow rate in a complete CoW and incomplete CoW (Liang et al., 2011; Alastruey et al., 2008). Figure 5.8 presents the pressure and flow rate waveforms in the AcoA and PcoA arteries with a complete CoW. Overall, the pressure in the EVA subject aged 25 years is slightly higher than that of NVA at the same age in AcoA and PcoA arteries, whereas the pressure for the EVA subject aged 85 years is 5.60 mmHg and 6.75 mmHg larger than the NVA subject at the same age in the AcoA and PcoA arteries, respectively. Indeed, Table 5.2 presents the rates of pressure rise in the AcoA and PcoA arteries with complete and incomplete CoW, which are calculated based on the pressure change from the beginning of the cardiac cycle to the

systolic peak for both NVA and EVA subjects at 25 and 85 years old. Overall, the rates of pressure rise in EVA subjects at 25 and 85 years old are approximately 5% and 9% respectively, higher than those of NVA, mainly resulting from the phase shift of pressure waveform for EVA subjects. On the other hand, the flow rate decreases in these two arterial sites with the increase of age. The flow rates in the AcoA and PcoA arteries in the EVA subjects aged 25 and 85 years are slightly lower than the counterpart of NVA.

Figure 5.9 shows comparisons of the pressure and flow rate waveforms in AcoA and PcoA arteries for the EVA and NVA subjects with an incomplete CoW featured by missing RA1 or RP1. For the incomplete CoW, the pressure waveform becomes slightly lower than the counterpart in a complete CoW. Due to the built-in collateral function of CoW, the flow rates in AcoA and PcoA arteries are much higher than those with the complete CoW, as shown in Table 6. This effect is amplified by EVA; thus higher values of flow rates in AcoA and PcoA were observed in EVA elder subjects. Again, the phase shift of systolic flow rate can be clearly observed for both cases in the EVA subject, and for pressure. The systolic pressure is even higher due to the reflected wave from peripheral sites.



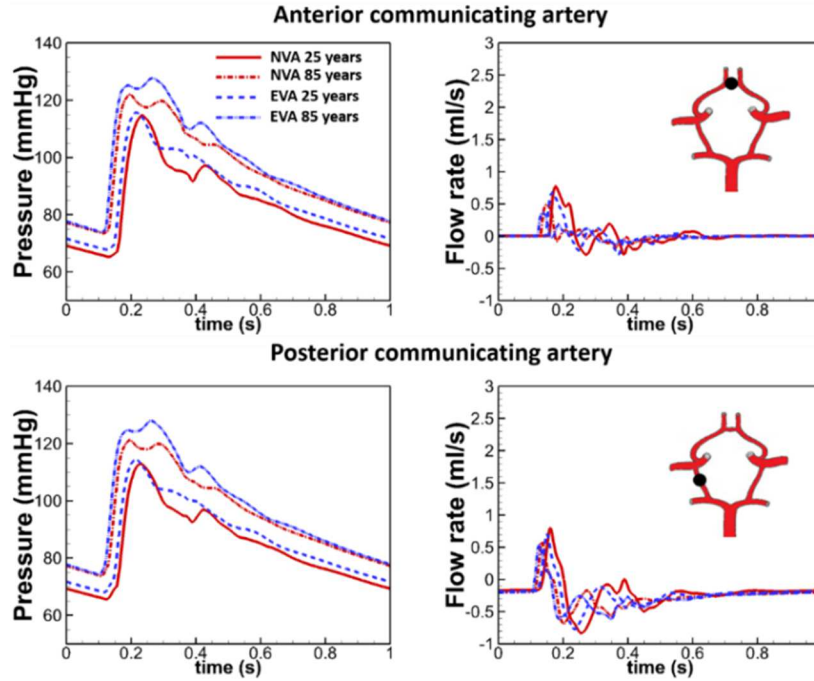


Figure 5.8 Comparisons of the pressure and flow rate waveform in a complete CoW. Top two waveforms represent the pressure and flow rate in the anterior communication artery; bottom two waveforms represent the pressure and flow rate in the posterior communicating artery.

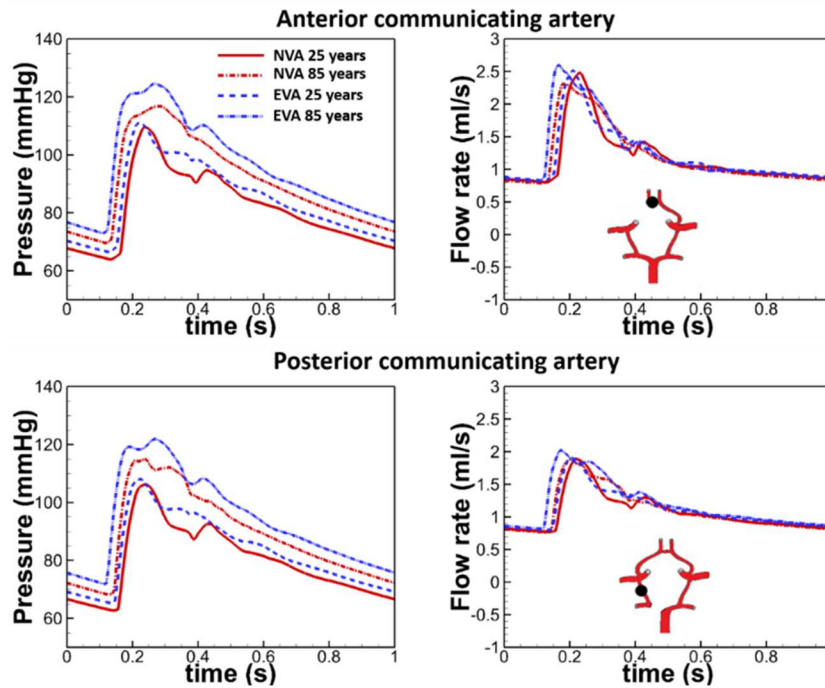


Figure 5.9 Comparisons of the pressure and flow rate waveform in an incomplete CoW. Top two waveforms represent the pressure and flow rate in the anterior communication artery with missing RA1; bottom two waveforms represent the pressure and flow rate in the posterior communicating artery with missing RP1.

## 5.5 Discussion

Results from the present simulation were validated for various arteries by comparison with in-vivo experimental data. Our results show that a subject with EVA has larger aortic cerebral pressure than those of an NVA subject. Moreover, the hemodynamic characteristics in the CoW indicate that elder subjects with EVA possess higher systolic pressure due to the early arrival of reflected waves, which may be associated with a higher risk of hypertension and hyperperfusion in the cohort. For an incomplete CoW with missing RA1 or RP1, a dramatic increase of flow rates in AcoA and PcoA arteries was observed, and this trend was further amplified by EVA.

As shown in Figure 5.2, the central systolic pressure increases with aging. Compared to the NVA, the EVA subject has a greater peripheral resistance and stiffer arterial wall properties, leading to an elevated central systolic pressure, central pulse pressure, and augmentation index (shown in Figure 5.3). The increase in central systolic pressure during aging poses additional afterload on the ventricle, which is especially pronounced in the case of EVA. These aspects are determined by the flow in the microcirculation in the terminal of the arterial system and the arterial stiffness (Nichols, 1985). The aortic systolic pressure can be separated into the forward-traveling and backward-traveling components. The forward component is determined by the left ventricular contraction, and the backward component is determined by the reflected wave from the peripheral circulation, resulting from the impedance mismatch at different junctions downstream of the arterial tree (Lee et al., 2009). Therefore, the pulse pressure and AIx would partly reflect the degree of increase in central arterial stiffness and peripheral resistance following aging. Note that the simulated AIx shown in Figure 5.3 (b) exhibits a nearly linear increase with age until the eighth decade

rather than a nonlinear increase (McEniery et al., 2005). The discrepancies may be due to the limitations in parameter adjustment for simulating aging in our study. For example, age-associated nonlinear aortic dilation and arterial stiffening were not fully taken into account, due to the lack of availability in vivo data. These factors affect the reduction in arterial compliance with age, leading to a nonlinear increase in AIx with age, especially in elderly subjects. Overall, the observation indicates that the elevated pulse pressure and AIx could lead to a rise in the arterial wall stress progression of atherosclerosis and the development of left ventricular hypertrophy (Sako et al., 2009). Figures 5.2 and 5.3 demonstrate that EVA could result in these diseases in middle age compared to NVA because higher central systolic pressure and AIx appears in younger ages (Reference values).

The NVA and EVA have been examined in terms of the pressure propagation along the arterial tree during aging among subjects aged 25, 55, and 65 years by comparing with measurements, aiming to further determine the hemodynamic change, as depicted in Figure 5.5. The shape of waves is varying depending on the wave reflection from the peripheral sites and the arterial stiffness (Nichols et al., 1993). For the case of subjects aged 25 years, in Figure 5.5 (c), NVA has shown the secondary peak after systole in the ascending aorta, while EVA indicates that the secondary peak is merging with systolic pressure because of the earlier arrived wave reflection. With the increase of age, in Figure 5.5 (b), all pressure wave shapes of EVA become sharper, whereas NVA shows a small pressure drop after the systolic in the ascending aorta. In the final stage, the forward pressure overlapped with backward pressure in the elderly, contributing even higher systolic pressure in the EVA subject, as can be seen in the terminal of the arterial tree in the subject aged 65 years, as shown in Figure 5.5 (a). The higher aortic pressure in the EVA middle-aged subject could

potentially lead to diastolic dysfunction of the heart. The large afterload on the left ventricle results in strain while ejecting blood, which has been shown to thicken and stiffen the wall of the heart (van de Vosse et al., 2011). Therefore, the EVA subject has a higher risk of cardiovascular disease than that of NVA, starting from middle age.

Moreover, a comprehensive understanding of flow patterns in the CoW would be beneficial for predicting the risk factor for cerebral hypertensive pressure, which is associated with intravascular disease in older adults, such as an aneurysm and stroke (Muntner et al., 2015; Taylor et al., 1995). Previous studies demonstrated that the CoW abnormalities host more aneurysms on the AcoA and PcoA arteries than other sites (Kayembe et al., 1984; Krasny et al., 2014; Songsaeng et al., 2010), and many patients are diagnosed with an intracranial aneurysm in middle ages in the setting of uncontrolled hypertension.

In Figure 5.8, the results indicate that the EVA subject shows greater systolic pressure than the NVA subject and a slight phase shift is noted. Again, Table 5.3 shows that the systolic pressure appears early for the EVA subjects. Generally, the AcoA and PcoA arteries are thinner compared to other vessels in the CoW. This caliber change could cause these vessels and especially junctions of these vessels to be less tolerant of high pressure because of the endothelial dysfunction and arterial stiffness found in the elderly. The prevalence of stroke-related to intracranial aneurysms is higher in the setting of hypertension.

Table 5.2 The rate of pressure rise from diastolic to systolic in AcoA and PcoA with complete and incomplete CoW, corresponding to left RA1 and RP1, for the NVA and EVA subjects with 25 and 85 years.

	Rate of pressure rise (mmHg/s)			
	NVA-25(yr)	NVA-85(yr)	EVA-25(yr)	EVA-85(yr)
AcoA with complete CoW	194.63	227.78	205.03	248.36
PcoA with complete CoW	188.49	224.12	198.21	247.25
AcoA with incomplete CoW	176.43	206.91	183.92	225.76
PcoA with incomplete CoW	164.00	206.31	172.83	228.21

Furthermore, the pressure and flow rate waveform analyses were carried out in an incomplete CoW, as shown in Figure 5.9. From the results, the pressure almost maintained the same level of the pressure presented in a complete CoW. However, the AcoA and PcoA systolic flow rates for the incomplete CoW are 3.2 and 2.4 times, respectively, larger than those for the complete CoW, as presented in Table 5.4. Compared to the AcoA artery, the flow rate waveform of the PcoA artery for the EVA subject undergoes a longer period of large flow rate because of the early arrival of the backward flow rate component, which may accelerate the development of intravascular stresses. Again, with the endothelial dysfunction of blood vessels, increased stiffness, and the large wall shear stress induced by the hyperperfusion, these two sites in the EVA are vulnerable to develop vascular disease, i.e. aneurysms (Kayembe et al., 1984). Consequently, the cerebral hypertensive pressure and the long-period of increased flow rate occurring in the EVA subject could increase the arterial stresses and therefore increase the risks for vascular disease around the CoW.

Table 5.3 The systolic flow rate in AcoA and PcoA with complete and incomplete CoW, corresponding to missing RA1 and RP1, for the NVA and EVA subjects at 25 and 85 years old.

	Systolic flow rate (ml/s)			
	NVA-25(yr)	NVA-85(yr)	EVA-25(yr)	EVA-85(yr)
AcoA with complete CoW	0.78	0.50	0.69	0.37
PcoA with complete CoW	0.8	0.58	0.73	0.54
AcoA with incomplete CoW	2.48	2.53	2.54	2.60
PcoA with incomplete CoW	1.89	1.94	1.94	2.02

## 5.6 Summary

In this chapter, the 1D model is used to simulate the hemodynamic characteristics of the cardio- and cerebrovascular system for both NVA and EVA systems. The present study has presented the differences seen in human subjects with EVA and NVA by using a validated THINKS model developed to simulate the hemodynamics in the human body. The increased arterial stiffness and early arrived wave reflection from peripheral circulations are key factors for alterations of hemodynamics, especially for the EVA subject. The increased central systolic pressure and AIx give rise to an increased afterload of the left ventricle. Moreover, cerebral hypertension and hyperperfusion for the EVA subject could have clinical effects on the CoW, especially for individuals with an incomplete CoW.

## 6 3D SIMULATIONS OF ANEURYSMS

### 6.1 Overview

In this chapter, a patient-specific anatomic aneurysmal flow was modeled from the 3D reconstruction of the cerebral vessels using DSA imaging. Based on the actual 3D construction of patient's aneurysm, we have created two phantom scenarios to investigate the effects of the aneurysm shape and size on the hemodynamics: (1) increase the size of the aneurysm by approximately two times and (2) create a bilobed aneurysm (dysmorphic) by restricting growth at a particular position over the aneurysm surface (mimic of fibrosis of the aneurysmal wall). The hemodynamic characteristics of the two phantom scenarios will be compared with the anatomic model. The present study aims to evaluate quantitatively; (1) the velocity distribution proximal to, and inside of, the aneurysm, (2) pressure distribution on aneurysm surface, (3) the WSS distribution on the surface of the aneurysmal sacs and (4) the variances of pressure and WSS on the saccular surface. While the influence of WSS and pressure is believed to correlate with the risk management of the aneurysm rupture, the importance of the oscillatory pressure and WSS should not be ignored as the time-dependent pulsating behavior of the blood flow may also cause damage to the aneurysm surface. The ultimate goal of the current study is to assess the forces applied to various aneurysms and attempt to extrapolate these with rupture risks for UIAs using computational simulations of intracranial aneurysm hemodynamics.

### 6.2 Aneurysm topology

The original aneurysm geometry acquired from the patient's clinical images, as shown in Figure 6.1, was then assumed to evolve in different paths leading to two completely different

morphologies, which are considered representative morphologies based on our retrospective review. The initial anatomic model, Figure 6.1 (a), was used to perform the transformations using Sculptor Morph V.3.4 (Optimal Solutions Software, LLC.). The first geometry (enlarged) was created by evenly enlarging the aneurysmal sac by 2.1 times which is a reasonable size for observed enlarged aneurysm, and it reaches the limit of grid deformation under the current meshing method, as shown in Figure 6.1 (b). Compared with the original model, the height from the ostium to the dome was increased to 5.50 mm, the diameter of the ostium was enlarged to 3.89 mm, and the equivalent inner diameter was increased to 5.64 mm. The second model (bi-lobed) was created by restricting the growth on a surrounding curve near the middle position on the sac surface (like tightening the aneurysmal sac in z-direction along the center line), as shown in Figure 6.1 (c). The bi-lobed model was assumed to transform from the original anatomic model unevenly while maintaining the maximum diameter of ostium being the same as the original model. As a result, the height from the ostium to the central lowest position of the concave region was reduced to 2.70 mm.

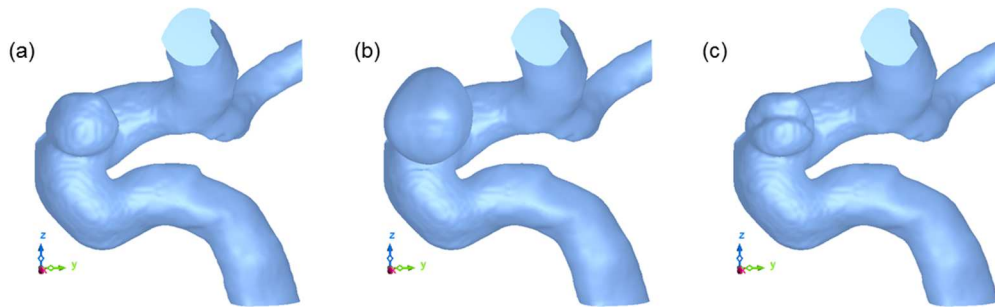


Figure 6.1 Anatomic model (a) and two morphology models: (b) evenly enlarged model; (c) bi-lobed model.



## 6.3 Computational fluid dynamics

### 6.3.1 Analysis conditions

The models can be directly loaded into the commercial CFD software SC/Tetra (Cradle North America, Dayton, OH). Blood flows were assumed as incompressible and Newtonian fluid. The computational solver employs the finite volume method to compute the governing continuity and momentum equations:

$$\nabla \cdot \mathbf{u} = 0 \quad (6.1)$$

$$\frac{\partial \mathbf{u}}{\partial t} + (\mathbf{u} \cdot \nabla) \mathbf{u} = -\frac{1}{\rho} \nabla P + \nu \nabla^2 \mathbf{u} \quad (6.2)$$

where  $\mathbf{u}$  is the flow velocity in x, y, and z directions,  $t$  is time,  $\rho$  is the density of blood,  $P$  is blood pressure, and  $\nu$  is the kinematic viscosity of blood.

In the CFD simulation, hexahedral grids were generated around the blood vessel wall as prism layers to capture the velocity boundary layer. In this case, ten prism layer were inserted with the increasign ratio of 1.2 and the thickness of the first prism layer of  $1 \times 10^{-5}$ . Tetrahedral grids were distributed on the arterial lumen and aneurysm cavity generated by local mesh refinement technique, as shown in Figure 6.4. The convective flux terms are computed using the second-order accurate MUSCL scheme, and time derivative is used first-order implicit scheme. In the meantime, the pressure correction method employs the SIMPLEC method.

As we assume the effect of vessel deformation is small, a rigid wall with no-slip boundary condition was applied to the wall surfaces. The flow was modeled as a laminar and incompressible flow, and the blood was modeled as Newtonian fluid with a density of  $\rho = 1050 \text{ kg/m}^3$  and a dynamic viscosity of  $\mu = 4.5 \times 10^{-3} \text{ Pa} \cdot \text{s}$ , which is in accordance with previous studies (Liang et al., 2009 and Berg et al., 2014). The *in-vivo* measurement of the

time-averaged blood flow rate in ICA is approximately 266 ml/min and, ICA diameter is around 0.5cm. This translates into a mean Reynolds number ( $Re = \frac{\rho V D}{\mu}$ , where  $V$  is the averaged velocity in ICA, and  $D$  is the diameter of the vessel). Even if we consider the waveform as shown Figure 6.2, the maximum Reynolds number is 816.

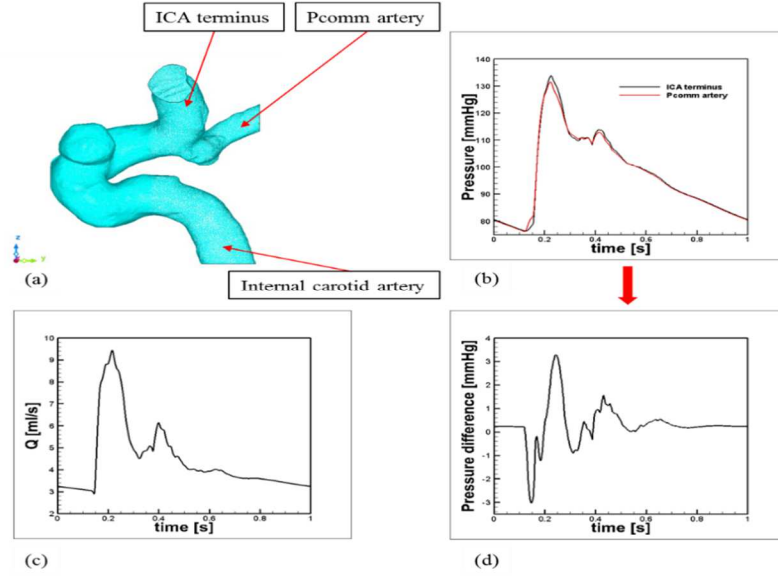


Figure 6.2 Inlet boundary condition for the simulation, a. anatomic modeling; b. comparison of the pressure waveform for ICA terminus and PcoA; c. volume flow rate for ICA inlet; d. blood pressure waveform.

The boundary conditions of the flow rate and pressure waveforms were directly extracted from the 1D model corresponding to the artery locations of the 3D model, as shown in Figure 6.2. At two distal exits, ICA terminus and PcoA, the pressure difference was applied to the ICA terminus as shown in Figure 3.10 (d), and a zero-value gage pressure was applied to the PcoA. The time-dependent values of the pressure at the center of the aneurysm's ostium, as shown in Figure 6.3 (a), were presented in Figures 6.3 (b). As can be observed from the plots, a quasi-steady state solution has been reached, and therefore all 3D CFD analyses performed in this dissertation were used the solution obtained in the fifth cardiac cycle.

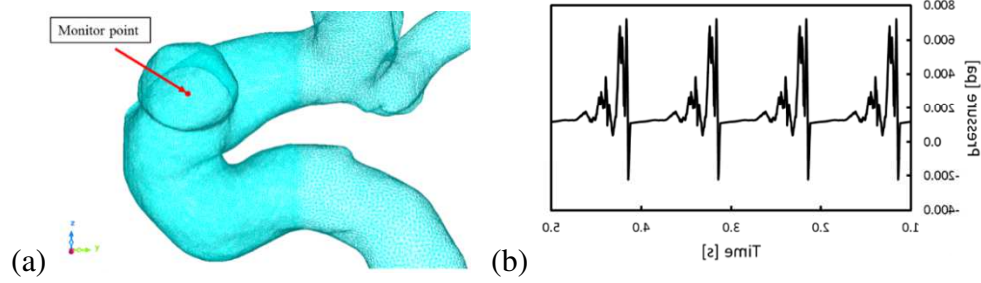


Figure 6.3 Monitor point position and the pressure and velocity profile from the second period to the fifth period.

### 6.3.2 Mesh independent study

The computational mesh sensitivity study was implemented to verify the grid convergence of the solver. Three difference meshes were created with the grid numbers of 2,521,128; 9,568,766, and 17,441,917, respectively. It should be noted that the refinement of the computational grids was mainly concentrated on the aneurysm region because the mesh quality takes less effects on the prediction of the hemodynamics of the regions far away from the aneurysm sac, as shown in Figure 6.4.



Figure 6.4 Computational meshes. (a) is coarse mesh; (b) is middle mesh; (c) is fine mesh.

Time-averaged pressure and WSS distributions over the aneurysm surface were compared among simulations, as presented in Figure 6.5. As can be seen from the results, minor visual differences of the pressure and WSS among the simulations can be observed on the top surface of the sac and the neck regions, respectively. Quantitatively, Table 6.1 presented the simulation running time and differences of pressure and WSS in different meshes. It is indicated that the maximum numerical error of the time-averaged pressure and WSS between

the middle and fine meshes are less than 0.21% and 0.36%, respectively. In order to save the computational time, the middle mesh was chosen to conduct the simulations for the rest simulations in this study.

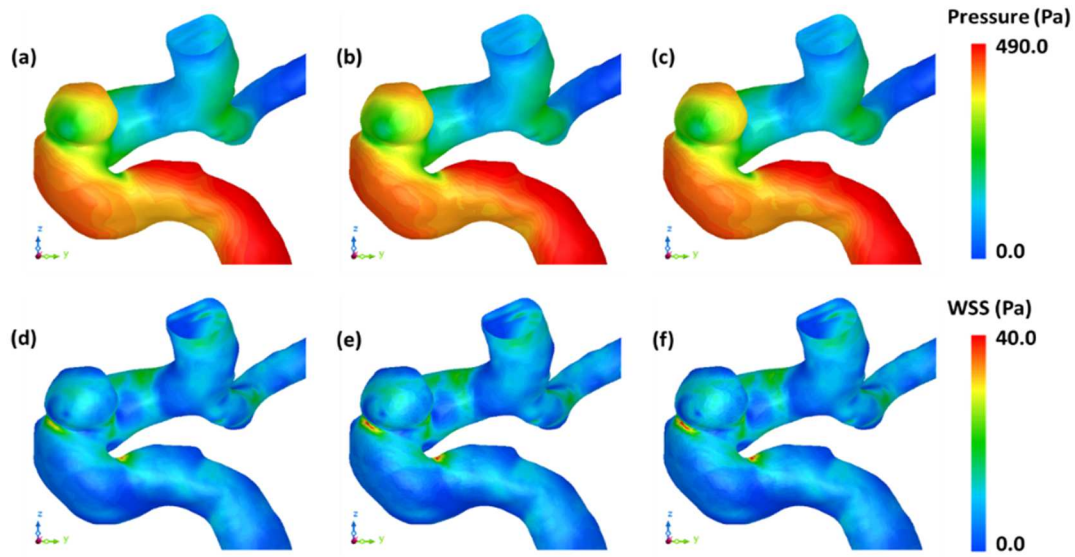


Figure 6.5 Time-averaged pressure (top) and WSS (bottom) distributions over the aneurysm surface: (a) and (d): the coarse mesh; (b) and (e): the middle mesh; and WSS distribution: (c) and (f): the fine mesh.

Table 6.1 The comparison of simulation times, pressure difference, and WSS difference among different meshes.

Mesh	Elements	Running time	Running cycles	Processors	Pressure Difference	WSS Difference
Coarse	2,521,128	4h:53m	5	160	+1.28%	+3.51%
Middle	9,568,766	9h:22m			-0.21%	-0.36%
Fine	17,441,917	37h:27m				

The assumption of the Newtonian fluid was tested by presenting the shear rate distributions over the aneurysm surface, as shown in Figure 6.6. In this figure, gray color represents the shear rate distributions larger than 100/s. The Non-Newtonian fluid takes significant effects on WSS when the shear rate is less than 100/s. As can be seen from the figure, small shear

rate regions can be observed at the bottom of the parent artery from the current perspective, and other small regions can be found near the exit of the ICA\_T. Therefore, the assumption of the Newtonian fluid is acceptable for the current aneurysm model.

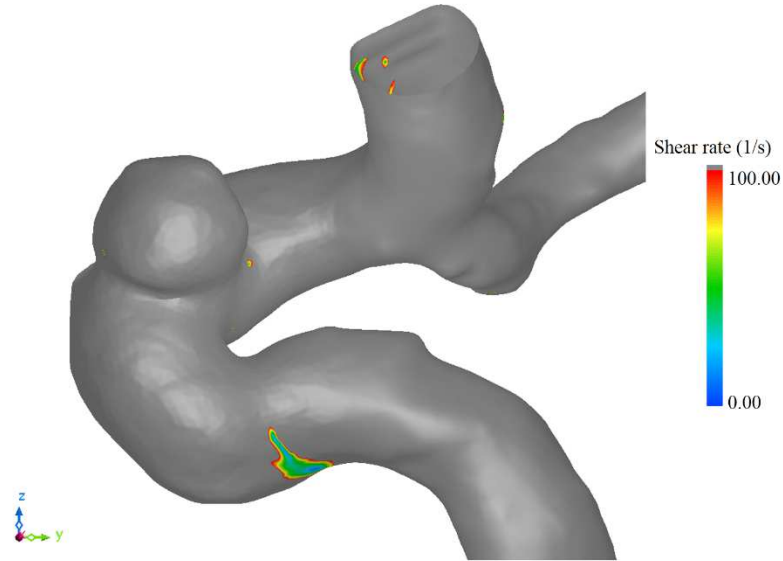


Figure 6.6 Time-averaged shear rate distributions over the aneurysm surface.

#### 6.4 Time-averaged flow patterns

Time-averaged analysis, which was based on 5,000 instantaneous data files in the fifth cycle, was performed for the three cases. The blood flow patterns inside the aneurysmal sac were compared in Figure 6.6. Complex vortex-like flows were observed inside the aneurysms for all three cases. Three represented streamlines were displayed for purposes of illustration. The black line indicates the fraction of the flow bypassing the aneurysm while the red and blue lines show the fraction of the blood entering into the aneurysmal sac. For the original anatomic aneurysm, the bloodstream enters the aneurysm from the ostium and moves along the back left wall of the sac from the current view of the aneurysm as shown in Figure 6.7 (a). Then, after the bloodstream reaches the dome, a quantity of bloodstream keeps flowing along the right side wall and moving out, whereas a large amount of bloodstream turns down along

the front surface resulting in vortices about the center of the aneurysmal sac and then moves out of the aneurysm resulting in a spiral line path.

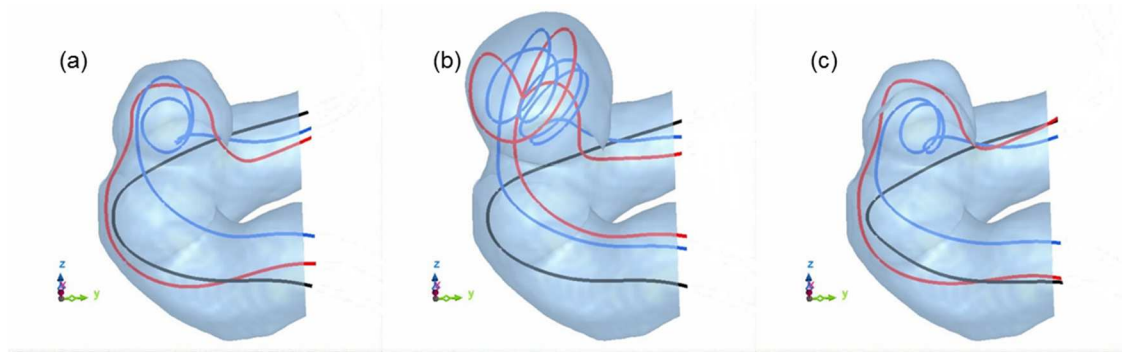


Figure 6.7 Time-averaged streamlines: (a), the anatomic case; (b), the enlarged case; (c), the bi-lobed case.

Dissimilar to the anatomic case, the enlarged model generates a more complicated flow pattern inside the aneurysmal sac, as shown in Figure 6.7 (b). There is no bloodstream directly leaving the aneurysmal sac after reaching the dome. All flow turns down along the front surface generating large-scale, central, vortices which make the blood residence time longer. This results in an evenly low-velocity distribution inside. The phenomenon can also be explained by linking with mass flow rate entering the aneurysm, which will be presented in the following. As performed in Figure 6.7 (c), the flow pattern of the bi-lobed case is similar to the anatomic model. Since the geometry has been changed, the dome of the aneurysm is now lower than the anatomic case so that the vortex is remained at a lower position compared to Figure 6.7 (a). Thus, the blood residence time is shorter than the anatomic case.

Figure 6.8 shows the time-averaged velocity contour and 2-D vector on the cross-section of the ostium as shown in Figure 6.8 (a). In order to illuminate the mass flow rate going into/out of the aneurysm, the velocity component normal to the cross section is used to compute the mass flow rate. As Figure 6.8 (b), (c), and (d) presented, local high positive and negative out-

of-plane velocities are observed in the anatomic and bi-lobed cases, which indicates more friction can be generated on the ostium region. The anatomic case has the largest mass flow rate (34.12%) out of the three cases, while the enlarged case has the lowest flow rate (23.78%). Therefore, under the same flow condition in the vessel, the increase of the aneurysmal sac volume gives rise to the decrease in velocity inside, which results in a lower WSS distribution on the surface of the sac. In order to illuminate the details inside of the aneurysmal sac, several cut-planes with in-plane velocity vectors and out-of-plane velocity contours have been added, as shown in Figures 6.9, 6.10 and 6.11. The distance in-between the cut-planes is about 1.6 mm. Again, the bloodstream entering into the aneurysm is mainly from the left side, near the front surface from the present perspective, and moves out from the right side near the front surface. The high-speed inflow and outflow around these two locations respectively could induce the local high WSS.

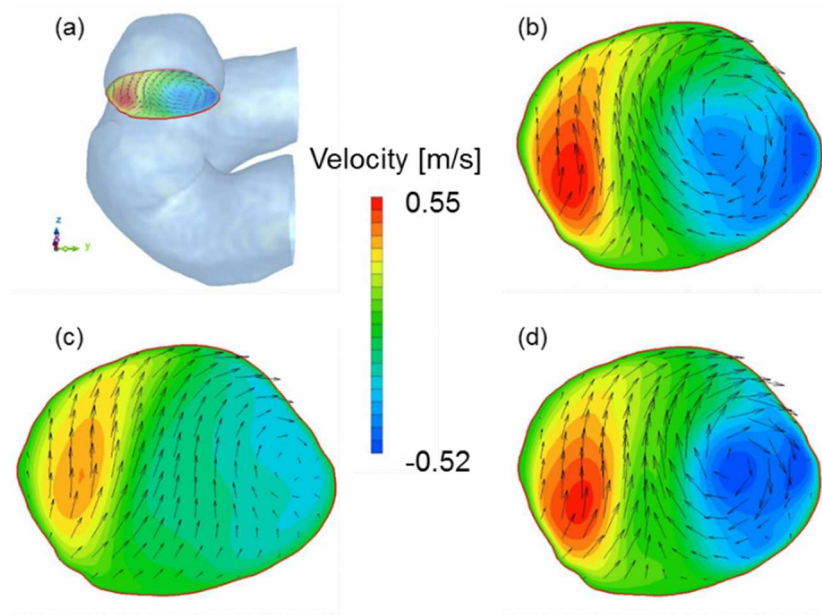


Figure 6.8 Time-averaged out-of-plane velocity contour with 2-D vectors on the surface of the inlet of the aneurysm: (a), the surface of the inlet of the aneurysm; (b), the anatomic case; (c), the enlarged case; (d), the bi-lobed case. Note that the range of the length of the velocity vector is from 0 to 0.38



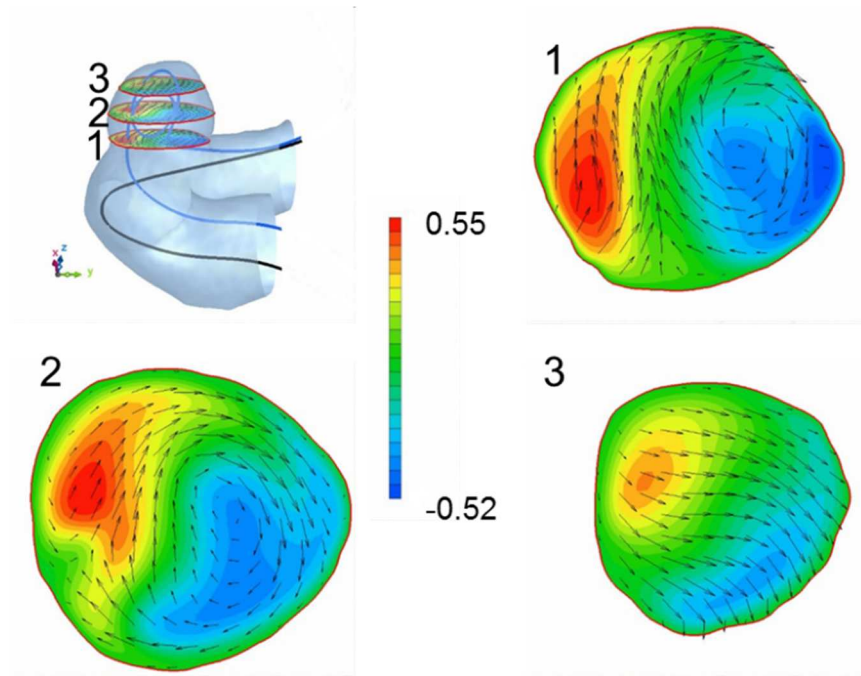


Figure 6.9 Time-averaged out-of-plane velocity contour with in-plane velocity vectors on several cross-sections in the aneurysm with streamlines for the anatomic case

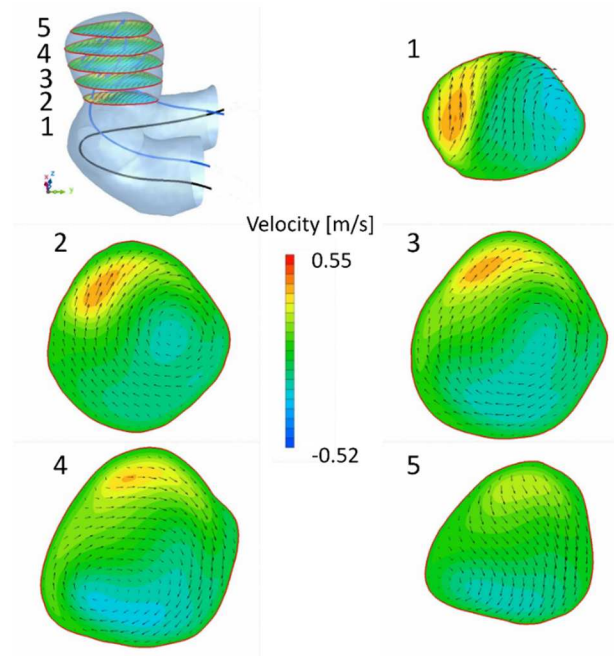


Figure 6.10 Time-averaged out-of-plane velocity contour with in-plane velocity vectors on several cross sections in the aneurysm with streamlines for the evenly enlarged case.



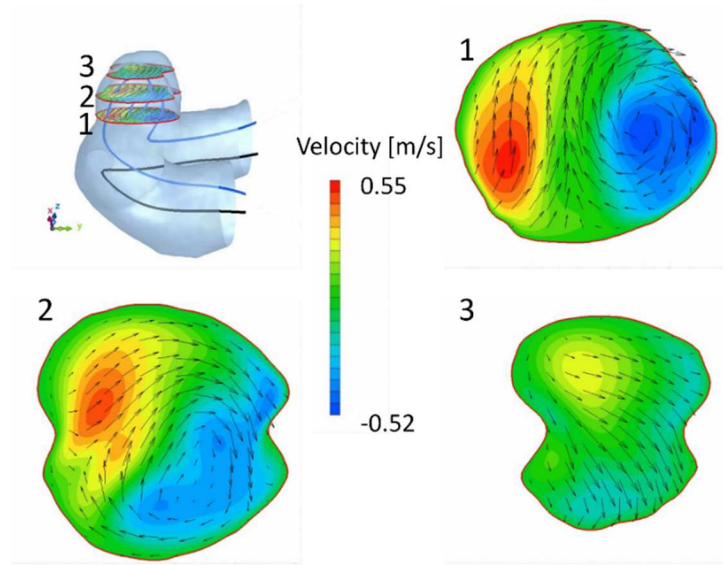


Figure 6.11 Time-averaged out-of-plane velocity contour with in-plane velocity vectors on several cross sections in the aneurysm with streamlines for the bi-lobed case.

## 6.5 Pressure and WSS distributions

Based on the time-averaged CFD simulation for the three models, pressure, WSS and their corresponding oscillatory components were extracted and mapped on the surface of the internal carotid aneurysm as shown in Figure 6.12, 6.13, 6.14, and 6.15 respectively.

The time-averaged pressure contours on the surface of the aneurysmal sac were presented in Figure 6.12, with Figure 6.12 (a) showing the perspective view of the aneurysm. As shown in Figure 6.12 (b), the maximum pressure of 415.38 pa on the anatomic model appears at the dome region in relation with the impingement, and the minimum pressure 157.62 Pa is located on the left-hand side corresponding to the high-speed passing flow. Figure 6.12 (c) shows the pressure contour of the enlarged phantom morphology, the range of pressure is from 231.84 to 399.58 Pa. It has been observed that the range is dramatically narrowed compared to the anatomic model and thus the pressure is more uniformly distributed. The pressure contour for the bi-lobed phantom morphology is shown in Figure 6.12 (d). The

range of pressures is from 158.84 to 461.00 Pa and a wider high pressure region is mainly concentrated in the concave region as compared to the original anatomic case.

Attention is now focused on the comparison of the WSS, as shown in Figure 6.13. For the original anatomic case, as shown in Figure 6.13 (a), the maximum WSS of 39.05 pa was observed at the aneurysm neck region as predicted in the previous analysis on the left-hand side. On the sac surface, a maximum WSS of 17.61 Pa was observed in several places in the dome area. In contrast, WSS for the enlarged and bi-lobed cases are shown in Figure 6.13 (b) and (c), respectively. The distribution of WSS for the enlarged case becomes more uniform on the aneurysmal sac surface and it has a smaller magnitude (the maximum WSS is 9.81 Pa on the sac surface), which agrees with the previous analysis based on the flow characteristics. For the bi-lobed case, in addition to the regions close to the aneurysm neck, high WSS was also observed close to the aneurysm neck and the concave region on the dome, which also agrees with the previous estimation based on the flow characteristics. In this case, due to the irregularity of the aneurysm, there exists a region of high WSS near the concave region, having a maximum WSS of 33.20 Pa.

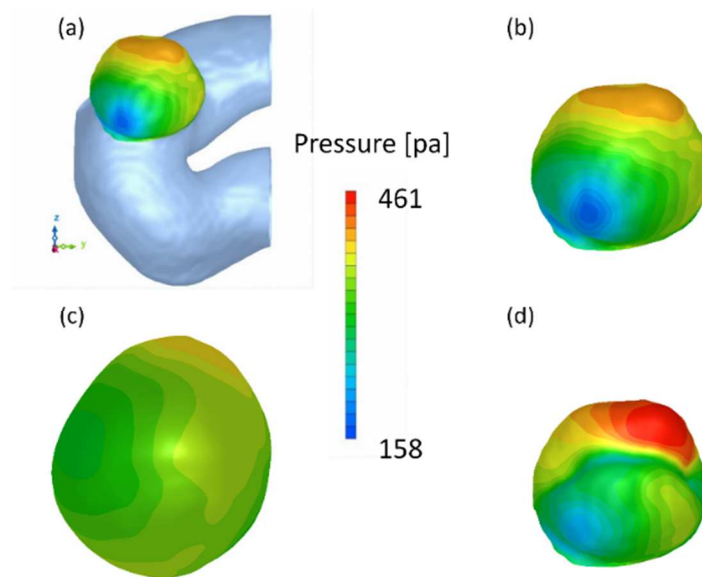


Figure 6.12 Time-averaged pressure distributions: (a), the perspective view of the aneurysm; (b), the anatomic case; (c), the enlarged case; (d), the bi-lobed case.

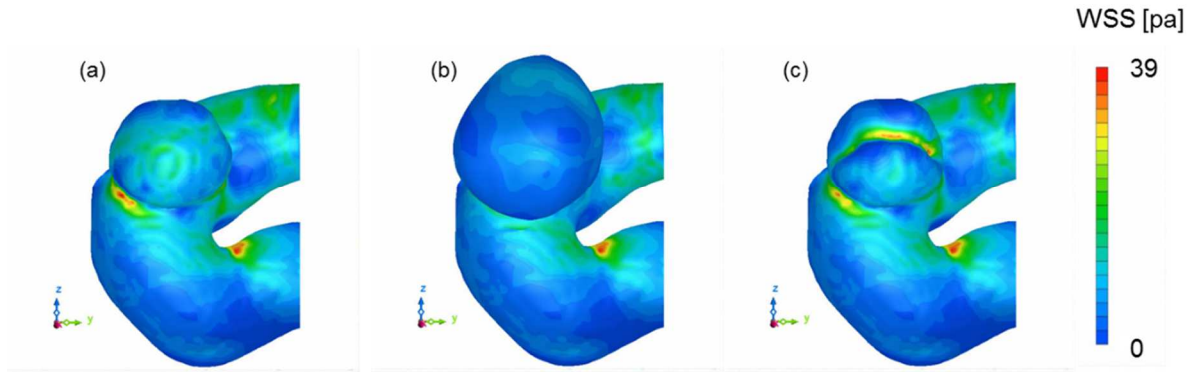


Figure 6.13 Time-averaged WSS distributions: (a), the anatomic case; (b), the enlarged case; (c), the bi-lobed case.

The contours of the RMS of WSS are shown in Figure 6.13 and 6.14. It can be seen that the RMS of pressure and WSS is around 30.9% and 62.5% of the mean, and the contour distributions are similar to those of the mean pressure and WSS. The high RMS value indicates that WSS is subject to a substantial oscillation due to the unsteady nature of the cardiac blood flow. The similarity in contours of the mean WSS and the RMS value implies that the region of the impact caused by the unsteady nature is essentially in accordance with the area where large mean WSS is observed.

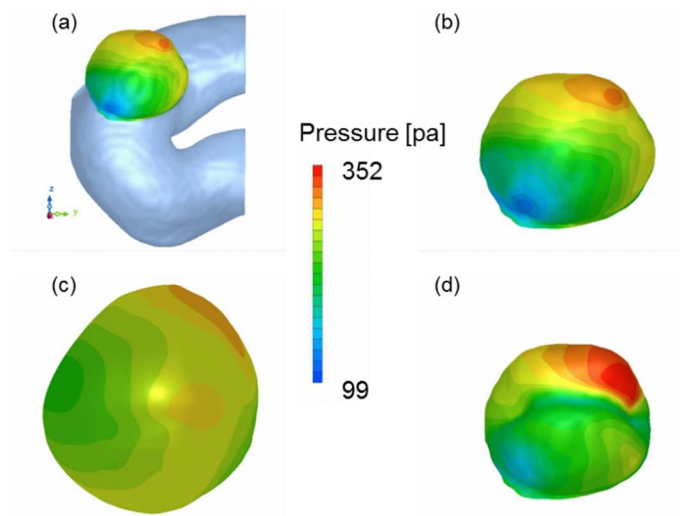


Figure 6.14 The RMS of Pressure distributions: (a). The anatomic case; (b). The enlarged case; (c). The bi-lobed case.

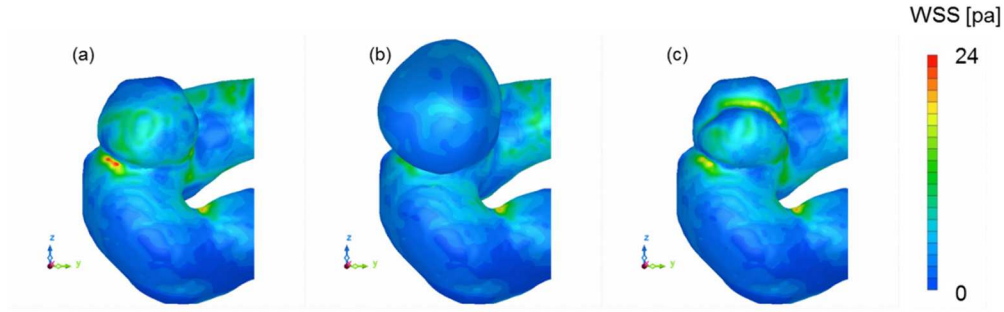


Figure 6.15 The variance of WSS distributions: (a). The anatomic case; (b). The enlarged case; (c). The bi-lobed case.

## 6.6 Discussion

CFD studies in the current chapter have assumed the same heart rate and blood pressure, which represents a snapshot of the varying physiological conditions. However, by eliminating the effect of heart rate and pressure, it presents a purer influence of the morphology of the bleb aneurysm on the flow pattern, pressure, and WSS distributions. The 3D patient-specific unruptured intracranial aneurysm was successfully reconstructed and modeled for the CFD simulation. The saccular sidewall IA in the present study belongs to the small bleb aneurysm phenotypes based on the classification in the previous study by Meng et al., (2014). The arterial flow characteristics are illustrated in terms of velocity vectors and streamlines. High velocity streams entered the aneurysm sac from the left back side and became complex vortices. The high and unsteady pressure and friction on the arterial wall could induce a mural-cell-mediated pathway. It has been indicated that pressure elicits tensile stresses in the wall, which are felt by vascular mural cells, namely smooth muscle cells and fibroblasts (Meng et al., 2014). Under unbalanced stresses, these mural cells can regulate collagen dynamics by cross-linking and synthesizing new collagen and degrading old collagen. Meanwhile, endothelial cells lining the vessel lumen sense changes in WSS from

blood flow and transduce these mechanical signals into biologic signals, activating pathways to maintain vascular homeostasis. Through endothelial cell-mediated biology, WSS not only regulates vascular tone but also drives vascular remodeling under sustained deviations from physiologic baselines (Humphrey et al., 2008; Nixon et al., 2010; Metaxa et al., 2010; Kolega et al., 2011).

In the bi-lobed phantom morphology, the increased WSS observed on the sac surface associated with a higher flow velocity gradient and increased pressure could accelerate the process of the artery wall degeneration and weaken in response to changing hemodynamic loading and biomechanic stressors (Cebral et al., 2013). This situation is aggravated by the large unsteady nature of blood flow. The computational results showed that the oscillation of WSS essentially coincides with high averaged WSS. The changes in the aneurysmal wall properties could induce intensive strain especially near the margin between the stiff region and normal region, and cause an aneurysm to grow unevenly. The uneven feature of an aneurysm and high WSS are mutually caused and intensified. This trend could theoretically lead to the rupture of an aneurysm.

In the evenly enlarged phantom morphology, the decreased pressure and WSS on the sac surface are considered favorable for maintaining vascular homeostasis. However, this is based on the hypothesis that the aneurysm is a thin-walled, smooth, hypocellular aneurysm phenotype. If it is a large, thick-walled, atherosclerotic aneurysm phenotype, the low WSS and high oscillatory shear could trigger an inflammatory-cell-mediated pathway, which could be associated with the growth and rupture of this type of the aneurysm (Cebral et al., 2005; Malek et al., 1999). Such findings highlight aneurysm hemodynamics, in conjunction with

the better classification of aneurysms, could help determine the rupture of cerebral aneurysms.

The major limitation is the assumption of rigid wall boundary conditions due to the lack of information of arterial wall properties such as elasticity and thickness, especially for deformed vessel segments. However, by assuming a linear-elastic material of the arterial structure, the fluid-structure interaction simulation can be conducted and provide possible insights of the influence of the damping of the vessel wall on the pressure propagation and WSS distributions. Torii et al., (2010) indicated that fluid–structure interaction might become important when simulating the aneurysm models with thinner wall, such as bifurcation or giant aneurysms. Nevertheless, this approach would considerably increase the computational cost. To trade-off between the accuracy and the cost, the rigid wall condition of the vessel was assumed.

The averaged intra-arterial mass flow rate waveform is based on a total human intravascular network simulation. However, the unsteady physiological conditions such as the change of heart rate and blood pressure were not taken into account in the present study. However, it is difficult to measure the precise waveform of a patient, because of different heart beats, total length of blood vessel, and the blood vessel structure. Based on this information, more accurate inlet boundary conditions and more precise fluid-structure interactions will be taken into account in our future studies.

## 6.7 Summary

An anatomic unruptured aneurysm on the internal carotid artery and two phantom morphology models under the same inlet flow waveform were analyzed using CFD. The aim of this chapter is to propose the aneurysm sac independent study with comparing the shape

and size of the aneurysm. The simulation results demonstrate that the complex shape of an aneurysm can cause an increase in the pressure and WSS distributions over the aneurysm surface, whereas the enlarged aneurysm leads a decrease in these parameters. Unfortunately, the impact of the shape and size of aneurysm on the risk factors of the rupture of an aneurysm cannot be concluded based on the current findings. The current study is only focusing on one patient-specific aneurysm model and two manipulated aneurysm geometries, and therefore the simulation results are not representative. Thus, further statistical studies are required for a large number of aneurysm models to validate the current findings. In this chapter, the 3D simulation on cerebral aneurysm was successfully developed, and the effects of the shape and size of the aneurysm sac on the local hemodynamics have been investigated. Therefore, the current CFD simulation technique can be used to couple with the 1D numerical model to investigate the effects of a local morphology on the global flow conditions.

## **7 MULTI-SCALE SIMULATIONS FOR CEREBRAL BLOOD FLOW WITH ANEURYSMS AND/OR STENOSES**

### **7.1 Overview**

A complete 3D model of the entire vascular system is preferred, but the high computational cost and the difficulty in reconstructing a full 3D model refrain us from performing such a calculation. Xiao et al., (2013) presented a full-body 3D arterial network computation. On the other hand, a multi-scale approach coupling the entire 1D vascular network and a 3D detailed patient-specific vascular segment can take into account the interactions between global and local hemodynamics. The 3D model in the coupling method is simulated by solving Navier-Stokes equations, either by an in-house computer program or a commercial CFD software (Soudah et al., 2014; Passerini et al., 2009; Papadakis 2009; and Liang et al., 2015, Formaggia et al.; 2001; Nobile 2009; Blanco et al., 2010, and Blanco et al., 2013). The connections between 1D and 3D models adopt 0D models as the interface to transmit flow and pressure information.

In this chapter, the current multi-scale model is validated against three simplified test cases: one with a straight stenotic artery and the other two for vessel bifurcations with different stenotic area ratios. In section 7.3, the proposed multi-scale model is used to simulate the hemodynamics of two 3D morphological segments: one with cerebral aneurysm and the other with stenosis. This study demonstrates how the flow conditions can be altered by vessel deformation caused by the associated vascular disease.



## 7.2 Validation studies of the multi-scale model

Validation studies were implemented using three complete 3D models, as shown in Figure 7.1 (a), (c), and (e), responding to Case I, II and III, respectively. The multi-scale models were modified from the 3D models by retaining the 3D sections highlighted by the blue boxes, and replacing the rest of the sections by the 1D model, as shown in Figure 7.1 (b), (d), and (f).

The first test case, shown as case I of Figure 7.1, was a straight stenotic artery model adopted from a previous study by Banerjee et al., (2008), with 65% occlusion in the cross-sectional area. The inflow boundary condition was applied based on a time-dependent laminar velocity given by Banerjee et al., (2008). The test cases II and III as shown in Figure 7.1 (c) and (e) are vessel bifurcation models with two different stenotic area ratios in one of the daughter branches, respectively. The purpose of these two designs is to capture the flow rate alterations in the two daughter branches because the stenosis could increase the pressure resistance and cause the flow rate of the daughter branch with stenosis to decrease while the other branch to increase. The area ratios of the stenosis are  $6/40$  and  $1/40$  for the cases II and III, respectively. The stenosis shape for case II was designed to change gradually whereas a sudden drop in the cross-sectional area was used in case III. The latter case increases the influence of the backward wave component and causes a large pressure loss across the stenosis. The inflow waveform was adopted from literature (Xiao et al., 2014 and Boileau et al., 2015), and a fixed static pressure condition was applied to both ends of the daughter branches.

Figure 7.2 shows comparisons of the mean pressure drop along the centerline of the artery for the multi-scale model and the complete 3D model. Experimental data and previous CFD

results were also shown for comparisons. As can be seen, the result obtained from the current complete 3D model is much closer to the experimental data than that of the previous CFD simulation and the multi-scale model can capture the pressure drop along the stenosis.

Figure 7.3 shows comparisons of pressure difference of the stenosis and flow rate waveforms at the two daughter branches for case II. As can be seen from the Figure, the pure 1D model was not able to capture the mean flow waveform at the exits of the branches and under-predict the pressure gradient across the stenosis (between positions A and B). On the other hand, the flow rate waveforms in two daughter branches can be reproduced by the multi-scale model similar to the 3D mode. The pressure-gradient waveform between positions A and B computed by the multi-scale model is also in good agreement with the 3D model.

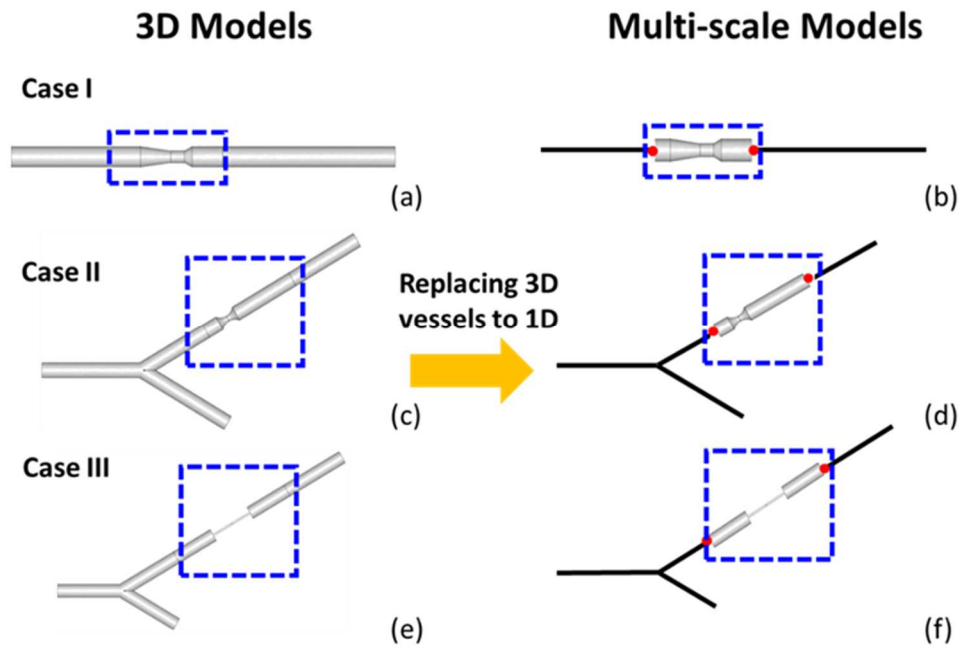


Figure 7.1 The geometries of the three test cases. The case I is stenotic artery; Case II and II are bifurcation models with different area ratios.

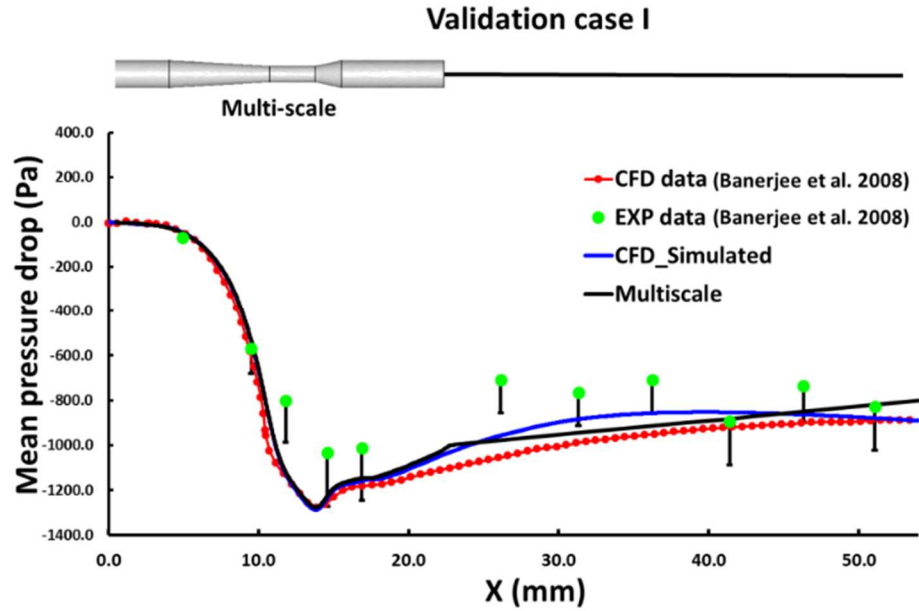


Figure 7.2 the mean pressure drop comparison of the multi-scale model with the 3D model and previous CFD simulation and experimental data by Banerjee et al., (2008).

Figure 7.4 shows comparisons of pressure difference across the stenotic arteries (between positions A and B) and flow rate waveforms of two daughter branches for case III. As can be seen from the Figure, severe pressure oscillations were observed in all model because of the interaction of the flow against the reflection wave caused by the sudden expansion. The pressure difference obtained from the multi-scale model is closer to the 3D model as compared to the pure 1D model. Similarly, the multi-scale model is able to provide more accurate flow distributions in the two branches than the 1D model.

Validation studies were implemented through three simplified geometries including single and multiple artery networks to evaluate the accuracy of the proposed multi-scale model by comparing the pressure and flow rate waveforms with previous experimental data and complete 3D models. The simulated results demonstrate that the multi-scale model is capable of capturing the pressure drop along the centerline and the flow rate and pressure waveforms due to the featured shape of a local morphology as compared with previous experimental and

complete 3D CFD results, as presented in Figure 7.2, 7.3, and 7.4. On the contrary, the 1D model was not able to predict the comprehensive feature of the pressure and flow rate because of the over simplified parameters. The multi-scale model merely adding the local 3D morphology enables the feature to display in the pressure and flow rate waveforms. As compared to solving complete 3D models, the multi-scale model could save considerable computational effort.

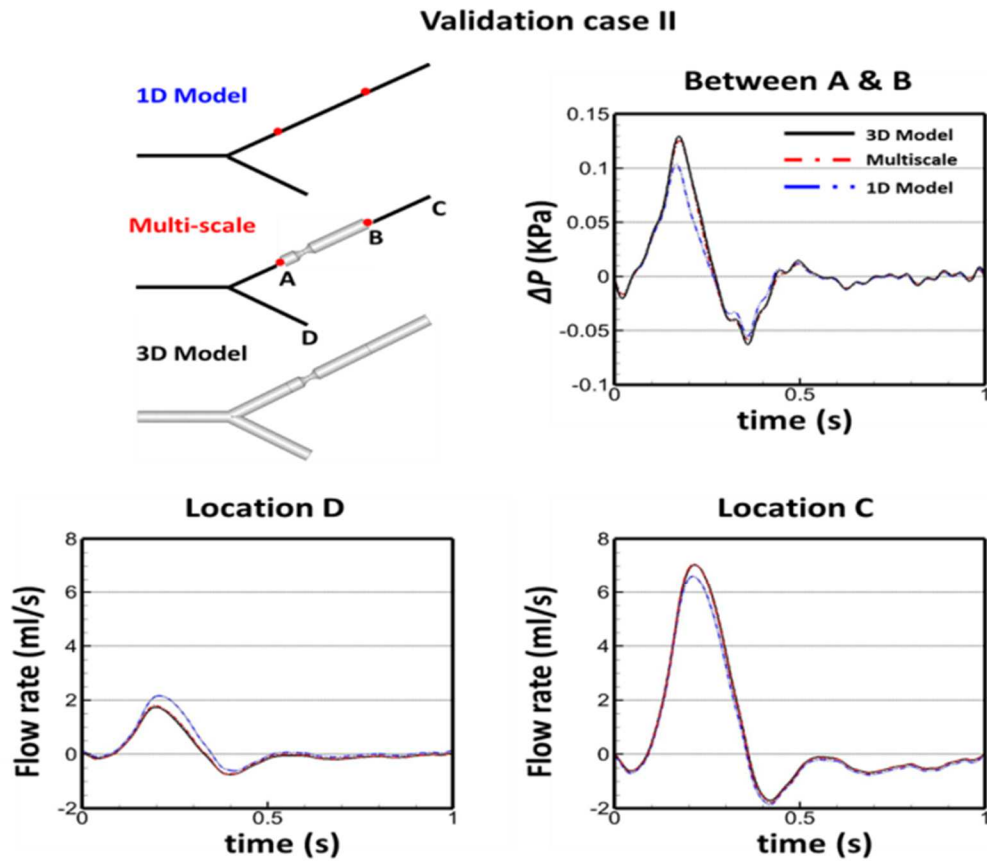


Figure 7.3 Pressure and flow rate waveform comparisons among the 1D, multiscale, and 3D models. Location A & B, the pressure difference between locations A and B; Location B and C, the flow rate waveforms comparison.

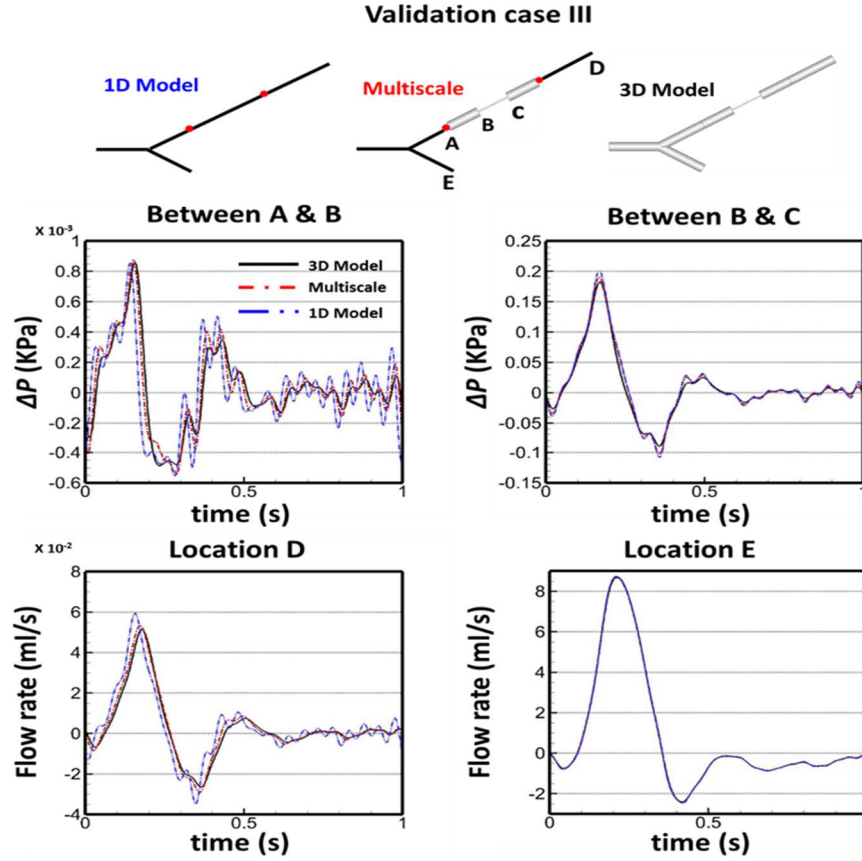


Figure 7.4 Pressure and flow rate waveform comparisons among the 1D, multiscale, and 3D models. Location A & B, the pressure difference between locations A and B; Location B and C, the flow rate waveforms comparison.

### 7.3 Application of the multi-scale model for patient-specific segments

#### 7.3.1 Setup of the patient-specific models

The first application case was a 3D LICA aneurysm model, which was constructed using 500 slices of MRA imaging data obtained from Miami Valley Hospital (Premier Health) in Dayton, OH (Yang et al. 2015). After generating the 3D geometry, numerous cracked elements and disconnected vessels were found. Thus, geometry cleaning was necessary, including noise elements removal and repairs of vessels missing connections. The 3D configuration of the aneurysm model was shown in the application I of Figure 7.5. The second case was an LCCA bifurcation model which was obtained and modified from

Grabcad (GrabCad). Modifications include extending the inlet and exits and creating the stenosis region with 80% stenotic appeared on the LICA branch, as shown by the 3D model in application II in Figure 7.5.

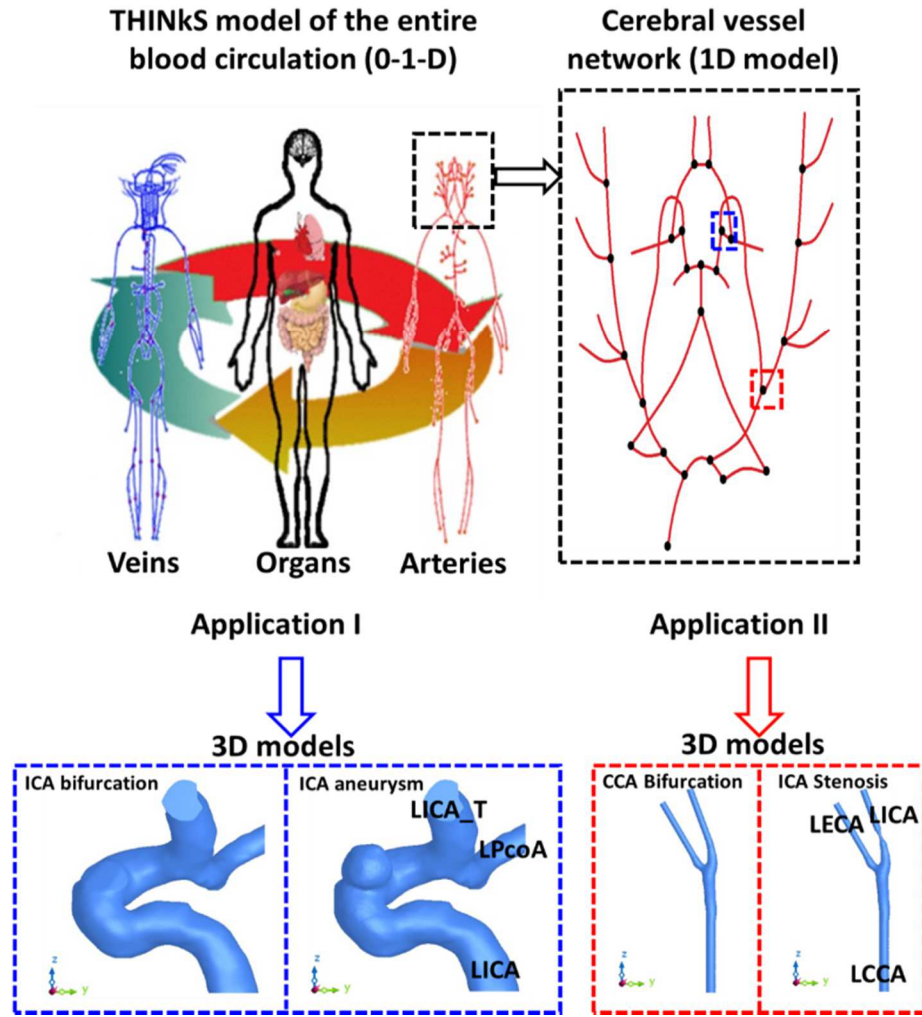


Figure 7.5 The description of applications of the multi-scale model, where a 3D aneurysm segment and a CCA bifurcation model are coupled with a 1D model of the entire cardiovascular system. LICA: left internal carotid artery; LPcoA: left posterior communicating artery; LICA\_T: left internal carotid artery terminal; LCCA: left common carotid artery; LECA: left external carotid artery.

In most CFD simulations, the boundary conditions of the flow and pressure waveforms were adopted from either the measurement of a healthy subject or the 1D network model (Yang et al., 2015; Xiang et al., 2014; and Liang et al., 2016). In the current study, patient-specific segments were solved using the multi-scale model and coupled with the entire human

intracranial vessel network (Huang et al., 2015 and Yu et al., 2016). This study aims to explore the hemodynamic changes in the vascular system induced by the featured vascular morphologies such as aneurysm sac or stenosis. In order to achieve this goal, baseline 3D models were created by removing the aneurysm sac or eliminating the stenosis, as shown in the application I and II in Figure 7.5. The multi-scale model was first used to compute the baseline models for the purpose of comparison. In order to ensure flow balance of the human network, the 3D zonal model was applied on both left and right sides of the flow vessel network. After solving the baseline models, the aneurysm sac or stenosis was only placed on the left ICA while the right ICA remains as the original healthy model. The models of the aneurysm sac or stenosis are called anomalous models in this chapter. The solution of the anomalous model can be compared with that of the baseline model to provide an investigation of the effects of local pathological morphology.

### 7.3.2 Computational results

Figure 7.6 depicts pressure and flow rate waveform comparisons at both the inlet and two downstream exits. In the Figure, solutions for the baseline and anomalous models were represented by the blue and red lines, respectively. As can be seen from the results, the overall difference of the pressure gradient between the baseline and multi-scale models is less than 1%. This change of pressure gradient in the LICA aneurysm model leads to a 2.40%, 4.71%, and 34.94% decrease in flow rate distributions in ICA, ICAT, and PcoA, respectively, as compared to the solutions of the baseline model.

The time-averaged velocity path-lines and pressure distributions over the aneurysm surface are shown in Figure 7.7. In addition, WSS and OSI are also presented. As can be observed, the maximum gauge pressure of 428.1 Pa appears at the top of the dome region, which is

caused by the impingement of the flow from the aneurysm orifice. On the other hand, the minimum gauge pressure of 214.4 Pa is located on the left-hand corner of the dome represented by the green contour plot. This low-pressure region is caused by the high-speed flow passing from the orifice (Yang et al., 2015). The maximum WSS was observed at the aneurysm neck region and the WSS at the surface of the aneurysm is relatively small with values ranging from 1 to 12 Pa. High OSI distributions were observed in regions where the large vessels having high curvature, aneurysm sac, and the downstream bifurcation regions, where flow separations occur when blood moves through those regions. The velocity path-lines are also shown in Figure 7.7. After the flow moving into the aneurysm and reaching the top of the dome, the blood flow curves downward and gradually exits the aneurysm with a spiral motion. This flow pattern gives rise to a mean blood inflow rate of 2.41 ml/s entering and leaving the aneurysm.



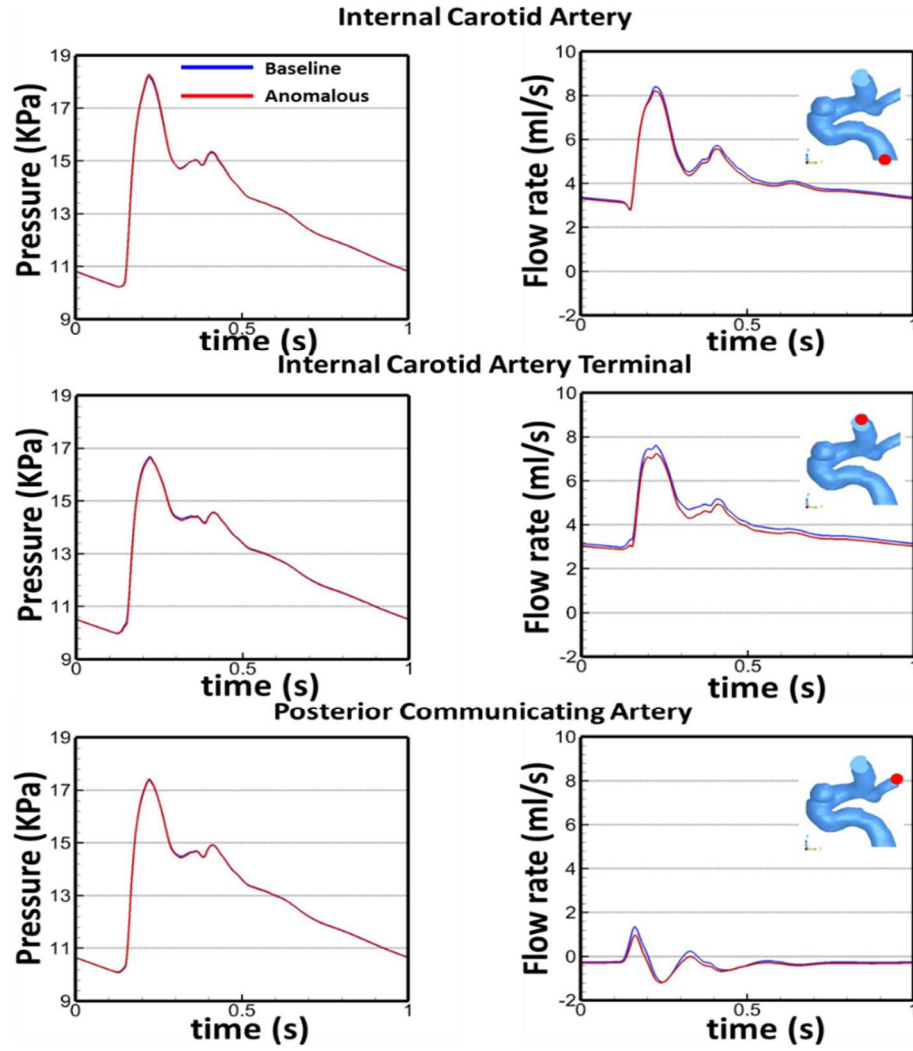


Figure 7.6 The pressure and flow rate waveforms comparisons of the multi-scale model with the baseline model at the ICA upstream and ICA\_T and PcoA downstream as red dots represent.

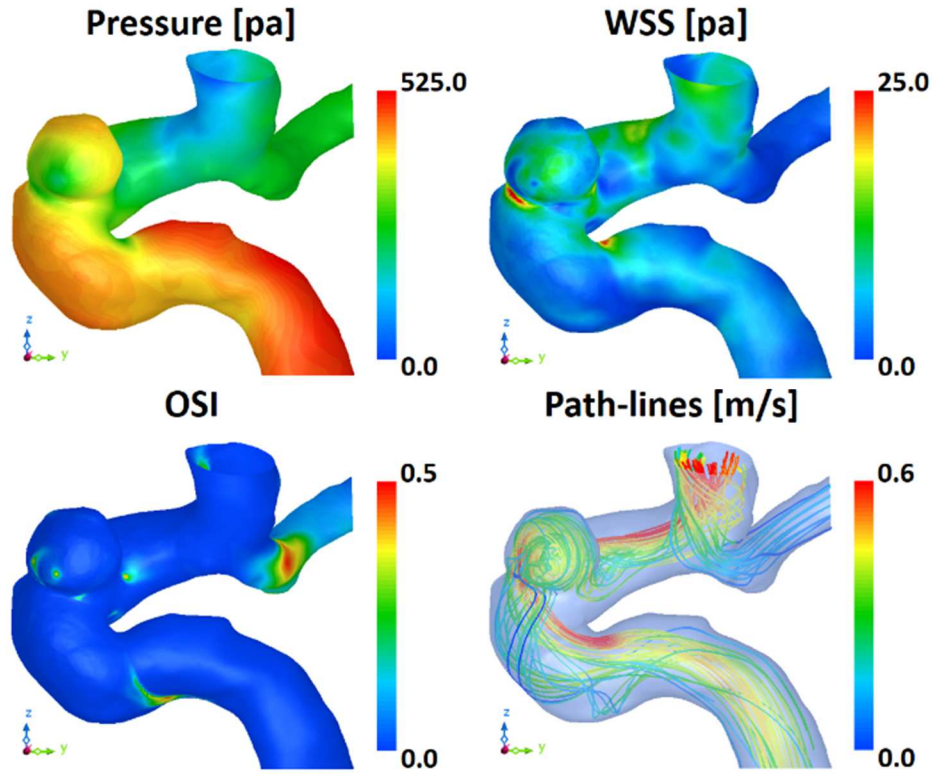


Figure 7.7 Pressure, WSS, OSI distributions over the surface and the velocity path-lines for the LICA aneurysm model.

Figure 7.8 presents the comparisons of flow and pressure waveforms at both the inlet and two exits between the stenotic LICA anomalous model and baseline model. Similarly, the overall difference of the pressure gradient between the baseline and multi-scale models is less than 1%. In contrast to the flow rate waveforms in the previous case, the anomalous model gives rise to a large drop in the flow rate in LCCA. Indeed, the changes in the mean flow rate in the CoW are shown in Table 7.1 and 7.2. The flow rate in the stenotic LICA is dropped by 36.50%. The amount of the reduced flow in LICA results in 21.50% increase in the flow rate at RICA. The decrease of flow rate in the left side of the CoW leads to an increase of RACA and RICAT by 67.60% and 22.49%, respectively. Figure 7.9 shows the WSS, OSI, and path-lines distributions over the inside wall of the artery. The maximum WSS of 35.21 Pa appears in the stenosis region. The CCA separates blood flow into the ICA and ECA, resulting in the

high OSI distributed near the bifurcation region. Likewise, the flow separations can be observed at the back of stenosis, as shown from the streamlines in Figure 7.9. Hence, high OSI distributions were observed at downstream of the stenosis.

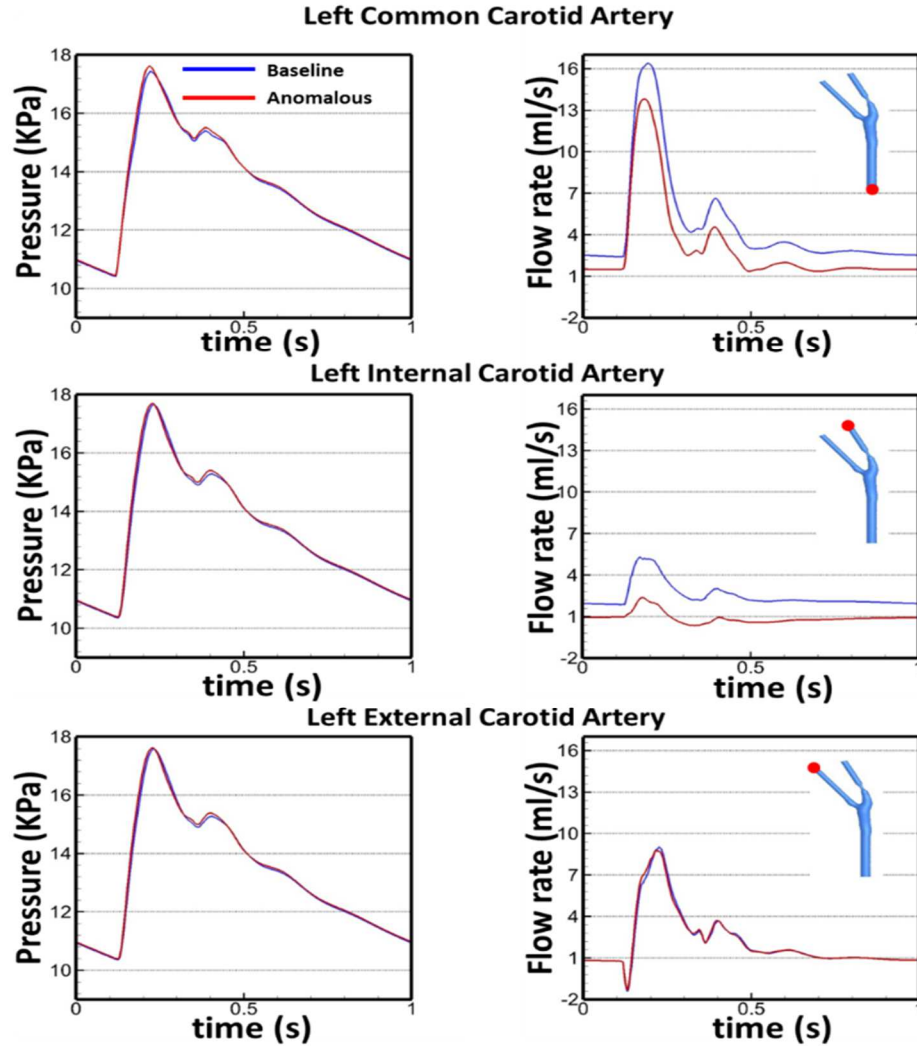


Figure 7.8 The pressure and flow rate waveforms comparisons of the multi-scale model with the baseline model at the LCCA upstream and LICA and LECA downstream as red dots represent.

Table 7.1: Comparison of mean flow rates in the CoW between the multi-scale model and the baseline model for the LCCA bifurcation model. The labels of vessels refer to the position on the CoW network on the right.

No. Vessels	Mean flow rate without LICA stenosis (ml/s)	Mean flow rate with LICA stenosis (ml/s)	Percentage difference (%)
1 RCCA	6.25	7.13	14.09
2 RICA	4.09	4.97	21.55
3 RICAT	4.26	5.21	22.49
4 RACA	1.44	2.42	67.60
5 RMCA	2.81	2.78	-0.89
6 RPCA	1.54	1.61	4.55
7 RPcoA	0.17	0.25	44.35
8 RVA	1.55	1.77	13.94
9 AcoA	0.06	1.06	1735.22

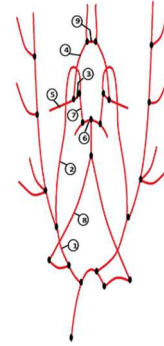


Table 7.2: Comparison of mean flow rates in the CoW between the multi-scale model and the baseline model for the LCCA bifurcation model. The labels of vessels refer to the position on the CoW network on the right.

No. Vessels	Mean flow rate without LICA stenosis (ml/s)	Mean flow rate with LICA stenosis (ml/s)	Percentage difference (%)
1 LCCA	6.12	4.66	-23.76
2 LICA	3.93	2.49	-36.50
3 LICAT	4.14	3.05	-26.23
4 LACA	1.33	0.31	-76.63
5 LMCA	2.81	2.75	-2.17
6 LPCA	1.56	1.92	23.25
7 LPcoA	0.19	0.55	193.75
8 LVA	1.56	1.77	13.98
9 BA	3.10	3.53	13.96

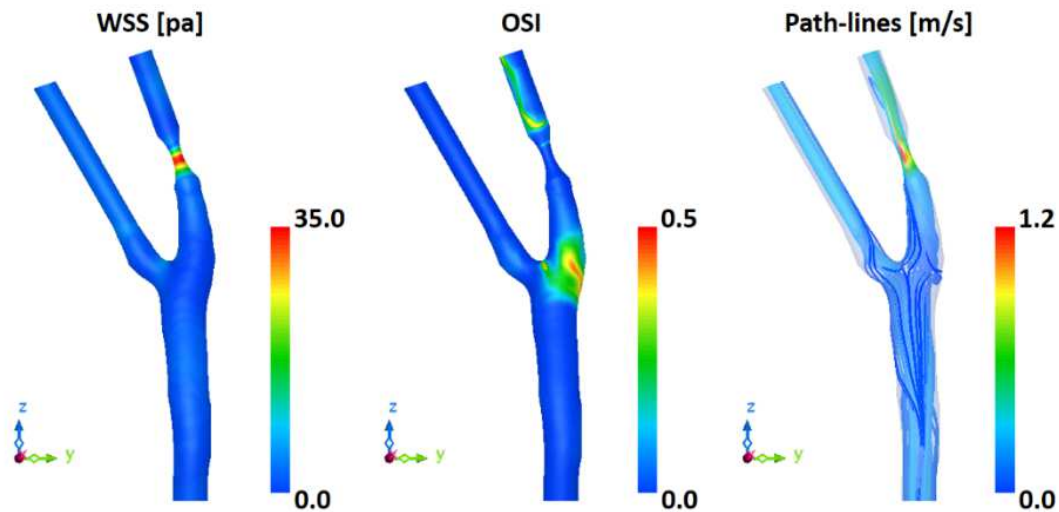
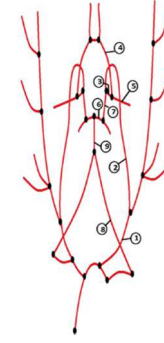


Figure 7.9 WSS, OSI distributions over the surface and the velocity path-lines for the LCCA bifurcation model.

## 7.4 Discussion

In this chapter, the 1D-3D multi-scale model has been proposed by exchanging pressure gradients and flow rates between the 1D and 3D models to account for effects of a local 3D morphological segment on the global hemodynamics. Validation studies were implemented through three simplified geometries including single and multiple artery networks to evaluate the numerical accuracy of the multi-scale model. The comparison results for the single artery model indicate that the current multi-scale model is capable of capturing the pressure drop along the centerline as compared to the previous experimental and CFD results, as shown in Figure 7.2. For bifurcation artery network models, the pressure and flow rate waveforms in each artery can also be predicted by the multi-scale model as compared to the results obtained from pure 3D models, as presented in Figure 7.3 and 7.4. In contrast to the multi-scale approach, the pure 1D model cannot accurately predict the pressure and flow rate waveforms in the bifurcation artery cases because the method failed to include the pressure feedback from the local morphological segment.

The simulation results of the patient-specific aneurysm model show that the developed cerebral aneurysm has less effect on changing the flow conditions, resulting in a 2.40% and 4.71% decrease of flow rate in ICA and ICAT, respectively. According to the current findings, the boundary conditions obtained from the pure 1D model is acceptable for ICA/ICAT case. On the other hand, the simulation results of the LICA stenosis model indicate that the severe local stenosis occurred on LICA can produce a large pressure drop leading to significant flow alterations within the CoW, as shown in Table 7.1 and 7.2. In these cases, by taking boundary conditions directly from the pure 1D numerical model without considering the feedback from the blockage of the stenosis may lead to an inaccurate

solution. Moreover, Héman et al. (2009) found that an intracranial aneurysm and the ICA stenosis coexist in patients. The proximal stenosis could lead to high WSS occurred at downstream vessels, which might associate with the cerebral aneurysm formation (Kono et al., 2013). The stenosis can cause a significant increase in flow rate in the collateral arteries around the CoW. This increased flow rate results in an augmentation of the WSS exerting on the blood vessel wall, potentially resulting in developing a cerebral aneurysm initiation (Kono et al., 2013; Griffiths et al., 1996). It is suggested that further *in vivo* or *in vitro* hemodynamic studies of the patient-specific morphological segments would be required to confirm the current investigations.

Even though the proposed multi-scale model is able to provide boundary conditions for the 3D simulation of morphological segments, the model cannot predict the boundary condition as accurate as the in-vivo patient-specific flow and pressure measurements. It should be noted that the flow waveform measured using DUT may be also accompanied with experimental uncertainties, possibly reducing the accuracy of the simulation outcomes (Xiang et al., 2014; Pereira et al., 2014). Recently, optical flow method (OFM) was proposed to extract the flow velocity and curves from a patient based on digital subtraction angiography (DSA) images, but some discrepancies can be observed as compared to DUT measurements (Pereira et al., 2014; Brina et al., 2014; Yang et al., 2017). Another limitation of the proposed multi-scale model is the assumption of the cycle-to-cycle coupling method between the 1D and 3D models by considering regular physiological conditions with the periodic flow and pressure waveforms, as reported in Liang et al., (2016). This cardio-cycle based coupling method would be invalid when the auto-regulation of blood flow perfusion of

the microcirculation is taken into account. The assumption of rigid walls and Newtonian fluid for the 3D simulation could also reduce the accuracy of the hemodynamic outcomes.

## 7.5 Summary

In this chapter, the current multi-scale model was validated against three simplified geometries and the agreement with experimental and/or full 3D simulation seemed to support the current approach. The investigation of the aneurysm and stenosis cases demonstrates that the feedback of the pressure loss from a local morphological segment can induce flow alterations. As a consequence, it results in changing the boundary conditions to interfere with the solution of the 3D simulation. Therefore, the proposed multi-scale model is proposed as an alternative computational model to study intracranial vascular diseases such as an aneurysm, stenosis, and combined cases.

# 8 CONCLUSIONS

## 8.1 Summary of the dissertation

The main contribution of the current dissertation is the development of the alternative multi-scale model by exchanging the flow and pressure conditions between the 1D and 3D models, containing the total human vessel network and local morphologies. This computational model investigates how the global hemodynamic changes can be induced by the local

morphological effects, and in consequence, may further alter the boundary conditions to interfere with solutions of the 3D simulation. This coupling approach enables patient-specific morphological models to be inserted into the total human vessel network without solving additional governing equations at the interfaces with a direct mapping of flow and pressure information between the 1D and 3D models. This simplification leads to less computational efforts when a large number of patient-specific models are required. The simulation results of the application studies presented in Chapter 7 revealed that the current aneurysm model has less effect on changing the flow rate distributions, indicating a 2.40% decrease of flow in the ICA and a 4.71% decrease in the ICA\_T. It is indicated that the boundary conditions obtained from the pure 1D model are acceptable for ICA/ICA\_T case. On the other hand, a significant drop of flow rate can be observed in the CCA bifurcation model because of the formation of the stenosis, leading to a severe imbalance of the flow distributions in the CoW. This flow alteration causes the arteries on the right side of the CoW to undergo an extra flow rate and hemodynamic stresses, possibly leading to vascular diseases.

To develop the multi-scale model, a previously published 1D numerical model was employed, and the evaluation of the numerical accuracy of the 1D model has been implemented by comparing the simulated results with previous *in vivo* measurements and numerical results. In the meantime, an experimental study of flow through a silicone arterial network has been conducted to assess the accuracy of the 1D numerical model. The comparison results of the pressure waveforms indicate that the 1D model is able to capture the main features occurred at the systolic regions, whereas the 1D model underestimates the pressure at the pre-systolic region and overestimates the pressure at the diastolic region. Quantitatively, the mean flow



rates for all measured arteries can be precisely predicted by the 1D model, and the overall difference between the numerical and experimental results is smaller than 1%.

The other contribution of this dissertation is the investigation of the effects of NVA and EVA on hemodynamic characteristics in the CoW by using the 1D numerical model. The numerical simulations revealed that higher central pulse pressure and AIx appear in the EVA subjects due to the early arrival of reflected waves, resulted in the increase of cardiac afterload compared with the NVA subjects. Moreover, the hemodynamic characteristics in the CoW show that the EVA subjects in an older age display a higher blood pressure than that of the NVA with a complete CoW. Herein, the increased blood pressure and flow rate coexist in the subjects with an incomplete CoW. In conclusion, the hemodynamic characteristics of the aortic tree and CoW related to aging appear to play an important role in causing cardiovascular and intravascular disease.

This dissertation also contributes to investigating the hemodynamic characteristics in variations of the CoW by using the 1D numerical model. Such as the variations of the CoW with missing A1 or missing P1, are confirmed by *in vivo* experimental data. It is demonstrated that the CoW has the ability to shunt blood flow and ensure the amount of the supplement of blood to different areas in the brain. However, the redistribution of blood flow can cause particular vessels to undergo extra flow rate and hemodynamic stresses, potentially resulting in developing vascular diseases.

A patient-specific model of a saccular ICA aneurysm was reconstructed from 3D rotational DSA images. The current dissertation presented 3D CFD simulations to investigate how the aneurysm shape and size effects on the hemodynamics of a cerebral aneurysm. To achieve this goal, enlarged and bi-lobed aneurysm morphologies were created based on the original

anatomic. The simulation results indicate that the bi-lobed aneurysm is able to increase the WSS over the sac, while the enlarged aneurysm contributes a decrease of the WSS exerting on the sac surface because of the flow reduction inside the aneurysm. However, the conclusions related to the hemodynamic risk factors for a cerebral aneurysm cannot be made because the hemodynamic changes obtained from only one aneurysm model are not representative. Therefore, further investigations are required by linking the biomedical hemodynamics study with the biology together to explore the effects of the WSS on the deformation of blood vessel wall.

## 8.2 Future applications of the model

The proposed 1D numerical model can be applied to investigate the hemodynamics of various vascular diseases such as cardiovascular diseases. By modifying the 0D model of the heart, a quick understanding on the hemodynamic changes induced by the stenosis of the heart valves can be obtained. By changing the arterial compliance, geometry, and the terminal resistance, the effects of vascular drugs on the pulse wave propagations along the arterial circulation system can be investigated.

To treat cerebral aneurysms, endovascular treatment has been widely adopted as the primary treatment strategy for complex aneurysms depending on the location and size, such as flow diverter stent and stent-assisted coiling. However, adverse clinical outcomes could occur after placing a stent, such as in-stent stenosis and occlusion (Tan et al., 2014). Thus, the proposed 1D-3D multi-scale model can be used to simulate the possible hemodynamic outcomes of stented aneurysms by comparing the pressure, WSS, and flow patterns in pre- and post-treatment aneurysm models. This simulation could aid in assessing the endovascular

treatment strategies from the biomechanical perspective and provide valuable information for the treatment options of a complex cerebral aneurysm.

## 9 REFERENCES

- Ahmed, M.M., Reddy, M.V., Venkatachary, M., Waheed, A., 2015. Human Anatomic variations in the formation of circulus arteriosus – A dissection method. *Int. J. Sci. Res. Pub.* 5, 1-6
- Alastruey, J., Khir, A.W., Matthys, K.S., Segers, P., Sherwin, S.J., Verdonck, P.R., Parker, K.H. and Peiró, J., 2011. Pulse wave propagation in a model human arterial network: assessment of 1-D visco-elastic simulations against in vitro measurements. *Journal of biomechanics*, 44(12), pp.2250-2258.
- Alastruey, J., Moore, S.M., Parker, K.H., David, T., Peiró, J. and Sherwin, S.J., 2008. Reduced modelling of blood flow in the cerebral circulation: Coupling 1 - D, 0 - D and cerebral auto - regulation models. *International journal for numerical methods in fluids*, 56(8), pp.1061-1067.
- Alastruey, J., Parker, K.H. and Sherwin, S.J., 2012, October. Arterial pulse wave haemodynamics. In 11th International Conference on Pressure Surges (pp. 401-442). Virtual PiE Led t/a BHR Group: Lisbon, Portugal.
- Alastruey, J., Parker, K.H., Peiró, J. and Sherwin, S.J., 2008. Lumped parameter outflow models for 1-D blood flow simulations: effect on pulse waves and parameter estimation. *Communications in Computational Physics*, 4(2), pp.317-336.
- Alastruey, J., Parker, K.H., Peiró, J., Byrd, S.M. and Sherwin, S.J., 2007. Modelling the circle of Willis to assess the effects of anatomical variations and occlusions on cerebral flows. *Journal of biomechanics*, 40(8), pp.1794-1805.

Alastruey, J., Passerini, T., Formaggia, L. and Peiró, J., 2012. Physical determining factors of the arterial pulse waveform: theoretical analysis and calculation using the 1-D formulation. *Journal of Engineering Mathematics*, 77(1), pp.19-37.

Alastruey, J., Passerini, T., Formaggia, L. and Peiró, J., 2012. Physical determining factors of the arterial pulse waveform: theoretical analysis and calculation using the 1-D formulation. *Journal of Engineering Mathematics*, 77(1), pp.19-37.

Antikainen, R.L., Jousilahti, P., Vanhanen, H. and Tuomilehto, J., 2000. Excess mortality associated with increased pulse pressure among middle-aged men and women is explained by high systolic blood pressure. *Journal of hypertension*, 18(4), pp.417-423.

Appanaboyina, S., Mut, F., Löhner, R., Putman, C. and Cebal, J., 2009. Simulation of intracranial aneurysm stenting: techniques and challenges. *Computer Methods in Applied Mechanics and Engineering*, 198(45-46), pp.3567-3582.

Arbab-Zadeh, A., Dijk, E., Prasad, A., Fu, Q., Torres, P., Zhang, R., Thomas, J.D., Palmer, D. and Levine, B.D., 2004. Effect of aging and physical activity on left ventricular compliance. *Circulation*, 110(13), pp.1799-1805.

Aune, E., Baekkevar, M., Roislien, J., Rodevand, O. and Otterstad, J.E., 2009. Normal reference ranges for left and right atrial volume indexes and ejection fractions obtained with real-time three-dimensional echocardiography. *European Journal of Echocardiography*, 10(6), pp.738-744.

Avolio, A.P., Chen, S.G., Wang, R.P., Zhang, C.L., Li, M.F. and O'Rourke, M.F., 1983. Effects of aging on changing arterial compliance and left ventricular load in a northern Chinese urban community. *Circulation*, 68(1), pp.50-58.

- Azer, K. and Peskin, C.S., 2007. A one-dimensional model of blood flow in arteries with friction and convection based on the Womersley velocity profile. *Cardiovascular Engineering*, 7(2), pp.51-73.
- Ballotta, E., Da Giau, G., Manara, R. and Baracchini, C., 2006. Extracranial severe carotid stenosis and incidental intracranial aneurysms. *Annals of vascular surgery*, 20(1), pp.5-8.
- Banerjee, R.K., Ashtekar, K.D., Helmy, T.A., Effat, M.A., Back, L.H. and Khoury, S.F., 2008. Hemodynamic diagnostics of epicardial coronary stenoses: in-vitro experimental and computational study. *Biomedical engineering online*, 7(1), p.24.
- Berg, P., Stucht, D., Janiga, G., Beuing, O., Speck, O. and Thévenin, D., 2014. Cerebral blood flow in a healthy Circle of Willis and two intracranial aneurysms: computational fluid dynamics versus four-dimensional phase-contrast magnetic resonance imaging. *Journal of biomechanical engineering*, 136(4), p.041003.
- Bessemers, D., Rutten, M. and Van De Vosse, F., 2007. A wave propagation model of blood flow in large vessels using an approximate velocity profile function. *Journal of Fluid Mechanics*, 580, pp.145-168.
- Blanco, P.J. and Feijóo, R.A., 2010. A 3D-1D-0D Computational model for the entire cardiovascular system. *Computational Mechanics*, eds. E. Dvorking, M. Goldschmit, M. Storti, 29, pp.5887-5911.
- Blanco, P.J. and Feijóo, R.A., 2013. A dimensionally-heterogeneous closed-loop model for the cardiovascular system and its applications. *Medical Engineering and Physics*, 35(5), pp.652-667.

Blanco, P.J., Feijóo, R.A. and Urquiza, S.A., 2007. A unified variational approach for coupling 3D–1D models and its blood flow applications. *Computer Methods in Applied Mechanics and Engineering*, 196(41-44), pp.4391-4410.

Blanco, P.J., Pivello, M.R., Urquiza, S.A. and Feijóo, R.A., 2009. On the potentialities of 3D–1D coupled models in hemodynamics simulations. *Journal of Biomechanics*, 42(7), pp.919-930.

Blanco, P.J., Urquiza, S.A. and Feijóo, R.A., 2010. Assessing the influence of heart rate in local hemodynamics through coupled 3D-1D-0D models. *International Journal for Numerical Methods in Biomedical Engineering*, 26(7), pp.890-903.

Blanco, P.J., Watanabe, S.M., Passos, M.A.R., Lemos, P.A. and Feijóo, R.A., 2015. An anatomically detailed arterial network model for one-dimensional computational hemodynamics. *IEEE Transactions on biomedical engineering*, 62(2), pp.736-753.

Boileau, E., Nithiarasu, P., Blanco, P.J., Müller, L.O., Fossan, F.E., Hellevik, L.R., Donders, W.P., Huberts, W., Willemet, M. and Alastruey, J., 2015. A benchmark study of numerical schemes for one - dimensional arterial blood flow modelling. *International journal for numerical methods in biomedical engineering*, 31(10).

Boussel, L., Rayz, V., McCulloch, C., Martin, A., Acevedo-Bolton, G., Lawton, M., Higashida, R., Smith, W.S., Young, W.L. and Saloner, D., 2008. Aneurysm growth occurs at region of low wall shear stress. *Stroke*, 39(11), pp.2997-3002.

Brina, O., Ouared, R., Bonnefous, O., van Nijnatten, F., Bouillot, P., Bijlenga, P., Schaller, K., Lovblad, K.O., Grünhagen, T., Ruijters, D. and Pereira, V.M., (2014). Intra-aneurysmal flow patterns: illustrative comparison among digital subtraction angiography, optical flow,

and computational fluid dynamics. *American Journal of Neuroradiology*, 35(12), pp.2348-2353.

Bullitt, E., Zeng, D., Mortamet, B., Ghosh, A., Aylward, S.R., Lin, W., Marks, B.L. and Smith, K., 2010. The effects of healthy aging on intracerebral blood vessels visualized by magnetic resonance angiography. *Neurobiology of aging*, 31(2), pp.290-300.

Castro, M.A., Putman, C.M., Sheridan, M.J. and Cebal, J.R., 2009. Hemodynamic patterns of anterior communicating artery aneurysms: a possible association with rupture. *American journal of neuroradiology*, 30(2), pp.297-302.

Cebal, J.R. and Raschi, M., 2013. Suggested connections between risk factors of intracranial aneurysms: a review. *Annals of biomedical engineering*, 41(7), pp.1366-1383.

Cebal, J.R., Castro, M.A., Burgess, J.E., Pergolizzi, R.S., Sheridan, M.J. and Putman, C.M., 2005. Characterization of cerebral aneurysms for assessing risk of rupture by using patient-specific computational hemodynamics models. *American Journal of Neuroradiology*, 26(10), pp.2550-2559.

Cebal, J.R., Mut, F., Weir, J. and Putman, C., 2011. Quantitative characterization of the hemodynamic environment in ruptured and unruptured brain aneurysms. *American Journal of Neuroradiology*, 32(1), pp.145-151.

Chandran, K.B., Rittgers, S.E. and Yoganathan, A.P., 2012. *Biofluid mechanics: the human circulation*. CRC press.

Chatziprodromou, I., Tricoli, A., Poulikakos, D. and Ventikos, Y., 2007. Haemodynamics and wall remodelling of a growing cerebral aneurysm: a computational model. *Journal of biomechanics*, 40(2), pp.412-426.



Cheng, C.P., Herfkens, R.J. and Taylor, C.A., 2003. Inferior vena caval hemodynamics quantified in vivo at rest and during cycling exercise using magnetic resonance imaging. *American Journal of Physiology-Heart and Circulatory Physiology*, 284(4), pp.H1161-H1167.

Cieslicki, K. and Ciesla, D., 2005. Investigations of flow and pressure distributions in physical model of the circle of Willis. *Journal of biomechanics*, 38(11), pp.2302-2310.

Cunha, P.G., Cotter, J., Oliveira, P., Vila, I., Boutouyrie, P., Laurent, S., Nilsson, P.M., Scuteri, A. and Sousa, N., 2015. Pulse wave velocity distribution in a cohort study: from arterial stiffness to early vascular aging. *Journal of hypertension*, 33(7), pp.1438-1445.

de Boorder, M.J., van der Grond, J., van Dongen, A.J., Klijn, C.J., Kappelle, L.J., Van Rijk, P.P. and Hendrikse, J., 2006. Spect measurements of regional cerebral perfusion and carbondioxide reactivity: correlation with cerebral collaterals in internal carotid artery occlusive disease. *Journal of neurology*, 253(10), pp.1285-1291.

de Rooij, N.K., Velthuis, B.K., Algra, A. and Rinkel, G.J., 2009. Configuration of the circle of Willis, direction of flow, and shape of the aneurysm as risk factors for rupture of intracranial aneurysms. *Journal of neurology*, 256(1), p.45.

Dexter, L., Dow, J.W., Haynes, F.W., Whittenberger, J.L., Ferris, B.G., Goodale, W.T. and Hellems, H.K., 1950. Studies of the pulmonary circulation in man at rest. Normal variations and the interrelations between increased pulmonary blood flow, elevated pulmonary arterial pressure, and high pulmonary “capillary” pressures. *The Journal of clinical investigation*, 29(5), pp.602-613.

Dhar, S., Tremmel, M., Mocco, J., Kim, M., Yamamoto, J., Siddiqui, A.H., Hopkins, L.N. and Meng, H., 2008. Morphology parameters for intracranial aneurysm rupture risk assessment. *Neurosurgery*, 63(2), pp.185-197.

- Dolan, J.M., Kolega, J. and Meng, H., 2013. High wall shear stress and spatial gradients in vascular pathology: a review. *Annals of biomedical engineering*, 41(7), pp.1411-1427.
- Fahy, P., Delassus, P., McCarthy, P., Sultan, S., Hynes, N. and Morris, L., 2014. An in vitro assessment of the cerebral hemodynamics through three patient specific circle of Willis geometries. *Journal of biomechanical engineering*, 136(1), p.011007.
- Fahy, P., McCarthy, P., Sultan, S., Hynes, N., Delassus, P. and Morris, L., 2014. An experimental investigation of the hemodynamic variations due to aplastic vessels within three-dimensional phantom models of the circle of Willis. *Annals of biomedical engineering*, 42(1), pp.123-138.
- Ford, M.D., Alperin, N., Lee, S.H., Holdsworth, D.W. and Steinman, D.A., 2005. Characterization of volumetric flow rate waveforms in the normal internal carotid and vertebral arteries. *Physiological measurement*, 26(4), p.477.
- Formaggia, L. and Veneziani, A., 2003. Reduced and multiscale models for the human cardiovascular system. *Lecture notes VKI lecture series*, 7.
- Formaggia, L. and Veneziani, A., 2003. Reduced and multiscale models for the human cardiovascular system. *Lecture notes VKI lecture series*, 7.
- Formaggia, L., Gerbeau, J.F., Nobile, F. and Quarteroni, A., 2001. On the coupling of 3D and 1D Navier–Stokes equations for flow problems in compliant vessels. *Computer methods in applied mechanics and engineering*, 191(6-7), pp.561-582.
- Formaggia, L., Lamponi, D. and Quarteroni, A., 2003. One-dimensional models for blood flow in arteries. *Journal of engineering mathematics*, 47(3-4), pp.251-276.

Formaggia, L., Nobile, F., Quarteroni, A. and Veneziani, A., 1999. Multiscale modelling of the circulatory system: a preliminary analysis. *Computing and visualization in science*, 2(2-3), pp.75-83.

Formaggia, L., Quarteroni, A. and Veneziani, A. eds., 2010. *Cardiovascular Mathematics: Modeling and simulation of the circulatory system (Vol. 1)*. Springer Science & Business Media.

Fortune, J.B. and Feustel, P., 2003. Effect of patient position on size and location of the subclavian vein for percutaneous puncture. *Archives of Surgery*, 138(9), pp.996-1000.

Gayat, E., Mor-Avi, V., Weinert, L., Yodwut, C. and Lang, R.M., 2011. Noninvasive quantification of left ventricular elastance and ventricular-arterial coupling using three-dimensional echocardiography and arterial tonometry. *American Journal of Physiology-Heart and Circulatory Physiology*, 301(5), pp.H1916-H1923.

Gibbons, G.H. and Dzau, V.J., 1994. The emerging concept of vascular remodeling. *New England Journal of Medicine*, 330(20), pp.1431-1438.

GrabCad [online], Grabcad. Available at: <https://grabcad.com/library/carotid-bifurcation>.

Griffith, T.M., 1994. Modulation of blood flow and tissue perfusion by endothelium - derived relaxing factor. *Experimental physiology*, 79(6), pp.873-913.

Gwilliam, M.N., Hoggard, N., Capener, D., Singh, P., Marzo, A., Verma, P.K. and Wilkinson, I.D., 2009. MR derived volumetric flow rate waveforms at locations within the common carotid, internal carotid, and basilar arteries. *Journal of Cerebral Blood Flow & Metabolism*, 29(12), pp.1975-1982.

Han, L., Bai, X., Lin, H., Sun, X. and Chen, X., 2013. Gender differences in the relationship between age-related carotid intima-media thickness and cardiac diastolic function in a healthy Chinese population. *Journal of cardiac failure*, 19(5), pp.325-332.

Héman, L.M., Jongen, L.M., van der Worp, H.B., Rinkel, G.J. and Hendrikse, J., 2009. Incidental intracranial aneurysms in patients with internal carotid artery stenosis: a CT angiography study and a metaanalysis. *Stroke*, 40(4), pp.1341-1346.

Hendrikse, J., van Raamt, A.F., van der Graaf, Y., Mali, W.P. and van der Grond, J., 2005. Distribution of cerebral blood flow in the circle of Willis. *Radiology*, 235(1), pp.184-189.

Huang, P.G. and Muller, L.O., 2015. Simulation of one - dimensional blood flow in networks of human vessels using a novel TVD scheme. *International journal for numerical methods in biomedical engineering*, 31(5).

Huang, G.P., Yu, H., Yang, Z., Schwieterman, R. and Ludwig, B., 2018. 1D simulation of blood flow characteristics in the circle of Willis using THINKS. *Computer methods in biomechanics and biomedical engineering*, 21(4), pp.389-397.

Humphrey, J.D. and Taylor, C.A., 2008. Intracranial and abdominal aortic aneurysms: similarities, differences, and need for a new class of computational models. *Annu. Rev. Biomed. Eng.*, 10, pp.221-246.

Humphrey, J.D., 2008. Vascular adaptation and mechanical homeostasis at tissue, cellular, and sub-cellular levels. *Cell biochemistry and biophysics*, 50(2), pp.53-78.

Kasuya, H., Shimizu, T., Nakaya, K., Sasahara, A., Hori, T. and Takakura, K., 1999. Angles between A1 and A2 segments of the anterior cerebral artery visualized by three-dimensional computed tomographic angiography and association of anterior communicating artery aneurysms. *Neurosurgery*, 45(1), pp.89-94.

- Kawaguchi, M., Hay, I., Fetics, B. and Kass, D.A., 2003. Combined ventricular systolic and arterial stiffening in patients with heart failure and preserved ejection fraction: implications for systolic and diastolic reserve limitations. *Circulation*, 107(5), pp.714-720.
- Kayembe, K.N., Sasahara, M. and Hazama, F., 1984. Cerebral aneurysms and variations in the circle of Willis. *Stroke*, 15(5), pp.846-850.
- Kolega, J., Gao, L., Mandelbaum, M., Mocco, J., Siddiqui, A.H., Natarajan, S.K. and Meng, H., 2011. Cellular and molecular responses of the basilar terminus to hemodynamics during intracranial aneurysm initiation in a rabbit model. *Journal of vascular research*, 48(5), pp.429-442.
- Kotsis, V., Stabouli, S., Karafillis, I. and Nilsson, P., 2011. Early vascular aging and the role of central blood pressure. *Journal of hypertension*, 29(10), pp.1847-1853.
- Krasny, A., Nensa, F., Sandalcioğlu, I.E., Göricke, S.L., Wanke, I., Gramsch, C., Sirin, S., Oezkan, N., Sure, U. and Schlamann, M., 2014. Association of aneurysms and variation of the A1 segment. *Journal of neurointerventional surgery*, 6(3), pp.178-183.
- Lakatta, E.G. and Levy, D., 2003. Arterial and cardiac aging: major shareholders in cardiovascular disease enterprises: Part I: aging arteries: a “set up” for vascular disease. *Circulation*, 107(1), pp.139-146.
- Lakatta, E.G., 1993. Cardiovascular regulatory mechanisms in advanced age. *Physiological reviews*, 73(2), pp.413-467.
- Larrabide, I., Geers, A.J., Morales, H.G., Bijlenga, P. and Rüfenacht, D.A., 2016. Change in aneurysmal flow pulsatility after flow diverter treatment. *Computerized Medical Imaging and Graphics*, 50, pp.2-8.

- Lasheras, J.C., 2007. The biomechanics of arterial aneurysms. *Annu. Rev. Fluid Mech.*, 39, pp.293-319.
- Lazzaro, M.A., Ouyang, B. and Chen, M., 2012. The role of circle of Willis anomalies in cerebral aneurysm rupture. *Journal of neurointerventional surgery*, 4(1), pp.22-26.
- Lee, H.Y. and Oh, B.H., 2010. Aging and arterial stiffness. *Circulation Journal*, 74(11), pp.2257-2262.
- Lee, J.H., Choi, C.G., Kim, D.K., Kim, G.E., Lee, H.K. and Suh, D.C., 2004. Relationship between circle of Willis morphology on 3D time-of-flight MR angiograms and transient ischemia during vascular clamping of the internal carotid artery during carotid endarterectomy. *American journal of neuroradiology*, 25(4), pp.558-564.
- Liang, F. and Liu, H., 2005. A closed-loop lumped parameter computational model for human cardiovascular system. *JSME International Journal Series C Mechanical Systems, Machine Elements and Manufacturing*, 48(4), pp.484-493.
- Liang, F., Fukasaku, K., Liu, H. and Takagi, S., 2011. A computational model study of the influence of the anatomy of the circle of Willis on cerebral hyperperfusion following carotid artery surgery. *Biomedical engineering online*, 10(1), p.84.
- Liang, F., Liu, X., Yamaguchi, R. and Liu, H., 2016. Sensitivity of flow patterns in aneurysms on the anterior communicating artery to anatomic variations of the cerebral arterial network. *Journal of biomechanics*, 49(15), pp.3731-3740.
- Liang, F., Oshima, M., Huang, H., Liu, H. and Takagi, S., 2015. Numerical study of cerebroarterial hemodynamic changes following carotid artery operation: a comparison between multiscale modeling and stand-alone three-dimensional modeling. *Journal of Biomechanical Engineering*, 137(10), p.101011.

- Liang, F., Takagi, S., Himeno, R. and Liu, H., 2009. Multi-scale modeling of the human cardiovascular system with applications to aortic valvular and arterial stenoses. *Medical & biological engineering & computing*, 47(7), pp.743-755.
- Liang, F.Y., Takagi, S., Himeno, R. and Liu, H., 2009. Biomechanical characterization of ventricular–arterial coupling during aging: a multi-scale model study. *Journal of biomechanics*, 42(6), pp.692-704.
- Long, Q., Luppi, L., König, C.S., Rinaldo, V. and Das, S.K., 2008. Study of the collateral capacity of the circle of Willis of patients with severe carotid artery stenosis by 3D computational modeling. *Journal of biomechanics*, 41(12), pp.2735-2742.
- Malek, A.M., Alper, S.L. and Izumo, S., 1999. Hemodynamic shear stress and its role in atherosclerosis. *Jama*, 282(21), pp.2035-2042.
- Malek, A.M., Alper, S.L. and Izumo, S., 1999. Hemodynamic shear stress and its role in atherosclerosis. *Jama*, 282(21), pp.2035-2042.
- Malossi, A.C.I., Blanco, P.J., Crosetto, P., Deparis, S. and Quarteroni, A., 2013. Implicit coupling of one-dimensional and three-dimensional blood flow models with compliant vessels. *Multiscale Modeling & Simulation*, 11(2), pp.474-506.
- Matthys, K.S., Alastruey, J., Peiró, J., Khir, A.W., Segers, P., Verdonck, P.R., Parker, K.H. and Sherwin, S.J., 2007. Pulse wave propagation in a model human arterial network: assessment of 1-D numerical simulations against in vitro measurements. *Journal of biomechanics*, 40(15), pp.3476-3486.
- McEniery, C.M., Hall, I.R., Qasem, A., Wilkinson, I.B., Cockcroft, J.R. and Acet Investigators, 2005. Normal vascular aging: differential effects on wave reflection and aortic

pulse wave velocity: the Anglo-Cardiff Collaborative Trial (ACCT). *Journal of the American College of Cardiology*, 46(9), pp.1753-1760.

Meng, H., Tutino, V.M., Xiang, J. and Siddiqui, A., 2014. High WSS or low WSS? Complex interactions of hemodynamics with intracranial aneurysm initiation, growth, and rupture: toward a unifying hypothesis. *American Journal of Neuroradiology*, 35(7), pp.1254-1262.

Metaxa, E., Tremmel, M., Natarajan, S.K., Xiang, J., Paluch, R.A., Mandelbaum, M., Siddiqui, A.H., Kolega, J., Mocco, J. and Meng, H., 2010. Characterization of critical hemodynamics contributing to aneurysmal remodeling at the basilar terminus in a rabbit model. *Stroke*, 41(8), pp.1774-1782.

Moncada, S.R.M.J., Palmer, R.M.L. and Higgs, E.A., 1991. Nitric oxide: physiology, pathophysiology, and pharmacology. *Pharmacological reviews*, 43(2), pp.109-142.

Montecinos, G.I., Müller, L.O. and Toro, E.F., 2014. Hyperbolic reformulation of a 1D viscoelastic blood flow model and ADER finite volume schemes. *Journal of Computational Physics*, 266, pp.101-123.

Moore, S., David, T., Chase, J.G., Arnold, J. and Fink, J., 2006. 3D models of blood flow in the cerebral vasculature. *Journal of biomechanics*, 39(8), pp.1454-1463.

Müller, L.O. and Blanco, P.J., 2015. A high order approximation of hyperbolic conservation laws in networks: application to one-dimensional blood flow. *Journal of Computational Physics*, 300, pp.423-437.

Müller, L.O. and Toro, E.F., 2013. Well-balanced high-order solver for blood flow in networks of vessels with variable properties. *International Journal for Numerical Methods in Biomedical Engineering*, 29(12), pp.1388-1411.



Müller, L.O. and Toro, E.F., 2014. A global multiscale mathematical model for the human circulation with emphasis on the venous system. *International journal for numerical methods in biomedical engineering*, 30(7), pp.681-725.

Muntner, P., Whittle, J., Lynch, A.I., Colantonio, L.D., Simpson, L.M., Einhorn, P.T., Levitan, E.B., Whelton, P.K., Cushman, W.C., Louis, G.T. and Davis, B.R., 2015. Visit-to-visit variability of blood pressure and coronary heart disease, stroke, heart failure, and mortality: a cohort study. *Annals of internal medicine*, 163(5), pp.329-338.

Murgo, J.P., Westerhof, N., Giolma, J.P. and Altobelli, S.A., 1980. Aortic input impedance in normal man: relationship to pressure wave forms. *Circulation*, 62(1), pp.105-116.

Mut, F. and Cebal, J.R., 2012. Effects of flow-diverting device oversizing on hemodynamics alteration in cerebral aneurysms. *American Journal of Neuroradiology*, 33(10), pp.2010-2016.

Mynard, J.P. and Nithiarasu, P., 2008. A 1D arterial blood flow model incorporating ventricular pressure, aortic valve and regional coronary flow using the locally conservative Galerkin (LCG) method. *International Journal for Numerical Methods in Biomedical Engineering*, 24(5), pp.367-417.

Mynard, J.P. and Smolich, J.J., 2015. One-dimensional haemodynamic modeling and wave dynamics in the entire adult circulation. *Annals of biomedical engineering*, 43(6), pp.1443-1460.

Mynard, J.P., Wasserman, B.A. and Steinman, D.A., 2013. Errors in the estimation of wall shear stress by maximum Doppler velocity. *Atherosclerosis*, 227(2), pp.259-266.

Nabeshima, M., F. Moriyasu, K. Nishikawa, N. Hamato, M. Fujimoto, Takayuki Nada, Nabeshima, M., Moriyasu, F., Nishikawa, K., Hamato, N., Fujimoto, M., Nada, T., Okuma,

M. and Shimizu, K., 1995. Azygos venous blood flow: measurement with direct bolus imaging. *Radiology*, 195(2), pp.467-470.

Nichols, W.W. and O'Rourke, M.F., 2005. *McDonald's Blood Flow in Arteries* 5th edn (London: Arnold).

Nichols, W.W., 1993. Effects of age and of hypertension on wave travel and reflections. *Arterial vasodilation: Mechanisms and therapy*.

Nilsson, P.M., 2008. Early vascular aging (EVA): consequences and prevention. *Vascular health and risk management*, 4(3), p.547.

Nilsson, P.M., 2014. Hemodynamic aging as the consequence of structural changes associated with early vascular aging (EVA). *Aging and disease*, 5(2), p.109.

Nilsson, P.M., 2015. Early Vascular Ageing—A Concept in Development. *Eur. Endocrinol*, 11(1), pp.26-31.

Nippa, J.H., Alexander, R.H. and Folsie, R., 1971. Pulse wave velocity in human veins. *Journal of applied physiology*, 30(4), pp.558-563.

Nixon, A.M., Gunel, M. and Sumpio, B.E., 2010. The critical role of hemodynamics in the development of cerebral vascular disease: a review. *Journal of neurosurgery*, 112(6), pp.1240-1253.

Nobile, F. 2009. Coupling strategies for the numerical simulation of blood flow in deformable arteries by 3D and 1D models. *Mathematical and Computer Modelling*, 49(11), 2152-2160.

Omodaka, S., Sugiyama, S.I., Inoue, T., Funamoto, K., Fujimura, M., Shimizu, H., Hayase, T., Takahashi, A. and Tominaga, T., 2012. Local hemodynamics at the rupture point of

cerebral aneurysms determined by computational fluid dynamics analysis. *Cerebrovascular Diseases*, 34(2), pp.121-129.

Papadakis, G. 2009. Coupling 3D and 1D fluid - structure - interaction models for wave propagation in flexible vessels using a finite volume pressure - correction scheme. *International Journal for Numerical Methods in Biomedical Engineering*, 25(5), 533-551.

Passerini, T., De Luca, M., Formaggia, L., Quarteroni, A. and Veneziani, A., 2009. A 3D/1D geometrical multiscale model of cerebral vasculature. *Journal of Engineering Mathematics*, 64(4), p.319.

Perdikaris, P., Grinberg, L. and Karniadakis, G.E., 2015. An effective fractal-tree closure model for simulating blood flow in large arterial networks. *Annals of biomedical engineering*, 43(6), pp.1432-1442.

Pereira, V.M., Brina, O., Gonzales, A.M., Narata, A.P., Bijlenga, P., Schaller, K., Lovblad, K.O. and Ouared, R., 2013. Evaluation of the influence of inlet boundary conditions on computational fluid dynamics for intracranial aneurysms: a virtual experiment. *Journal of biomechanics*, 46(9), pp.1531-1539.

Pereira, V.M., Ouared, R., Brina, O., Bonnefous, O., Satwiaski, J., Aerts, H., Ruijters, D., van Nijnatten, F., Perren, F., Bijlenga, P. and Schaller, K., (2014). Quantification of internal carotid artery flow with digital subtraction angiography: validation of an optical flow approach with Doppler ultrasound. *American Journal of Neuroradiology*, 35(1), pp.156-163.

Pocock, Gillian 2006. *Human Physiology*. Oxford University Press. p. 264. ISBN 978-0-19-856878-0

Pontrelli, G., 2004. A multiscale approach for modelling wave propagation in an arterial segment. *Computer methods in biomechanics and biomedical engineering*, 7(2), pp.79-89.

Quarteroni, A., 2001. Modeling the cardiovascular system—A mathematical adventure: Part I. SIAM News, 34(5), pp.1-3.

Qureshi, A.I., 2004. Endovascular treatment of cerebrovascular diseases and intracranial neoplasms. The Lancet, 363(9411), pp.804-813.

Redfield, M.M., Jacobsen, S.J., Borlaug, B.A., Rodeheffer, R.J. and Kass, D.A., 2005. Age- and gender-related ventricular-vascular stiffening: a community-based study. Circulation, 112(15), pp.2254-2262.

Reference Values for Arterial Stiffness' Collaboration, 2010. Determinants of pulse wave velocity in healthy people and in the presence of cardiovascular risk factors: 'establishing normal and reference values'. European heart journal, 31(19), pp.2338-2350.

Reorowicz, P., Obidowski, D., Klosinski, P., Szubert, W., Stefanczyk, L. and Jozwik, K., 2014. Numerical simulations of the blood flow in the patient-specific arterial cerebral circle region. Journal of biomechanics, 47(7), pp.1642-1651.

Reymond, P., Bohraus, Y., Perren, F., Lazeyras, F. and Stergiopoulos, N., 2011. Validation of a patient-specific one-dimensional model of the systemic arterial tree. American Journal of Physiology-Heart and Circulatory Physiology, 301(3), pp.H1173-H1182.

Saeed, S., Waje-Andreassen, U., Fromm, A., Øygarden, H., Kokorina, M.V., Naess, H. and Gerds, E., 2014. Early vascular aging in young and middle-aged ischemic stroke patients: the Norwegian Stroke in the Young Study. PloS one, 9(11), p.e112814.

Sako, H., Miura, S.I., Kumagai, K. and Saku, K., 2009. Associations between augmentation index and severity of atheroma or aortic stiffness of the descending thoracic aorta by transesophageal echocardiography. Circulation Journal, 73(6), pp.1151-1156.

Salton, C.J., Chuang, M.L., O'Donnell, C.J., Kupka, M.J., Larson, M.G., Kissinger, K.V., Edelman, R.R., Levy, D. and Manning, W.J., 2002. Gender differences and normal left ventricular anatomy in an adult population free of hypertension: A cardiovascular magnetic resonance study of the Framingham Heart Study Offspring cohort. *Journal of the American College of Cardiology*, 39(6), pp.1055-1060.

Sherwin, S.J., Franke, V., Peiró, J. and Parker, K., 2003. One-dimensional modelling of a vascular network in space-time variables. *Journal of Engineering Mathematics*, 47(3-4), pp.217-250.

Shi, Y., Lawford, P. and Hose, R., 2011. Review of zero-D and 1-D models of blood flow in the cardiovascular system. *Biomedical engineering online*, 10(1), p.33.

Shojima, M., Oshima, M., Takagi, K., Torii, R., Hayakawa, M., Katada, K., Morita, A. and Kirino, T., 2004. Magnitude and role of wall shear stress on cerebral aneurysm: computational fluid dynamic study of 20 middle cerebral artery aneurysms. *Stroke*, 35(11), pp.2500-2505.

Silva Neto, Â.R., Câmara, R.L.B. and Valença, M.M., 2012. Carotid siphon geometry and variants of the circle of Willis in the origin of carotid aneurysms. *Arquivos de neuro-psiquiatria*, 70(12), pp.917-921.

Songsaeng, D., Geibprasert, S., Willinsky, R., Tymianski, M., TerBrugge, K.G. and Krings, T., 2010. Impact of anatomical variations of the circle of Willis on the incidence of aneurysms and their recurrence rate following endovascular treatment. *Clinical radiology*, 65(11), pp.895-901.

Soudah, E., Rossi, R., Idelsohn, S. and Oñate, E., 2014. A reduced-order model based on the coupled 1D-3D finite element simulations for an efficient analysis of hemodynamics problems. *Computational Mechanics*, 54(4), pp.1013-1022.

Soudah, E., Rossi, R., Idelsohn, S. and Oñate, E., 2014. A reduced-order model based on the coupled 1D-3D finite element simulations for an efficient analysis of hemodynamics problems. *Computational Mechanics*, 54(4), pp.1013-1022.

Steele, B.N., Wan, J., Ku, J.P., Hughes, T.J. and Taylor, C.A., 2003. In vivo validation of a one-dimensional finite-element method for predicting blood flow in cardiovascular bypass grafts. *IEEE Transactions on Biomedical Engineering*, 50(6), pp.649-656.

Stergiopoulos, N., Young, D.F. and Rogge, T.R., 1992. Computer simulation of arterial flow with applications to arterial and aortic stenoses. *Journal of biomechanics*, 25(12), pp.1477-1488.

Stoquart-ElSankari, S., Lehmann, P., Villette, A., Czosnyka, M., Meyer, M.E., Deramond, H. and Balédent, O., 2009. A phase-contrast MRI study of physiologic cerebral venous flow. *Journal of Cerebral Blood Flow & Metabolism*, 29(6), pp.1208-1215.

Taber, Clarence Wilbur; Venes, Donald 2009. *Taber's cyclopedic medical dictionary*. F a Davis Co. pp. 1018-1023.

Taelman, L., Degroote, J., Verdonck, P., Vierendeels, J. and Segers, P., 2013. Modeling hemodynamics in vascular networks using a geometrical multiscale approach: numerical aspects. *Annals of biomedical engineering*, 41(7), pp.1445-1458.

Tanaka, H., Fujita, N., Enoki, T., Matsumoto, K., Watanabe, Y., Murase, K. and Nakamura, H., 2006. Relationship between variations in the circle of Willis and flow rates in internal carotid and basilar arteries determined by means of magnetic resonance imaging with

semiautomated lumen segmentation: reference data from 125 healthy volunteers. *American journal of neuroradiology*, 27(8), pp.1770-1775.

Taylor, C.L., Yuan, Z., Selman, W.R., Ratcheson, R.A. and Rimm, A.A., 1995. Cerebral arterial aneurysm formation and rupture in 20,767 elderly patients: hypertension and other risk factors. *Journal of neurosurgery*, 83(5), pp.812-819.

Thom, T., Haase, N., Rosamond, W., Howard, V.J., Rumsfeld, J., Manolio, T., Zheng, Z.J., Flegal, K., O'donnell, C., Kittner, S. and Lloyd-Jones, D., 2006. Heart disease and stroke statistics—2006 update: a report from the American Heart Association Statistics Committee and Stroke Statistics Subcommittee. *Circulation*, 113(6), pp.e85-e151.

Torii, R., Oshima, M., Kobayashi, T., Takagi, K. and Tezduyar, T.E., 2010. Influence of wall thickness on fluid - structure interaction computations of cerebral aneurysms. *International Journal for Numerical Methods in Biomedical Engineering*, 26(3 - 4), pp.336-347.

Toro, E.F. and Siviglia, A., 2013. Flow in collapsible tubes with discontinuous mechanical properties: mathematical model and exact solutions. *Communications in Computational Physics*, 13(2), pp.361-385.

Ujiie, H., Liepsch, D.W., Goetz, M., Yamaguchi, R., Yonetani, H. and Takakura, K., 1996. Hemodynamic study of the anterior communicating artery. *Stroke*, 27(11), pp.2086-2094.

Uston, C., 2005. NEUROwords Dr. Thomas Willis' famous eponym: the circle of Willis. *Journal of the History of the Neurosciences*, 14(1), pp.16-21.

Van de Vosse, F.N. and Stergiopulos, N., 2011. Pulse wave propagation in the arterial tree. *Annual Review of Fluid Mechanics*, 43, pp.467-499.

Vega, C., Kwon, J.V. and Lavine, S.D., 2002. Intracranial aneurysms: current evidence and clinical practice. *American family physician*, 66(4), pp.601-610.

Vignon-Clementel, I.E., Figueroa, C.A., Jansen, K.E. and Taylor, C.A., 2006. Outflow boundary conditions for three-dimensional finite element modeling of blood flow and pressure in arteries. *Computer methods in applied mechanics and engineering*, 195(29-32), pp.3776-3796.

Wang, J.J. and Parker, K.H., 2004. Wave propagation in a model of the arterial circulation. *Journal of biomechanics*, 37(4), pp.457-470.

Wiebers, D.O. and International Study of Unruptured Intracranial Aneurysms Investigators, 2003. Unruptured intracranial aneurysms: natural history, clinical outcome, and risks of surgical and endovascular treatment. *The Lancet*, 362(9378), pp.103-110.

Wilcox, D.C., 2000. *Basic fluid mechanics*. DCW industries.

Xiang, J., Natarajan, S.K., Tremmel, M., Ma, D., Mocco, J., Hopkins, L.N., Siddiqui, A.H., Levy, E.I. and Meng, H., 2011. Hemodynamic–morphologic discriminants for intracranial aneurysm rupture. *Stroke*, 42(1), pp.144-152.

Xiang, J., Siddiqui, A.H. and Meng, H., 2014. The effect of inlet waveforms on computational hemodynamics of patient-specific intracranial aneurysms. *Journal of biomechanics*, 47(16), pp.3882-3890.

Xiang, J., Tremmel, M., Kolega, J., Levy, E.I., Natarajan, S.K. and Meng, H., 2011. Newtonian viscosity model could overestimate wall shear stress in intracranial aneurysm domes and underestimate rupture risk. *Journal of neurointerventional surgery*, pp.neurintsurg-2011.

Xiang, J., Tutino, V.M., Snyder, K.V. and Meng, H., 2014. CFD: computational fluid dynamics or confounding factor dissemination? The role of hemodynamics in intracranial



aneurysm rupture risk assessment. American Journal of Neuroradiology, 35(10), pp.1849-1857.

Xiao, N., Alastruey, J. and Alberto Figueroa, C., 2014. A systematic comparison between 1 - D and 3 - D hemodynamics in compliant arterial models. International journal for numerical methods in biomedical engineering, 30(2), pp.204-231.

Xiao, N., Humphrey, J.D. and Figueroa, C.A., 2013. Multi-scale computational model of three-dimensional hemodynamics within a deformable full-body arterial network. Journal of computational physics, 244, pp.22-40.

Yang, Z., Yu, H., Huang, G. P., & Ludwig, B. (2017). Divergence Compensatory Optical Flow Method for Blood Velocimetry. Journal of Biomechanical Engineering, 139(6), 061005.

Yang, Z., Yu, H., Huang, G.P., Schwieterman, R. and Ludwig, B., 2015. Computational fluid dynamics simulation of intracranial aneurysms—comparing size and shape. Journal of Coastal Life Medicine, 3(3), pp.245-252.

Yee HC. Upwind and symmetric shock-capturing schemes. NASA-TM 89464, 1987.

Yu, H., Huang, G.P., Yang, Z., Liang, F. and Ludwig, B., 2016. The influence of normal and early vascular aging on hemodynamic characteristics in cardio-and cerebrovascular systems. Journal of biomechanical engineering, 138(6), p.061002.

Zacharia, B.E., Hickman, Z.L., Grobelny, B.T., DeRosa, P., Kotchetkov, I., Ducruet, A.F. and Connolly, E.S., 2010. Epidemiology of aneurysmal subarachnoid hemorrhage. Neurosurgery Clinics, 21(2), pp.221-233.

COPYRIGHT BY

HONGTAO YU

2018